XENON-INDUCED POWER OSCILLATIONS IN A GENERIC SMALL MODULAR REACTOR

A Dissertation

by

EVANS DAMENORTEY KITCHER

Submitted to the Office of Graduate and Professional Studies of
Texas A&M University
in partial fulfillment of the requirements for the degree of

DOCTOR OF PHILOSOPHY

Chair of Committee,	Sunil S. Chirayath
Committee Members,	William S. Charlton
	John W. Poston, Sr.
	Wolfgang Bangerth
Head of Department,	Yassin A. Hassan

August 2016

Major Subject: Nuclear Engineering

ABSTRACT

As world demand for energy continues to grow at unprecedented rates, the world energy portfolio of the future will inevitably include a nuclear energy contribution. It has been suggested that the Small Modular Reactor (SMR) could play a significant role in the spread of civilian nuclear technology to nations previously without nuclear energy. As part of the design process, the SMR design must be assessed for the threat to operations posed by xenon-induced power oscillations.

In this research, a generic SMR design was analyzed with respect to just such a threat. In order to do so, a multi-physics coupling routine was developed with MCNP/MCNPX as the neutronics solver. Thermal hydraulic assessments were performed using a single channel analysis tool developed in Python. Fuel and coolant temperature profiles were implemented in the form of temperature dependent fuel cross sections generated using the SIGACE code and reactor core coolant densities.

The Power Axial Offset (PAO) and Xenon Axial Offset (XAO) parameters were chosen to quantify any oscillatory behavior observed. The methodology was benchmarked against results from literature of startup tests performed at a four-loop PWR in Korea. The developed benchmark model replicated the pertinent features of the reactor within ten percent of the literature values. The results of the benchmark demonstrated that the developed methodology captured the desired phenomena accurately.

Subsequently, a high fidelity SMR core model was developed and assessed. Results of the analysis revealed an inherently stable SMR design at beginning of core life and end of core life under full-power and half-power conditions.

The effect of axial discretization, stochastic noise and convergence of the Monte Carlo tallies in the calculations of the PAO and XAO parameters was investigated. All were found to be quite small and the inherently stable nature of the core design with respect to xenon-induced power oscillations was confirmed.

Finally, a preliminary investigation into excess reactivity control options for the SMR design was conducted confirming the generally held notion that existing PWR control mechanisms can be used in iPWR SMRs with similar effectiveness. With the desire to operate the SMR under the boron free coolant condition, erbium oxide fuel integral burnable absorber rods were identified as a possible means to retain the dispersed absorber effect of soluble boron in the reactor coolant in replacement.

DEDICATION

To my loving parents, Paul and Caroline, I would not be where I am today without you.

ACKNOWLEDGEMENTS

I would like to express my deepest gratitude to my advisor and committee chair, Dr. Sunil S. Chirayath first and foremost for his wisdom and guidance which has stood me in good stead throughout the course of this research. He has provided a wonderful learning environment where I have found endless support allowing me to grow and mature both as an academic, young professional and more importantly as a person. You are a true gentleman and I am proud to call you my friend.

I would like to thank my committee members individually; Dr. Charlton, for his insightful observations and comments which always resulted in improvement of the dissertation research; Dr. Bangerth for ensuring mathematical and simulation rigor in the developed methodology and Dr. Poston for his meticulous revision of the dissertation always seeking to improve the final product and my skill in presentation and communication of technical material. Gentlemen it has been a pleasure and an honor.

I would also like to thank the staff and faculty of the Department of Nuclear Engineering and my friends and colleagues at Texas A&M University for making my time here a greatly rewarding one.

To my family, thank you for being my refuge and source of strength. Lastly to my wife, a man who finds a good wife is blessed indeed! Thank you for never ending belief in me and loving me through the completion of this research.

NOMENCLATURE

ACE	A Compact ENDF
ASI	Axial Separation Index
BAR	Burnable Absorber Rod
BOL	Beginning of core life
CHF	Critical Heat Flux
DNBR	Departure from Nucleate Boiling
DOE	United States Department of Energy
ENDF	Evaluated Nuclear Data File
EOL	End of core life
H/D	Height-to-diameter ratio
IAEA	International Atomic Energy Agency
iPWR	Integral Pressurized Water Reactor
LWR	Light Water Reactor
LOCA	Loss of Coolant Accident
MCNP	Monte Carlo N-Particle transport code
PAO	Power Axial Offset
PWR	Pressurized Water Reactor
SCA	Single Channel Analysis
SMR	Small Modular Reactor
USNRC	United States Nuclear Regulatory Commission
XAO	Xenon Axial Offset

TABLE OF CONTENTS

Page

LIST OF FIGURES

Page

LIST OF TABLES

Page

1 INTRODUCTION

1.1 Introduction

As the world demand for electrical energy continues to grow at unprecedented rates, the world energy portfolio of the future will inevitably include a nuclear energy contribution. It has been suggested that the Small Modular Reactor (SMR) could play a significant role in the spread of civilian nuclear technology to nations previously without nuclear energy. As part of the progression of advanced and next generation reactor designs, a wide spectrum of SMR concepts are being developed all over the globe.

In order to capture the complex core geometries and material heterogeneity featured in these and other advanced reactor designs, the use of the Monte Carlo method in core modeling and reactor physics simulations has become increasingly popular. This trend has been aided and even accelerated by ever increasing computational power through increased computer memory capacity and processor speeds.[1] In addition to full blown three-dimensional models of the core geometry, multi-physics simulation tools are being developed whereby existing state-of-the-art independent physics codes are coupled via an external coupling script. These high fidelity codes can independently simulate the neutronic, thermal hydraulic, chemical and mechanical phenomena occurring within the reactor core. In reality, it is often the interplay of these phenomena which constitute vital cogs in the workings of any system. Often, an adequate understanding of several modes of operation of the reactor core cannot be attained without taking into account the various forms of feedback that exist between the various physical phenomena involved.

As such, in this research, a generic SMR design was developed and analyzed. A multi-physics coupling routine was developed and utilized to introduce thermal hydraulic

assessment and feedback in the form of temperature dependent fuel cross sections and reactor core coolant density. The research assessed the threat to safety and operation of the generic SMR model including that posed by xenon-induced power oscillations. The goal was to develop a methodology whereby a dynamic phenomenon such as xenon-induced power oscillations could be analyzed using the Monte Carlo method whilst informing design and development of SMR technology.

1.2 Background

Traditionally, the commercial nuclear market has been focused on reactor designs with large power outputs (1000–1700 MWe).[2] These single large output units are unsuited for the limited electric grid capacity in many developing countries.[3] In addition the electrical grid infrastructure in some of these countries is highly decentralized and located in a few isolated population centers with minimal interconnections. This situation favors the use of smaller power plants sited at geographically separated locations.

The International Atomic Energy Agency has defined the Small Modular Reactor (SMR) as 'reactors that produce electric power up to 300 MWe, designed to be built in factories and shipped to utilities for installation as demand arises'. By this definition, there are over thirty SMR designs under development around the world spanning the entire range of nuclear technologies currently available. The SMR represents an exciting and viable pathway to the deployment of new nuclear technology as part of a renaissance in nuclear energy[4] primarily by offering several advantages over existing large commercial reactors. These benefits include inherent safety features, increased security and proliferation resistance with design integrated safeguards measures, and underground construction to address the

threats of sabotage, airplane impact and some natural hazard scenarios.[5] In addition, SMRs are anticipated to offer significant economic advantages when compared to larger nuclear technology options in the form of lower initial capital investment, shorter construction times and a greater ability to match plant capacity with demand for electricity. Both the end user of the electricity and the developer of the power plant stand to profit from scale gains which are not present in a conventional large Pressurized Water Reactor (PWR). These gains are found in greater site selection flexibility for SMRs which are suited to areas with smaller electrical grids, limited supplies of water and/or land allowing greater proximity to the end user and to industry for process heat applications. The combination of these and other factors make SMRs a very attractive form of nuclear technology as they offer electric grid and economic appropriateness in existing world economic conditions.[4 6 7 8 9 10]

1.3 Motivation

The continued and growing interest in making SMR technology a reality in the near future requires a substantial research effort to verify SMR design and safety with high fidelity models for various configurations. Although coupled neutron kinetics and thermal hydraulics methodologies exist and have been extensively used with respect to the PWR and other light water applications, there is limited experience for integral Pressurized Water Reactor (iPWR) type SMRs using such simulation approaches. SMRs feature inherent safety characteristics that make their accident progressions significantly different warranting a revision of the transient analyses performed. Thus, establishing high fidelity coupled methodologies are important for transient situations featuring significant variations in the shape of the neutron flux.

1.4 Objective

The objective of this research was to assess the threat posed by xenon-induced power oscillations to the normal operations of a generic SMR of the iPWR type. In order to do so, xenon-induced power oscillations in a generic iPWR-type SMR reactor core must be modeled using a computational multi-physics coupling routine with the Monte Carlo N-Particle (MCNP) radiation transport code containing fuel burn-up code (CINDER90) as the chosen neutronics solver. A thermal hydraulic component is necessary due to the fundamental physics underlying the production and destruction of xenon within reactor cores and the resulting effects on core power.

Significant implications of the proposed research would be to: first, provide insight and help instruct decisions made regarding the design approach applied to iPWR-type SMR control; second, aid in the formulation of a control methodology for iPWR-type SMRs (both in normal operation and accident scenarios); third, provide a starting point and publicly available reference data for the continued research and discussion regarding control and shutdown diversity in a boron-free environment; and lastly, help educate preliminary control rod/mechanism design for the iPWR-type SMR.

1.5 Dissertation Overview

Section 2 introduces the iPWR concept and provides a brief overview of the more promising existing iPWR SMR designs. A detailed discussion of the dynamics involved with xenon-induced power oscillations and the parameters affecting the xenon stability of a core design are presented and followed by an overview of the requirements of the simulation approach chosen to perform the research.

Section 3 is focused on the research methodology employed, presenting descriptions of the computational codes utilized and explaining how these tools are coupled using an external routine to perform the multi-physics simulations of the phenomena required to analyze xenon-induced power oscillations. In Section 4, a case study of xenon induced power oscillations is performed on a simplified model, the results of which are compared to the literature for validating the coupling methodology.

Section 5 provides a detailed description of the development of the SMR core model. The SMR core physics simulations and analyses for the presence of xenon-induced power oscillations are described in Section 6. Sensitivity studies investigate the effects of axial spatial discretization and stochastic noise in a single result inherent to the Monte Carlo process.

In closing, a summary of the results, their practical implications and the major conclusions from the research are presented in Section 7 with possible avenues for future research identified and briefly explored.

2 LITERATURE REVIEW

In this section, the iPWR SMR design concept is introduced in Section 2.1 leading into a brief discussion of existing SMR designs of the iPWR type in Section 2.2. Literature on the characteristics and dynamics of xenon within the core is presented in Section 2.3 followed by a discussion on the simulation approach selected in closing in Section 2.4.

2.1 The Integral Pressurized Water Reactor Concept

The Integral Pressurized Water Reactor (iPWR) design concept is a simple yet radical solution to one of the worst accident scenarios for existing PWRs: the large break loss of coolant accident or large break LOCA. In a large break LOCA scenario, the initiating event for the accident is a large double ended break of one of the large coolant pipes connecting the reactor core to the steam generators, typically the leg with the pressurizer attached. This event leads to rapid loss of coolant through the break and depressurization resulting in the core being left uncovered. A common end state for the scenario is fuel failure due to melting and a significant radioactive fission product and actinide source term release. The mitigation approach in the past has been to add a plethora of auxiliary safety systems to PWR designs to ensure that, in the case of the large-break LOCA, the core remains covered with coolant and the heat removal systems remain capable of removing the remaining decay heat.

In contrast, the iPWR design approach to this accident scenario is to reduce it by eliminating the large coolant pipes where these accidents occur. This is achieved by placing the pressurizer, steam generator and coolant pumps in a single pressure vessel with the reactor core. Smaller reactors allow a pressure vessel large enough to accommodate the required components to be forged. Figure 1 is a schematic of the layout of an iPWR SMR.

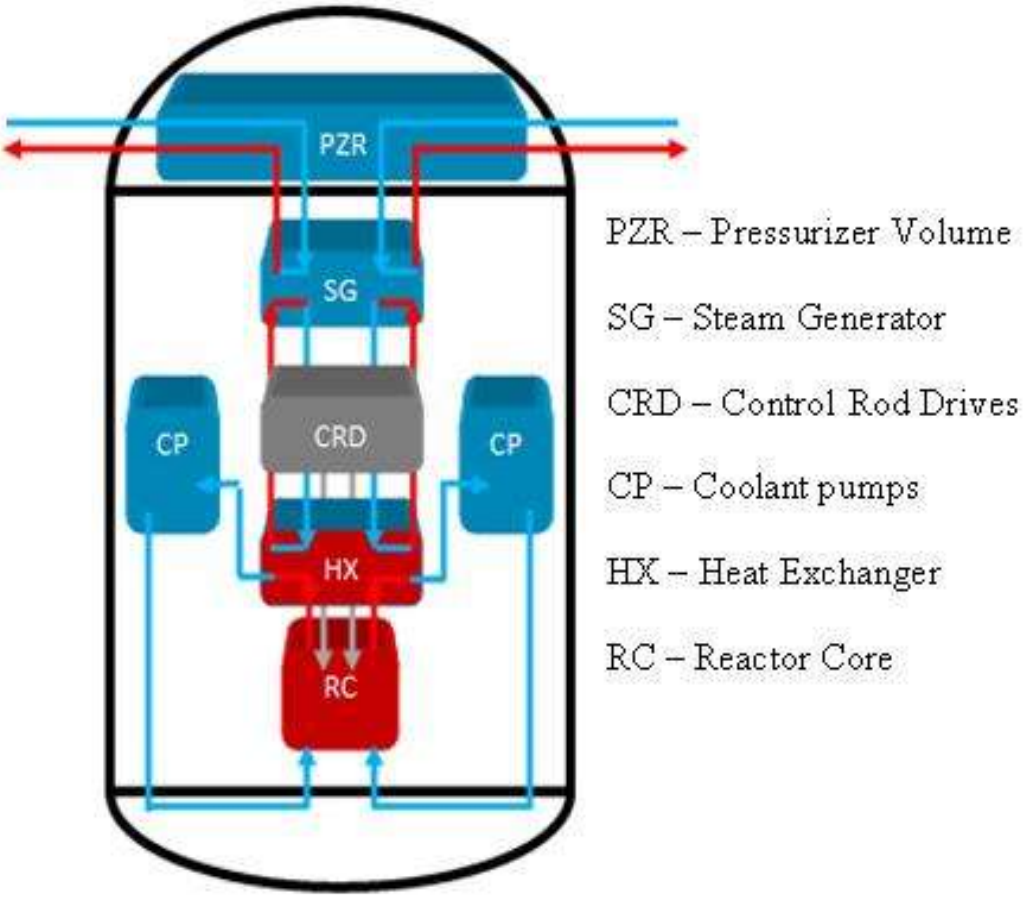

Figure 1: Component Schematic of an Integral PWR

As mentioned, the SMRs that are in the near deployment stage are all of this iPWR type. Not only does this design concept eliminate an entire category of accident scenarios but also increases the coolant inventory in the core allowing heat removal by natural circulation to be applicable over a wider range of operation. It is this kind of innovation with respect to safety by design and decreased capital and operation costs by eliminating auxiliary safety systems that is characteristic of SMRs and differentiates them from previous small reactor designs.

In addition, all components of these SMRs are designed to be manufactured in a factory setting and transportable by barge, truck or rail to the plant site, where the reactor will be assembled. Benefits of the modular design philosophy include reduced construction times as components are pre-fabricated and increased quality of components as quality assurance would be done in the highly controlled environment of the factory.

2.2 Existing iPWR SMR Designs

SMR designs under development around the world include thermal, epithermal and fast neutron spectrum reactors, light water, heavy water, gas and liquid metal coolants and electrical power output at both ends of the 5 MWe to the 300 MWe range. Within this global development effort, the United States Nuclear Regulatory Commission (USNRC) is currently involved in commercial licensing related procedures for four SMR designs. The designs under review are the NuScale SMR, the B&W mPower SMR, the Westinghouse SMR and the Holtec SMR-160.[11] The following is a brief description of each of these designs; all variations of the iPWR design concept

2.2.1 NuScale SMR

The NuScale SMR is an iPWR design offering from NuScale Power LLC scheduled to begin design certification application procedures with the USNRC in the second half of 2016.[12] The design is based on the Multi-Application Small Light Water Reactor (MASLWR) project developed at Oregon State University in collaboration with Idaho National Laboratory under funding from the United States Department of Energy (U.S.D.O.E) in the early 2000's. The design is intended for natural circulation cooling in all

operation modes including full-power operation at its rated 50 MWe. The pressure vessel (containing the core, pressurizer and steam generator) is to be submerged in the reactor building safety related pool increasing design safety. The reactor building itself will be below grade and is designed to house up to twelve NuScale SMRs for a total plant power of 600 MWe.[10 13 14 15] The fuel will be in the form of reduced height standard PWR 17 x 17 fuel assemblies with a maximum fuel enrichment of 5.0 wt. % ^{235}U on a nominal two-year refueling cycle.[16]

2.2.2 Holtec SMR-160

The Holtec SMR-160 is an iPWR design offering from SMR LLC, a subsidiary company of Holtec International (Holtec). Like the NuScale SMR, the SMR-160 is intended for a passive cooling regime but unlike the other designs on the US market, the SMR-160 design features an integrated containment design rather than an integrated vessel design. Each module is designed to produce 160 MWe and features a containment that houses the reactor vessel, steam generator, pressurizer, and spent fuel pool. The containment is designed to be below grade.[17]

2.2.3 Westinghouse SMR

The Westinghouse SMR is an iPWR design offering from Westinghouse Electric Company that improves on Westinghouse's proven AP1000 technology with regards to simplicity and passive safety.[18] The Westinghouse SMR is intended for forced circulation cooling, the pressure vessel is designed to house the core, eight coolant pumps, the pressurizer and steam generator. Each module is designed to produce 225 MWe with the

pressure vessel submerged in water in the reactor building as a standalone unit. The reactor building is designed to be below grade. The fuel will be in the form of reduced height standard PWR 17 x 17 fuel assemblies with a maximum fuel enrichment of 5.0 wt. % ^{235}U on a nominal two-year refueling cycle.[10]

2.2.4 B&W mPower SMR

The B&W mPower SMR is an iPWR design offering from Generation mPower LLC, a subsidiary company of Babcock & Wilcox (B&W). The mPower SMR began pre-application activities with the NRC in 2009.[19] The design is derived from B&W's 50+ years of experience in the design, and manufacturing of reactor technology and represents the culmination of existing B&W generation III+ technology. Intended for forced circulation cooling, the pressure vessel is designed to house the core, eight coolant pumps, the pressurizer and steam generator. The reactor building is designed to be below grade. The nameplate power of each module is 180 MWe and the standard plant design is a 'twin pack' orientation for a total plant power of 360 MWe. If desired, a plant configuration featuring 10 modules at a single site would result in a total plant power of 1800 MWe; comparable to existing large PWRs. The fuel will be in the form of reduced height standard PWR 17 x 17 fuel assemblies with a maximum fuel enrichment of 5.0 wt. % ^{235}U on a nominal four-year refueling cycle.[10 20]

2.3 Xenon Dynamics and Stability

2.3.1 Xenon Characteristics

The isotope of xenon (Xe-135 or ^{135}Xe) is a fission product and has been known as a

neutron "poison" since 1944.[21 22] The fundamental physics governing the behavior of xenon in nuclear reactor cores have long been understood.[23 24 25 26] Xenon-135 plays a key role in the neutronics of the reactor core due to a combination of many factors. Firstly, it has a very large thermal neutron absorption cross section of 2.6 million barns.[27] Secondly, it has a relatively large cumulative fission yield of approximately six percent. The direct fission yield of Xenon-135 is only 0.2 percent with the remainder of production coming from the decay of its precursors; antimony-135 (Sb-135 or ^{135}Sb), Tellurium-135 (Te-135 or ^{135}Te) and iodine-135 (I-135 or ^{135}I). The half-lives of the decay of antimony-135 and tellurium-135 to iodine-135 are very short (1.68 s and 19 s, respectively). However, iodine-135 decays to xenon-135 with a half-life of 6.58 hours. As a result xenon-135 is produced (from decay) with a delay while its removal is based on its large neutron absorption cross section and its own decay. A simplified production scheme for xenon-135 is shown in Figure 2.

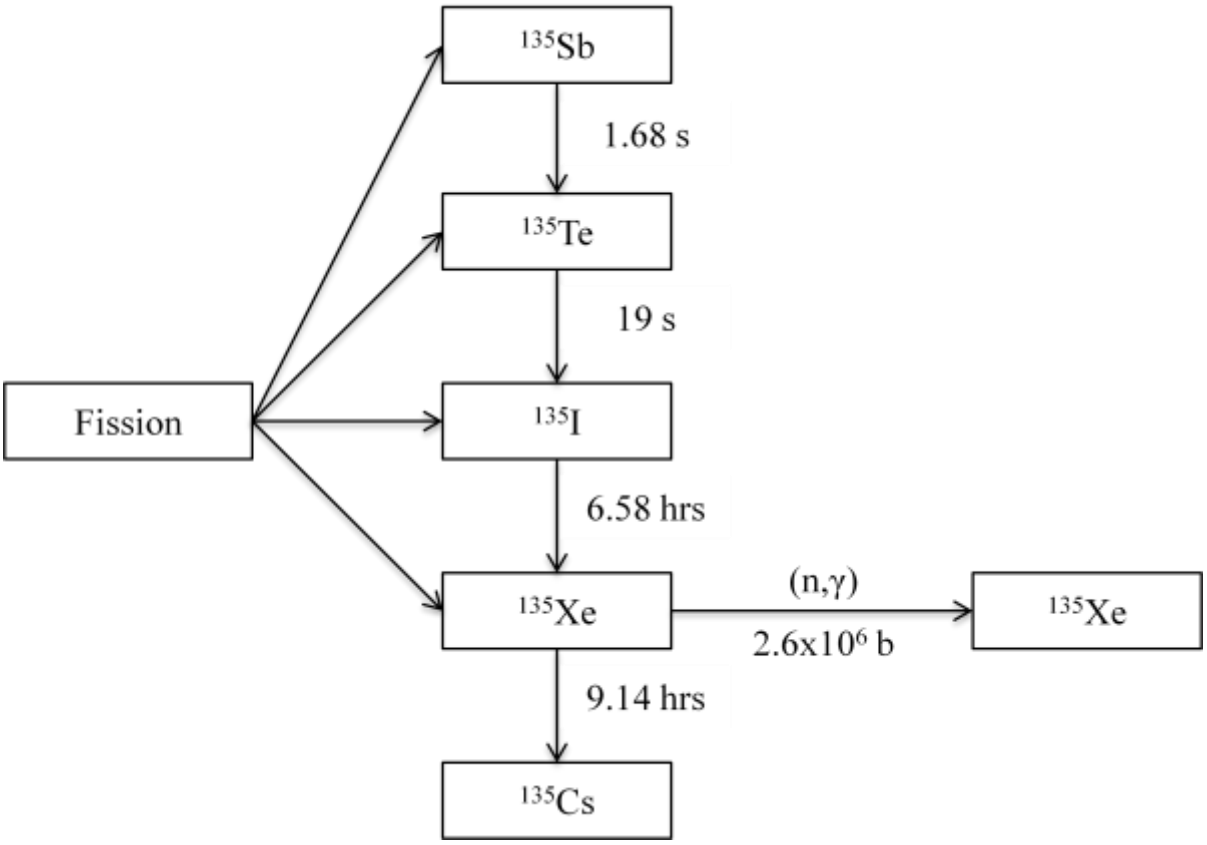

Figure 2: Simplified Decay Chain for Xenon-135

2.3.2 Equilibrium Xenon

Assume iodine-135 is produced from fission and destroyed by decay directly to xenon-135. Then assume xenon-135 is produced from fission and the decay of iodine-135 and is destroyed by decay and neutron capture, the conservation equations for iodine and xenon can be written as

$$\frac{\partial \mathrm{I}}{\partial \mathrm{t}} = \gamma_{\mathrm{I}} \sum_{\mathrm{f}} \phi(\mathrm{r},\mathrm{t}) - \lambda_{\mathrm{I}} \mathrm{I}(\mathrm{r},\mathrm{t})$$

$$\frac{\partial \mathrm{Xe}}{\partial \mathrm{t}} = \gamma_{\mathrm{Xe}} \sum_{\mathrm{f}} \phi(\mathrm{r},\mathrm{t}) + \lambda_{\mathrm{I}} \mathrm{I}(\mathrm{r},\mathrm{t}) - \lambda_{\mathrm{Xe}} \mathrm{Xe}(\mathrm{r},\mathrm{t}) - \sigma_{\mathrm{a,Xe}} \phi(\mathrm{r},\mathrm{t}) \mathrm{Xe}(\mathrm{r},\mathrm{t}).$$

At equilibrium, $\frac{\partial I}{\partial t} = \frac{\partial Xe}{\partial t} = 0$ and the equilibrium concentrations can be found:

$$I(r) = \frac{\gamma_I \sum_f \phi(r)}{\lambda_I}$$

$$Xe(r) = \frac{(\gamma_I + \gamma_{Xe}) \sum_f \phi(r)}{\lambda_{Xe} + \sigma_{a,Xe}\phi(r)}$$

where $I(r,t)$ and $Xe(r,t)$ are the iodine and xenon concentrations in space r and time t; $\frac{\partial I}{\partial t}$ and $\frac{\partial Xe}{\partial t}$ are the time rate of change of the iodine and xenon concentrations; γ_I and γ_{Xe} are the fission yields iodine and xenon; λ_I and λ_{Xe} are the decay constants of iodine and xenon; $\sum_f$ is the macroscopic fission cross section; $\phi(r,t)$ is the scalar neutron flux; and $\sigma_{a,Xe}$ is the microscopic absorption cross section of xenon. Note that the equilibrium level of iodine and xenon in any region in the core is dependent on the flux in that region.

2.3.3 Dynamics of Xenon-Induced Power Oscillations

To understand the dynamics underlying xenon-induced power oscillations, let us consider a reactor with two loosely coupled regions, initially in steady state with the neutron flux and xenon concentrations equal in both regions. An initiating event such as control rod movement, change in power or temperature causes a local perturbation in the thermal neutron flux (let us say an increase) in region one.

Region 1 experiences an immediate increase in xenon-135 removal from increased neutron capture. The production of iodine-135 similarly is increased from increased fission. The production of xenon-135 (from iodine-135 decay) however remains at previous equilibrium levels due to the 6.58-hour half-life of iodine-135. As a result, net xenon-135 concentration decreases causing the neutron flux in region 1 to increase further. This will continue until the xenon-135 concentration increases to match the new increased thermal

neutron flux. At this point thermal neutron flux in region 1 will begin to decrease due to increased removal from xenon-135 capture.

In order to maintain constant total power of the reactor, the flux in the region 2 decreases correspondingly. Hence, the removal of xenon-135 through neutron capture will decrease while the production of xenon-135 (from iodine-135 decay) remains at the previous equilibrium level. The net result is an increase in xenon-135 concentration (from iodine-135 decay) further decreasing the flux in region 2. Again, this will continue until xenon-135 production (from iodine-135 decay) decreases to match the decreased thermal flux after which thermal flux levels will increase due to decreased removal from xenon-135 capture.

Thus, region 1 increases to a maximum thermal neutron flux and the minimum xenon-135 concentration then decreases again while region 2 decreases to a minimum neutron flux and maximum xenon-135 concentration before increasing. Depending on the design of the reactor core, these oscillations may be self-stabilizing and eventually dampen out, or they may continue to grow and threaten reactor operation.

2.3.4 Xenon Stability

The bounding time scale for xenon dynamics is determined by the half-lives of iodine-135 and xenon-135 at 6.58 hours and 9.14 hours, respectively. Thus, typical oscillation periods are on the order of one day giving ample opportunity for xenon-induced power oscillations in commercial reactors to be controlled. One notable implication of the oscillation period is that both short-term effects (delayed neutrons, etc.) can be safely ignored and temperature variations assumed to be quasi-steady state.

In order for xenon oscillations to occur, two conditions must be met. First, the reactor must be physically large to the extent where the physical dimensions of the core are several times larger than the neutron diffusion length for the core. The average diffusion length of a neutron in a thermal reactor is in the order of a few centimeters. The larger the core, the greater the chance of achieving a state whereby certain regions of the core are spatially decoupled resulting in a delay with respect to propagation of the effects of a change in the neutron flux; allowing oscillations to occur. Tightly-coupled cores are less likely to exhibit oscillatory behavior due to the effect of a change in flux levels in one region being immediately propagated to all other regions. The second condition is that the thermal neutron flux must be large enough such that the rate of destruction of xenon-135 is significantly larger than destruction by decay. This large neutron flux allows for the instantaneous destruction of xenon-135 due to an increased flux level potentially resulting in xenon-induced power oscillations.

In general, the xenon stability of a reactor design decreases with increasing core size, increasing thermal neutron flux levels, increasing core height-to-diameter ratio, decreasing neutron diffusion length, decreasing magnitude of the negative power coefficient, increasing uniformity of the thermal flux distribution and decreasing fuel enrichment.[28] Thus, an SMR core with large height to diameter (H/D) ratio for the core, a small negative power coefficient of reactivity with low enriched uranium (LEU) fuel is a potential candidate to experience xenon-induced power oscillations. Additionally the probability of the oscillations occurring increases with the fuel burn-up and flattening of power and neutron flux profiles.[23]

2.4 Simulation Approach

In order to perform the desired analysis and determine the threat posed to the iPWR SMR from xenon-induced power oscillations, the chosen simulation approach should sufficiently account for the fundamental phenomena underpinning the rate of change of xenon-135 within the reactor core and spatial xenon-135 concentration information obtained. To do so at a satisfactory level, one must essentially solve coupled multi-physics equations for neutron transport, fuel depletion and transmutation equations, thermal heat conduction within the fuel with fission and radiative capture source terms, convective heat transfer and fluid flow within the coolant channels with the appropriate initial conditions, boundary conditions and equations of state for closure.

The high level of complexity required in a single computational code that can adequately handle the above mentioned physics intrinsically and the existence of state of the art "single" physics codes has resulted in a common simulation approach whereby an external routine is used to couple existing codes that handle one or two of the required physics. This is achieved using the MCNP/MCNPX codes with coupled thermal hydraulics. The MCNP/MCNPX codes in particular have been employed as the neutronics and fuel transmutation solver in many such routines.[29 30 31 32 33 34 35 36 37 38 39 40]

3 METHODOLOGY

In this section a description of the computational tools used to perform the coupled multi-physics analysis of the SMR design is presented in conjunction with the developed computational methodology

3.1 Computational Methodology

The multi-physics coupling computational methodology developed as part of this research involves simulating the generic SMR core model using the MCNP/MCNPX[41 42] codes coupled to a semi-analytic thermal hydraulics assessment tool. Brief descriptions of each component of the coupling routine are provided below.

The first step of the routine is to determine initial power and temperature distributions of the reactor at "cold zero power" conditions. This is done by executing a single, separate eight-hour fuel (burn-up) depletion simulation in MCNPX with initial fuel and coolant temperatures at 300 °K and a coolant density of 0.99 g/cm^3 in all assemblies. The output of this initialization simulation is used to determine fuel temperature distribution and coolant temperature and density distributions for the first step of the production depletion calculations. Next, the MCNPX output file is parsed and material compositions extracted and stored using Python. Power fractions are fed to the Single Channel Analysis (SCA) tool and xenon-135 concentrations are extracted.

The SCA is implemented in Python and uses the power fractions from the MCNPX output to calculate volumetric heat generation rates for each axial fuel segment. These in conjunction with inlet coolant temperature and pressure are used to calculate axial fuel and coolant temperature distributions using a semi-analytical approach.[43] Coolant properties such

as density, specific heat capacity, thermal conductivity and viscosity for each axial coolant segment are determined as a function of temperature and pressure using the International Association for the Properties of Water and Steam (IAPWS) correlations.[44] Once the fuel temperature is determined, temperature dependent neutron reaction cross sections are generated using the SIGACE[45] tool developed by the International Atomic Energy Agency (IAEA). These updated parameters are used in the updated MCNPX depletion simulation. A system level flowchart of the developed multi-physics coupling routine is shown in Figure 3.

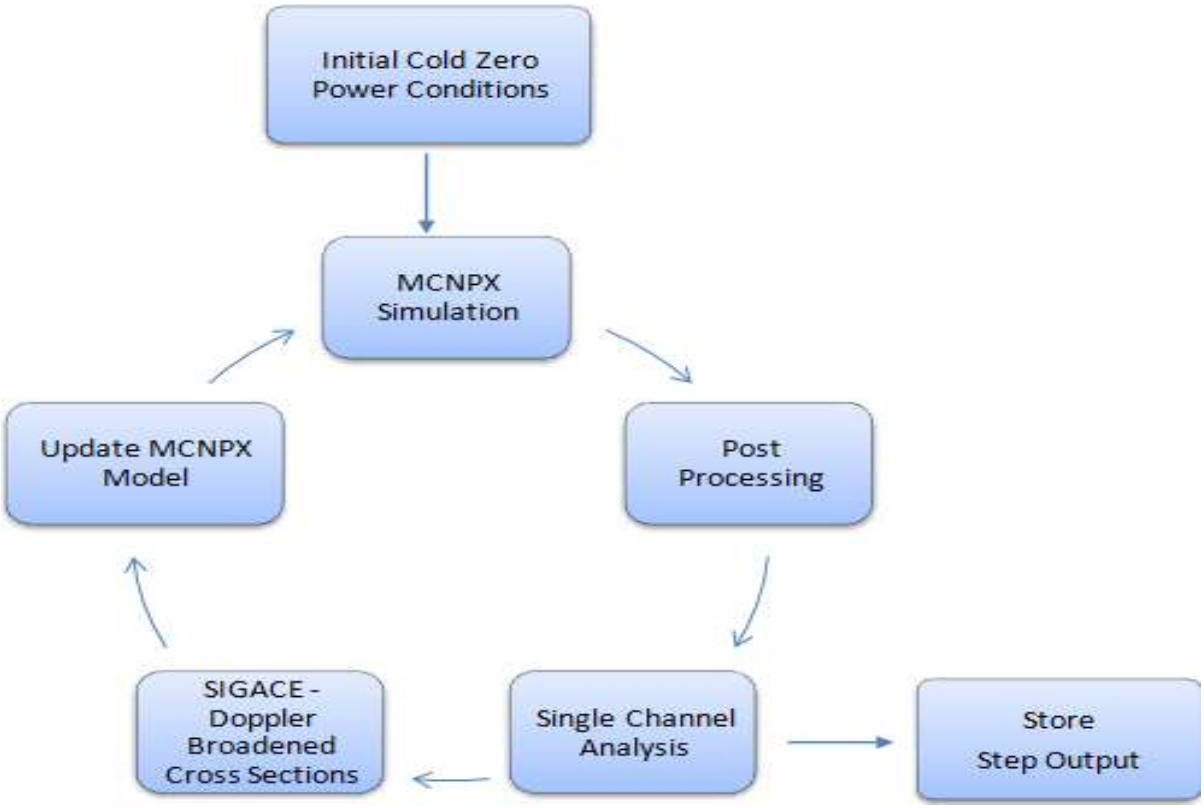

Figure 3: Flowchart for Multi-Physics Coupling Routine

3.2 Description of Tools

3.2.1 The Monte Carlo Method

The Monte Carlo method is a numerical technique that produces approximate solutions to problems that prove difficult to solve using other methods. The cornerstone of the method is the repeated random sampling of a probability distribution similar in nature to the throwing of dice at a gambling table in Monte Carlo and hence its name. By choosing appropriate probability distributions to sample, that are characteristic of the problem being solved, a numerical solution can be obtained. In the case of neutron transport, it is finding the solution of the Boltzmann Radiation Transport Equation. The Monte Carlo method simulates the transport of individual particles within the problem phase space, records specific details of each particle transport within the problem phase space and approximates the overall solution to the problem as the averaged particle behavior after simulating a large number of particles. The method works based on the fact that population statistics can be inferred from sample statistics given a sufficiently large sample according to the central limit theorem. Unlike deterministic methods for solving the Boltzmann Transport Equation which generally give a solution over the entire phase space for all predetermined quantities of interest (e.g. flux, current etc.), the Monte Carlo method typically solves only for user specified quantities in user defined portions of the problem phase space.

As mentioned, the Monte Carlo method is underpinned by random sampling of appropriate probability distributions. In order to do so, many Monte Carlo codes (including the MCNP and MCNPX codes) use Linear Congruential Generator algorithms to produce an essentially inexhaustible list of random numbers.

The events that comprise a particle history are determined by the rules (physics) and probabilities (nuclear transport data) governing the transport of the particle type through the materials specified in the problem phase space. As such, random numbers are used to determine the location and attributes with which a particle is born, the distance and direction the particle is to be transported until it interacts, the nuclide with which it interacts and associated type of interaction and the resulting changes to the nuclide and particle because of the interaction. This stochastic process is repeated a large number of times in order to achieve convergence to the solution of the problem being solved via the Monte Carlo simulation.

Monte Carlo methods lend themselves well to complex three-dimensional problem geometries where the nodal discretization of the problem phase-space prove to be a hindrance to the application of deterministic methods. Codes such as MCNP/MCNPX support the desire for high fidelity modeling of the reactor core needed for this dissertation research.

3.2.2 MCNP and MCNPX for Radiation Transport

The Monte Carlo N-Particle radiation transport code or MCNP is a general geometry three-dimensional Monte Carlo code developed at Los Alamos National Laboratory. The code can be used to perform individual or coupled neutron, photon and electron transport over a wide range of particle energies. The MCNP code offers many important features necessary for high fidelity neutronics modeling such as user defined geometries and material compositions. The lattice cell structure is particularly useful for modeling fuel assemblies and the reactor core. In addition thermal neutron scattering laws can be implemented which account for the influence on the scattering angle and energies of neutrons at thermal energies

acknowledging the fact that the target atom must be treated as being bound in a molecule (in most cases) and not as a free gas. Various particle tally types allow for neutron flux spectra and neutron spatial distributions to be determined.

MCNPX is an extension of the MCNP code that has extended energy ranges for neutron, photon and electron and many added capabilities including heavy charged particle transport, improved physics simulation models where experimental data does not exist and new variance reduction and data analysis techniques amongst others. Pertinent to this research, the MCNPX code can be used to perform transmutation, activation and burn-up analyses in reactor core physics simulations through the CINDER90 module.

The MCNP and MCNPX codes represent the state-of-the-art in Monte Carlo radiation transport methods and have been successfully applied to various reactor physics problems for various system configurations spanning the entire gamut of nuclear technologies including critical thermal, epithermal, fast and high-energy neutron spectrum systems, light water, gas and liquid metal-cooled systems and even accelerator-driven systems for both commercial and academic purposes. The MCNP and MCNPX codes have been extensively benchmarked and generally used as a benchmarking resource for other codes and applications in the field of nuclear engineering.[46 47 48 49]

3.2.3 CINDER90 for Fuel Depletion

The CINDER90 module in the MCNPX code uses Markov chains to solve the set of coupled differential equations that constitute the nuclide transmutation equations. CINDER90 is the current version of the CINDER code (also developed at Los Alamos National Laboratory) and features decay and interaction probability data for 3456 nuclides

including 30 fission yield sets, and yield data for 1325 fission-products.[50 51 52] The differential equations solved in CINDER90 are a simplified form of the Batemann equations:

$$\frac{\mathrm{dN_m}}{\mathrm{dt}} = -\mathrm{N_m(t)}\beta_\mathrm{m} + \sum_{\mathrm{k\neq m}} \mathrm{N_k(t)}\gamma_{\mathrm{k\rightarrow m}} + \overline{\mathrm{Y}}_\mathrm{m}$$

$$\beta_\mathrm{m} = \lambda_\mathrm{m} + \sum_\mathrm{r} \int \sigma_{\mathrm{m,r}}(\mathrm{E})\phi(\mathrm{r,E,t})\mathrm{dE}$$

$$\gamma_{\mathrm{k\rightarrow m}} = \sum_{\mathrm{m\neq k}} \mathrm{L_{km}}\,\lambda_\mathrm{k} + \sum_{\mathrm{m\neq k}} \sum_\mathrm{r} \int \mathrm{Y_{km,r}(E)}\sigma_{\mathrm{k,r}}(\mathrm{E})\phi(\mathrm{r,E,t})\mathrm{dE}$$

where $\frac{dN_m}{dt}$ is the rate of change of the nuclide density of m, $-N_m(t)\beta_m$ is the destruction rate of nuclide m, $\sum_{k\neq m} N_k(t)\gamma_{k\rightarrow m}$is the production rate of m summed over all other nuclides, $\bar{Y}_m$ is the production rate of m from an external source, λ_m is the destruction rate of m by radioactive decay, $\sum_r \int \sigma_{m,r}(E)\phi(r,E,t)dE$ is the destruction of m by transmutation into all other nuclides summed over all transmutation reactions, $\sum_{m\neq k} L_{km}\,\lambda_k$ is the production rate of m from the decay of all other nuclide and $\sum_{m\neq k}\sum_r \int Y_{km,r}(E)\sigma_{k,r}(E)\phi(r,E,t)dE$ is the summation of the production rate of m by transmutation of all other nuclides summed over all transmutation reactions.

The CINDER90 code uses its extensive set of nuclear data to dynamically determine which production/destruction chains to include in the simulation based on given significance criteria which the user can alter. Significance criteria used in this research was any one of mass, activity, or reaction rates greater than $1\text{x}10^{-10}$. The CINDER90 code then uses Markovian chains to solve for differential contributions to the concentration of a nuclide from all nuclide chains that have production/destruction mechanisms for the nuclide of interest in essence linearizing the chosen set of equations. These partial nuclide densities $(\mathrm{N_i})$ are summed to obtain the total nuclide density$(\mathrm{N_m})$. The computation to solve for $N(t)$ of

the i^{th} element is only coupled to the $(i-1)^{th}$ element for which all parameters are assumed known:

$$\frac{dN_i}{dt} = -N_i(t)\beta_i + N_{i-1}(t)\gamma_{i-1} + \overline{Y}_i.$$

The significance criteria involves calculating the passby parameter $P_m(t) = \int_0^t N_m(t)\beta_m \, dt$ which is essentially the probability that a nuclide will produce another nuclide in a given time interval. If this probability is found to be insignificant (as determined by the user), the transmutation chain is terminated.

To capture the temporal evolution of reaction rates within a system such as a reactor core, the CINDER90 code must be coupled with a steady-state reaction rate calculator. MCNP provide this capability, supplying CINDER90 with updated reaction rates at each user determined time interval. Thus, in a typical MCNPX depletion simulation, an initial material composition is provided to MCNP via the user input deck. MCNP is used to calculate material specific neutron fluxes and reaction rates using a standard five-group structure. These neutron flux and reaction rate tallies are convoluted to produce an effective one-group flux and reaction rate by which an effective one-group cross section is determined and passed to CINDER90. The CINDER90 module then uses this material specific one-group cross section along with its extensive nuclide data set to perform a fuel depletion calculation to obtain new nuclide densities for each material at the end of the user specified time interval. These material densities are returned to MCNPX for the transport simulation of the next time step to be performed. This process is repeated until all time steps specified by the user in the input deck have been completed.

3.2.4 Single Channel Analysis Tool for Thermal Hydraulics

The Single Channel Analysis (SCA) tool for thermal hydraulics analysis for this research is developed in Python and uses analytical models and equations to determine axial fuel and coolant temperature distributions within each assembly in the reactor core. The SCA focuses the thermal hydraulics and thermodynamic analysis efforts on a single isolated vertical flow fuel assembly channel. Typically the hottest channel is used to set a conservative upper bound on temperatures, heat fluxes, pressure drop and other quantities for the entire assembly.

In the previous research, solutions for the radial and axial fuel element temperature distributions were derived[43] and are reproduced here for convenience. In the radial direction, the fuel, gap and clad temperature distributions are determined by using the core power distribution determined from MCNP to appropriately distribute the total core power (Q) through out the fuel pins. By definition, Q''' is the core power density, q_{FE} is the average pin power, $q'''_{FE}(r)$, $q''_{FE}(S)$ and $q'_{FE}(z)$ are the average volumetric, surface and linear heat generation rates, respectively.

The linear heat generation rate is used in the heat equation $q'_{FE}(r) = -k\frac{dT}{dr}$ applying Fourier's Law of Heat Conduction. In order for an analytical solution to be found, certain assumptions must be made. These include assuming steady-state heat transfer, one-dimensional thermal conduction, constant and evenly distributed fission heat source and constant material properties. The peaking factors $q'_{FE,max} = F^{P}_{tot} \times q'_{FE}$ can be applied and the solutions for the temperature distributions in the fuel, gap and clad found:

$$T_F(r) = T_{max} - \frac{q'''_F}{4k_F} r^2; \qquad 0 \le r \le r_F$$

$$T_G(r) = T_{CI} + \frac{q'''_F r^2}{2k_G} \ln\left(\frac{r_C}{r}\right); \qquad r_F \le r \le r_{CI} \text{ and}$$

$$T_C(r) = T_{CI} + \frac{T_{CI} - T_{CO}}{\ln\left(\frac{r_{CO}}{r_{CI}}\right)} \ln\left(\frac{r_{CI}}{r}\right); \quad r_{CI} \le r \le r_{CO}$$

where $T_F(r)$, $T_G(r)$ and $T_C(r)$ are the temperature distributions in the fuel, gap and clad, T_{max}, T_{CI} and T_{CO} are the temperatures at the centre of the fuel, the inner surface of the clad and the outer surface of the clad and r_F, r_{CI} and r_{CO} are the radii of the fuel region, inner surface of the clad and outer surface of the clad

Using Newton's law of cooling $q'' = h(T_{CO} - T_b)$ in conjunction with a known bulk coolant temperature, the solution for temperature at the outer surface of the clad is found. By summation of the temperature changes over each region of the fuel element, the maximum centerline temperature is $T_{max} = T_{CO} + \frac{q'}{2\pi f_F}\left[\frac{r_F}{2k_F} + \frac{r_{CI} - r_F}{k_G} + \frac{r_{CO} - r_{CI}}{k_C}\right]$.

In the axial direction, from nuclear reactor theory, the neutron flux shape for a bare cylindrical reactor with extrapolated height $(\tilde{H})$ is a cosine functional. This functional form is assumed and imposed on the axial linear heat flux which can then be approximated by $q'(z) = q'_{FE} \times F^P_{tot} \times \cos\left(\frac{\pi}{\tilde{H}} z\right)$. The heat conduction equation is solved analytically for each region in the axial direction under the same assumptions as the radial case:

$$T_b(z) = T_{in} + \frac{q'_{max}}{\omega C_p}\left(\frac{\tilde{H}}{\pi}\right)\left[\sin\left(\frac{\pi}{\tilde{H}} z\right) + \sin\left(\frac{\pi H}{2\tilde{H}}\right)\right]$$

$$T_{CO}(z) = T_{in} + q'_{max}\left[\frac{\tilde{H}}{\pi\omega C_p}\left\{\sin\left(\frac{\pi}{\tilde{H}} z\right) + \sin\left(\frac{\pi H}{2\tilde{H}}\right)\right\} + \frac{1}{2\pi h r_{CO}} \cos\left(\frac{\pi}{\tilde{H}} z\right)\right]$$

$$T_{CI} = T_{CO}(z) + \frac{q'_{max}}{2\pi k_C} \times \ln\left(\frac{r_{CO}}{r_f}\right) \cos\left(\frac{\pi}{\tilde{H}} z\right)$$

$$T_F(z) = T_{in} + q'_{max}\left[\frac{\tilde{H}}{\pi\omega C_p}\left\{\sin\left(\frac{\pi}{\tilde{H}} z\right) + \sin\left(\frac{\pi H}{2\tilde{H}}\right)\right\} + \Delta T_{FE}\cos\left(\frac{\pi}{\tilde{H}} z\right)\right]$$

where $\Delta T_{FE} = \frac{1}{2\pi h r_{CO}} + \frac{1}{2\pi k_C} \times \ln\left(\frac{r_{CO}}{r_F}\right) + \frac{1}{2\pi k_G} \times \ln\left(\frac{r_{CI}}{r_F}\right) + \frac{1}{4\pi k_f}$.

3.2.5 SIGACE for Doppler Broadened Neutron Cross Sections

SIGACE is a code package developed by the International Atomic Energy Agency as a tool for MCNP users to generate Doppler-broadened cross section data sets from standard MCNP cross sections. Within the package, any standard MCNP cross section can be Doppler broadened to a higher temperature in Evaluated Nuclear Data File (ENDF) format. ENDF/B-VII cross section data were used in this research. The standard MCNP cross sections are stored in the A Compact ENDF (ACE) file format and must be first converted to ENDF format using the ACELST module of the SIGACE code package and then broadened by the SIGMA1 module. An ACE file from the output of the SIGMA1 module is generated for use in MCNP.[45 53]

Over the 600 °K – 1500 °K range of temperatures that are of interest, cross section data sets are available only at three temperatures; 600 °K, 900 °K and 1200 °K. To further increase fidelity of the model, Doppler broadened cross section data sets were generated using the SIGACE code package. The data sets allow the Doppler broadening behavior of fuel temperature distribution to be incorporated into the MCNPX model.

The SIGACE code package was used to generate data sets for ^{235}U, ^{238}U, ^{239}Pu and ^{240}Pu over the temperature range of 600 °K to 1500 °K at 50 °K intervals. These

radionuclides represent the major contributors to the fission and resonance absorption reactions in a thermal spectrum for low-enriched uranium fuel. The thermal radiative capture cross sections for ^{238}U and ^{240}Pu are compared to the thermal fission cross sections for ^{235}U and ^{239}Pu in Figure 4. The neutron absorption cross sections for xenon-135 and samarium-149 (major parasitic neutron absorbers) are also shown. The data were taken from JANIS 4.0.[54]

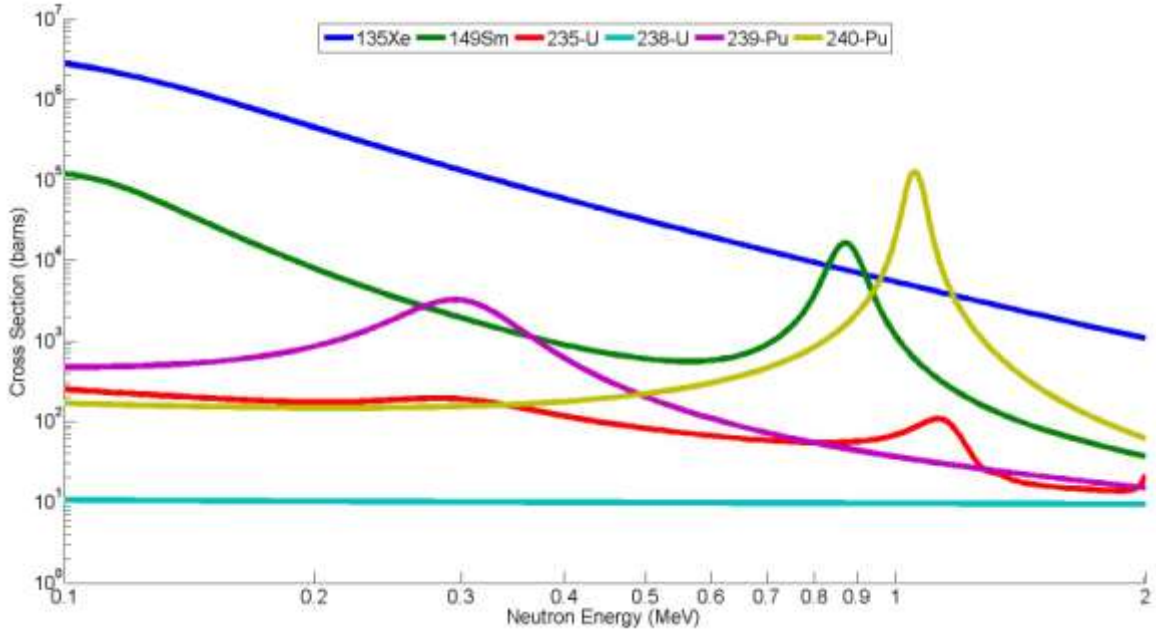

Figure 4: Cross section Behavior of Important Nuclides at Thermal Energies

4 METHODOLOGY VERIFICATION – BENCHMARK PROBLEM

4.1 The Need for Benchmarking

As discussed in the previous section, the Monte Carlo Method is very suitable for high fidelity modeling of the reactor core due to its ability to incorporate complex user-defined three-dimensional geometries and its use of continuous cross section data. In fuel transmutation, activation and burn-up simulations, the user divides the total simulation time duration into smaller time steps. The size of each step is chosen such that any changes in the shape of the neutron flux can be safely neglected. However due to the large computational time requirements of simulating a large number of particle histories in order to achieve convergence, the user is inclined to choose the largest possible time step to optimize between computational accuracy of the simulation results and computational time spent achieving the result. As such typical fuel depletion simulations using Monte Carlo radiation transport methods are typically run on time scales that are too long to capture the dynamic nature of the interplay between xenon-135 concentration and neutron flux levels to adequately resolve the xenon-induced, power oscillation phenomenon as needed in this research.

Additionally, the stochastic nature of the Monte Carlo method results in artificial asymmetries arising during a single time step simulation which is then propagated to the next time step as a genuine asymmetry. In situations where the solution is known to be symmetric, any one single Monte Carlo simulation will give asymmetric results that are "symmetrical within error". In most cases however, these results would be deemed acceptable for application to the dissertation research, such asymmetries from one time step to the next have been demonstrated to engender an oscillatory behavior which is unphysical.[55] Attempts have

been made to eliminate the inherent stochastic instabilities in Monte Carlo codes that cause these "phantom oscillations".[56 57 58 59 60]

In order to validate the results generated by application of the developed methodology to a generic SMR model, a benchmark problem is considered where the xenon-induced power oscillation phenomena that the methodology is designed to capture, are indeed present. The MCNPX simulations were executed using an MPI parallel installation version of MCNPX 2.7 on a 32 core, 2.7 GHz, 64 GB RAM desktop workstation. The coupling of MCNPX and the SCA tool was done using Portable Python 2.7.6.1.

4.2 Description of Benchmark Model

The chosen benchmark model was based on startup physics tests performed at Yonggwang Unit 3 (Korea Electric Power Corporation) on which previous benchmarks have been performed using an analytical model, and the two-group, three-dimensional diffusion code ROCS.[61 62] The representative core data for benchmarking calculated using the ROCS code and measured, are reproduced in Table 1.

Without additional information regarding the reactor state, a model representative of a 1D homogenized diffusion simulation was developed in MCNPX with similar physical and neutron transport characteristics. Matching individual parameters in Table 1 directly through trial and error was an impossible task and as such the objective in the model development was to obtain similar neutronic behavior by achieving similar ratios between the fast-to-thermal fluxes, fast-to-thermal absorption cross sections, fast-to-thermal fission cross sections, iodine and xenon atom densities and the number of neutrons produced per fission.

Table 1: Reference Core Data for Benchmark by Simulation

Parameters	Calculated Values (ROCS)	Measured Values
Active Fuel Height H (cm)	381	381
Iodine and Xenon Decay Constants λ_I, λ_{Xe} (s^{-1})	2.924×10^{-5} , 2.100×10^{-5}	2.924×10^{-5} , 2.100×10^{-5}
Iodine and Xenon Fission Yields γ_I, γ_{Xe}	6.325×10^{-2} , 9.691×10^{-5}	6.353×10^{-2} , 2.678×10^{-5}
Two Group Neutron Flux ϕ_1, ϕ_2 ($cm^{-2}s^{-1}$)	2.803×10^{14} , 6.275×10^{13}	1.366×10^{14} , 3.117×10^{13}
Iodine and Xenon Atom Densities $\bar{N}_I, \bar{N}_{Xe}$ (cm^{-3})	6.437×10^{15} , 1.817×10^{15}	3.224×10^{15} , 1.497×10^{15}
Two Group Diffusion Coefficients D_1, D_2 (cm^{-1})	1.336 , 4.093	1.320 , 4.005
Two Group Absorption Cross Sections $\sum_{a1}, \sum_{a2}$ (cm^{-1})	8.659×10^{-3} , 7.294×10^{-2}	8.652×10^{-3} , 7.480×10^{-2}
Total Reaction Cross Section $\sum_R$ (cm^{-1})	1.637×10^{-2}	1.711×10^{-2}
Two Group Fission Cross Sections $\sum_{f1}, \sum_{f2}$ (cm^{-1})	2.259×10^{-3} , 3.733×10^{-2}	2.254×10^{-3} , 3.7723×10^{-2}
Neutrons Produced per Fission ν	2.454	2.469
Xenon Cross Section σ_{Xe} (cm^{-2})	1.313×10^{-18}	1.431×10^{-18}
Power Reactivity Coefficient α_p (cm^{-1})	-2.484×10^{-4}	-2.697×10^{-4}

The geometry of the final benchmark model is presented in Figure 5. The geometry consisted of two annular fuel regions representing the top and bottom regions of the core. Reflective boundary conditions were imposed in the radial direction essentially making the model one dimensional in the axial direction. In the axial direction, two water regions served as axial reflectors.

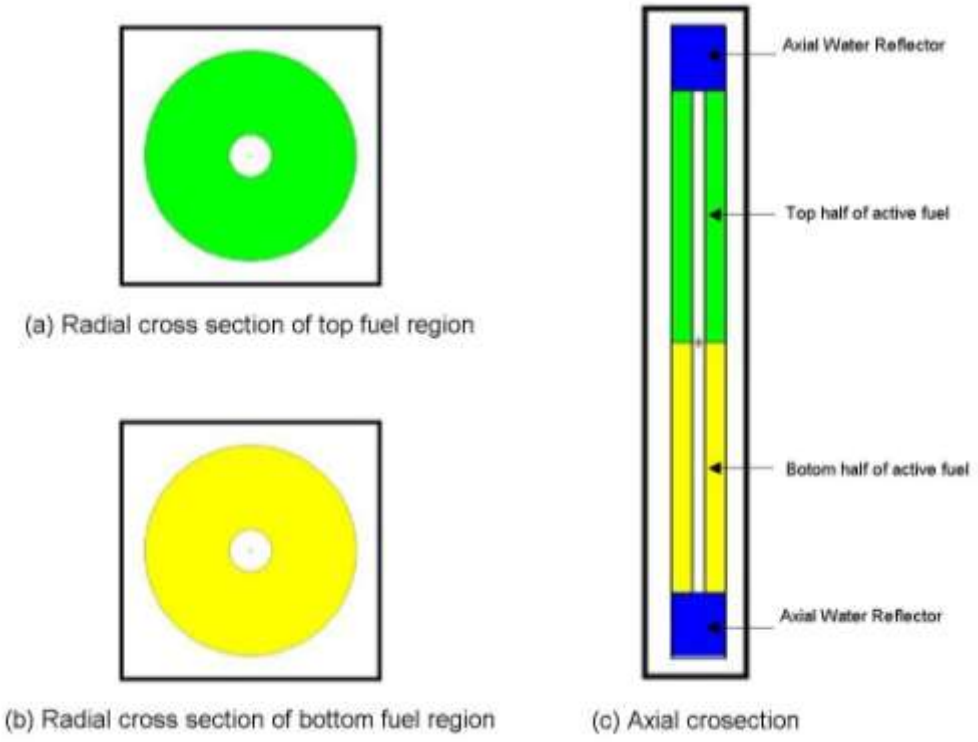

Figure 5: Benchmark Model Geometry

Table 2 compares characteristics of the benchmark model developed to the values in literature by calculating the ratio of the parameters of developed model and of the ROCS code to the reference measured values. A majority of the parameters in Table 2 are within five percent agreement with the Benchmark values. However, there are discrepancies in the two-group fission cross sections. Thus, while exact results are unlikely, the proximity of overall system parameters suggests the model should exhibit significant oscillatory behavior sufficient for benchmarking of the developed methodology.

Table 2: Comparison of Simulation Model Parameters to Reference Data

Parameters	Benchmark ROCS Vs. Measured values	Benchmark model Vs. Measured values
Ratio of Active Fuel Height H (cm)	1.00	1.00
Ratio of Two Group Neutron fluxes ϕ_1/ϕ_2	0.98	0.95
Ratio of Iodine and Xenon Densities $\bar{N}_I/\bar{N}_{Xe}$	0.61	0.61
Ratio of Two Group Absorption Cross Sections $\sum_{a1}, \sum_{a2}$	1.00 , 1.03	0.97 , 1.04
Ratio of Two Group Fission Cross Sections $\sum_{f1}, \sum_{f2}$	1.00 , 1.01	0.71 , 1.10
Ratio of Neutrons Produced per Fission ν	1.01	1.00

4.3 Results of Benchmark Simulations

The test was performed at a cycle burn-up of 0.35GWd/MTU at fifty percent power. The oscillation was initiated by a control rod bank insertion into the entire top region of the core for six hours before removal. Measured data was collected over the first eighty hours of the test and the axial separation index (ASI) was calculated. The observed oscillation was stable (self-regulating) in nature with a period of approximately thirty-two hours and a maximum ASI of approximately twenty percent.[69] [70] The axial separation index also known as the Power Axial Offset (PAO) is defined by $\%\text{Power Axial Offset} = \frac{(\mathrm{P_{bot}} - \mathrm{P_{top}})}{(\mathrm{P_{bot}} + \mathrm{P_{top}})} \times 100$, where P_{bot} and P_{top} are the power in the bottom and top regions of the core, respectively. In addition to the Power Axial Offset (PAO), the Xenon Axial Offset (XAO) parameter also serves as a quantitative measure of xenon stability and defined in a similar manner: $\%\,\text{Xenon Axial Offset} = \frac{(\mathrm{Xe_{bot}} - \mathrm{Xe_{top}})}{(\mathrm{Xe_{bot}} + \mathrm{Xe_{top}})} \times 100$ where $\mathrm{Xe_{bot}}$ and $\mathrm{Xe_{top}}$ are the masses of xenon in the bottom and top regions of the core, respectively.

The results for the same test in the benchmark model are shown in Figure 6. As expected the results were not directly comparable to the literature with the observed oscillation being unstable in nature with a period of approximately twenty-nine hours. The magnitude of the oscillation increased over the simulation time with a largely consistent oscillation period. Nevertheless, an oscillatory behavior similar to that of the benchmark was observed and the period was consistent with the literature and that expected in the benchmark within ten percent relative error. XAO results are presented in Figure 7.

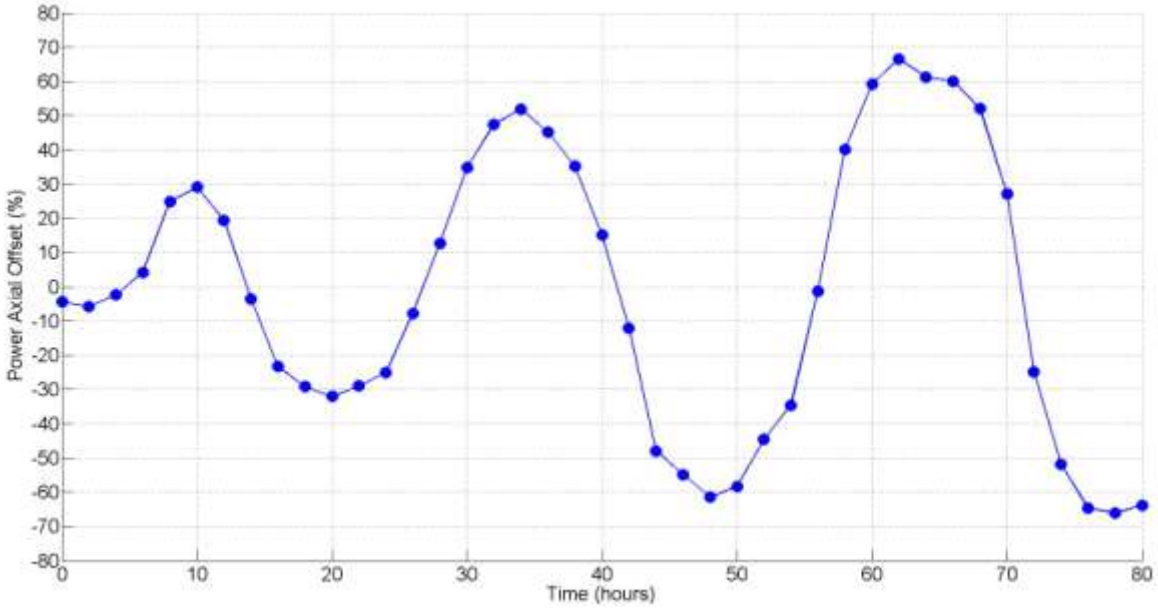

Figure 6: Benchmark Model Power Axial Offset with Height at 381 cm

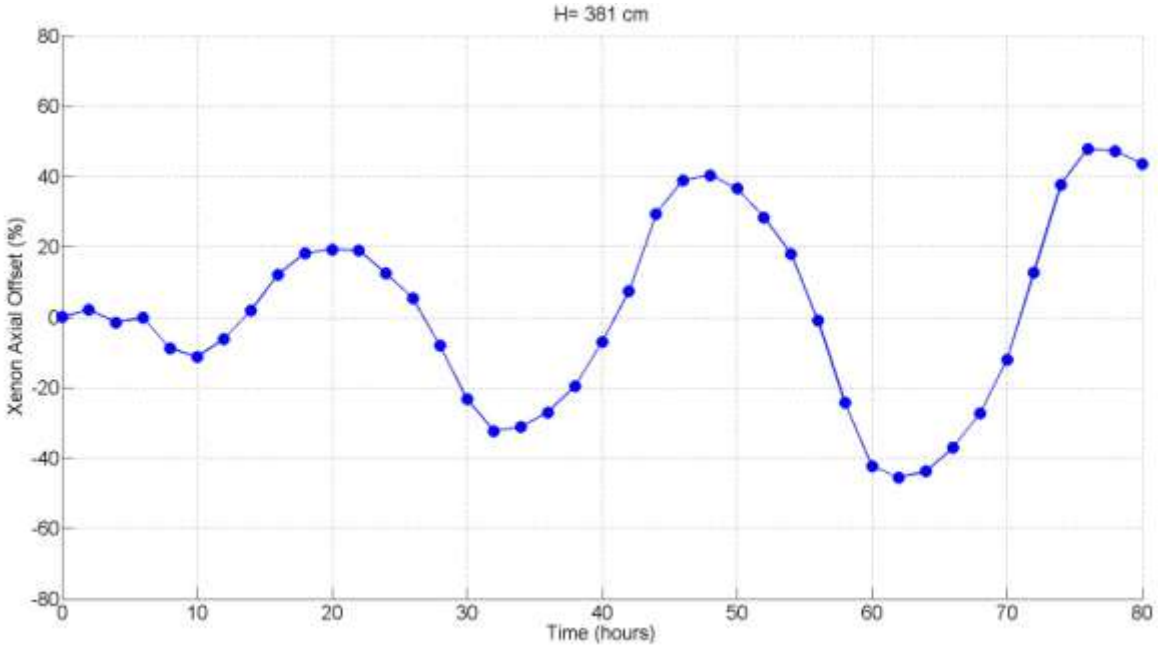

Figure 7: Benchmark Model Xenon Axial Offset with Height at 381 cm

Three additional cases were simulated with heights of 310, 240 and 110, centimeters respectively. The simulations were done to further confirm that the fundamental physics behind xenon-induced power oscillations were indeed being captured by the developed methodology. In these simulations, the observed unstable nature of the oscillations in the full height simulation was expected to decrease, stabilize and eventually disappear as the flux in the two regions of the benchmark model become more tightly coupled with decreasing model height. Figure 8 shows a comparison of the results from the simulated cases. In this figure, the case with a 310 cm height exhibits a reduced oscillation magnitude and a period of approximately twenty-five hours. Closer inspection reveals a stable oscillation with decreasing magnitude and period. The cases with 240 cm and 110 cm heights are very stable with no observable xenon-induced power oscillations. After the initial offset due to the control rod motion, a stochastic oscillation was observed at the five and two percent level in the 240 and 110-centimeter models, respectively.

The physics governing xenon-induced power oscillations indicates that the behavior of the xenon axial offset should be equal to the power axial offset with respect to oscillatory nature, but 180 degrees out-of-phase. Thus, a maximum in the PAO should be coincident with a minimum in the XAO and vice versa. The results of the case with a height of 381 centimeters are presented in Figure 7 and from comparison of the PAO results in Figure 8 and the XAO results presented in Figure 9, this out-of-phase relationship between the PAO and XAO parameters was observed..

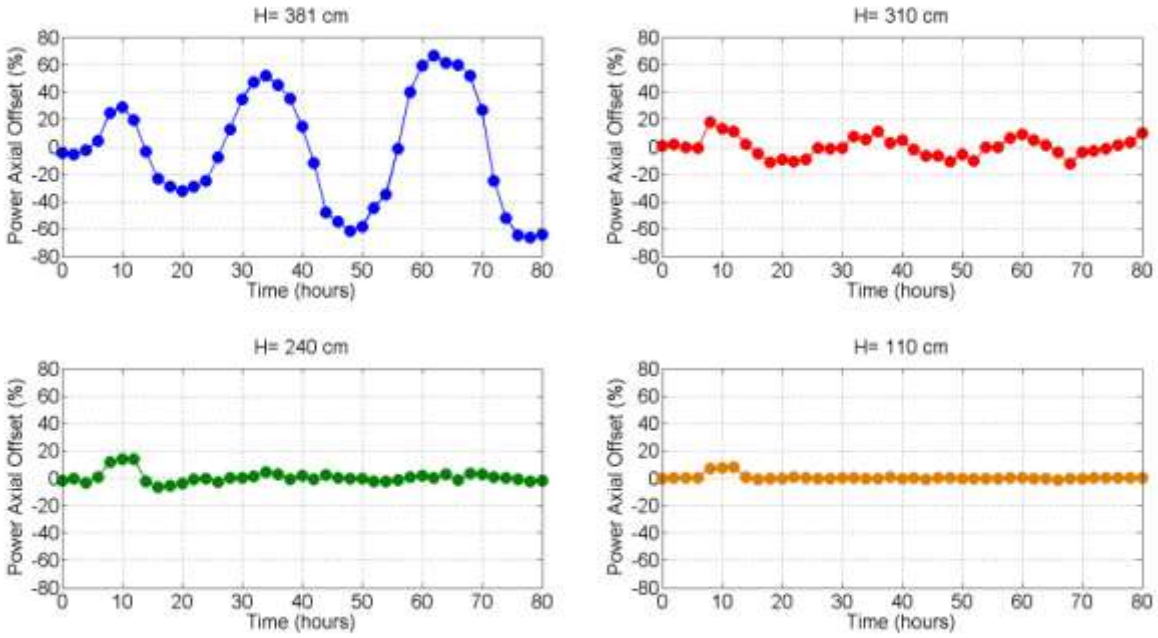

Figure 8: Benchmark Model Power Axial Offset at Various Heights

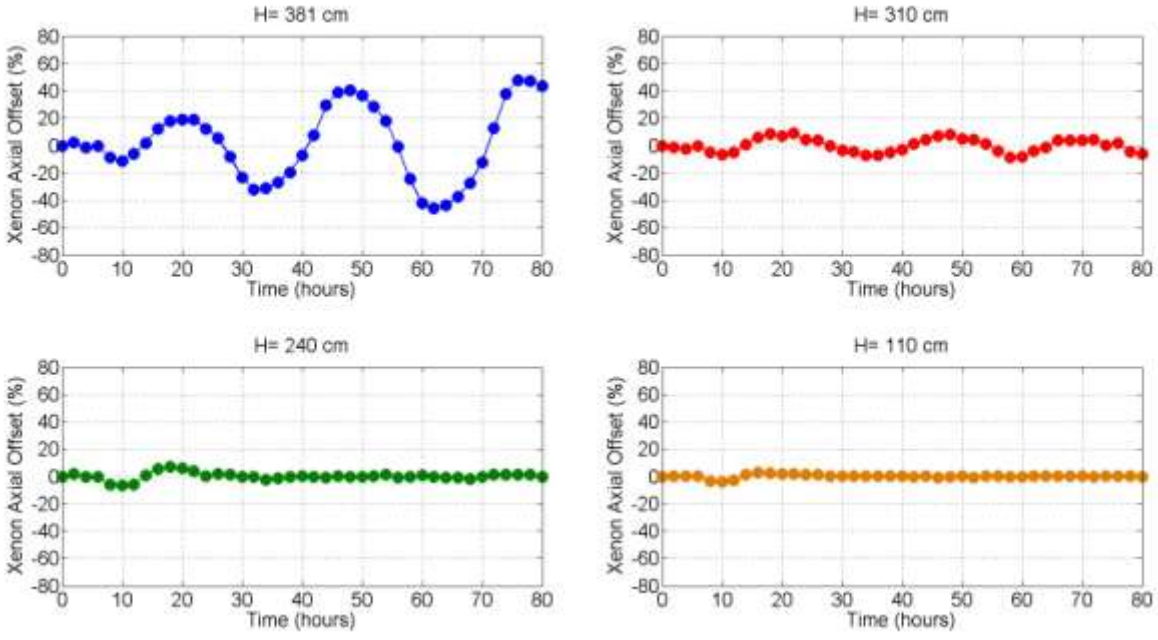

Figure 9: Benchmark Model Xenon Axial Offset at Various Heights

5 SMR CORE MODEL

The objectives of the research as presented in Section 1.4 were two-fold. In Sections 3 and 4 the first objective was accomplished; namely the development and benchmarking of a multi-physics computational methodology capable of high fidelity safety analysis. The second objective was to apply the developed methodology to assess the threat posed from xenon-induced power oscillations to a generic small modular reactor core. In this section, the development of the computational model of the SMR in MCNPX is presented in Section 5.1 and the requirements for high fidelity within the model implemented in Section 5.2.

5.1 SMR Simulation Model Parameters

The model used as the starting point for the final SMR simulation model was developed as part of research where a safety and performance analysis was conducted for a generic small modular reactor core.[43] The generic SMR core model was developed based on the proposed performance characteristics of the B&W mPower SMR as publically available in 2012, which at the time represented the most advanced iPWR SMR design in the United States.[63] With the available information, a generic core was developed capable of producing 530 MW of thermal power for a core life-time of four years at ninety-five percent capacity factor in keeping with observed commercial capacity factors for currently operating nuclear power plants in the United States.[64] The fuel enrichment was limited to five percent uranium-235. Burnable absorber rods (BARs) with boron carbide as the absorber material were used to shape the core power profile. Through a combination of neutronics and depletion simulations, an optimized core loading pattern was established. Optimized fuel assembly and core parameters are shown in Table 3 and Table 4, respectively.

Table 3: SMR Fuel Assembly Parameters

Parameter	Value
Fuel Material	UO_2 (LEU)
Gap Material	Helium
Clad Material	Zircaloy-4
Fuel Pellet Diameter	0.784 cm
Gap Outer Diameter	0.816 cm
Clad Outer Diameter	0.930 cm
Fuel Rod Lattice Pitch	1.260 cm

Table 4: Optimized SMR Core Parameters

Parameter	Value
Height-to-Diameter Ratio	1.23
^{235}U Enrichment	4.4 and 4.95 at% ^{235}U
Total Fuel Mass	22.4 tons
Average Fuel burn-up	39.45 GWd/MTU
Radial Power Peaking Factor	1.24
Axial Power Peaking Factor	1.09

The simulation model was a three-dimensional full core model in MCNP5[46] and MCNPX[47] and was assessed for safety by calculating reactivity coefficients, point reactor kinetics parameters, and axial and radial core neutron flux and power distributions. A thermal hydraulics Single Channel Analysis (SCA) assessment was performed by calculating the radial and axial temperatures at the fuel centerline, at clad inner surface, at clad outer surface and in the bulk coolant, respectively. The Critical Heat Flux (CHF) and Departure from Nucleate Boiling Ratio (DNBR) distributions were also calculated for the ten percent overpower scenario and found to be within safe operation limits set for low-enriched uranium fueled light water reactors as specified in the Code of Federal Regulations.[65] Figure 10 shows axial and radial cross sections of an individual assembly.

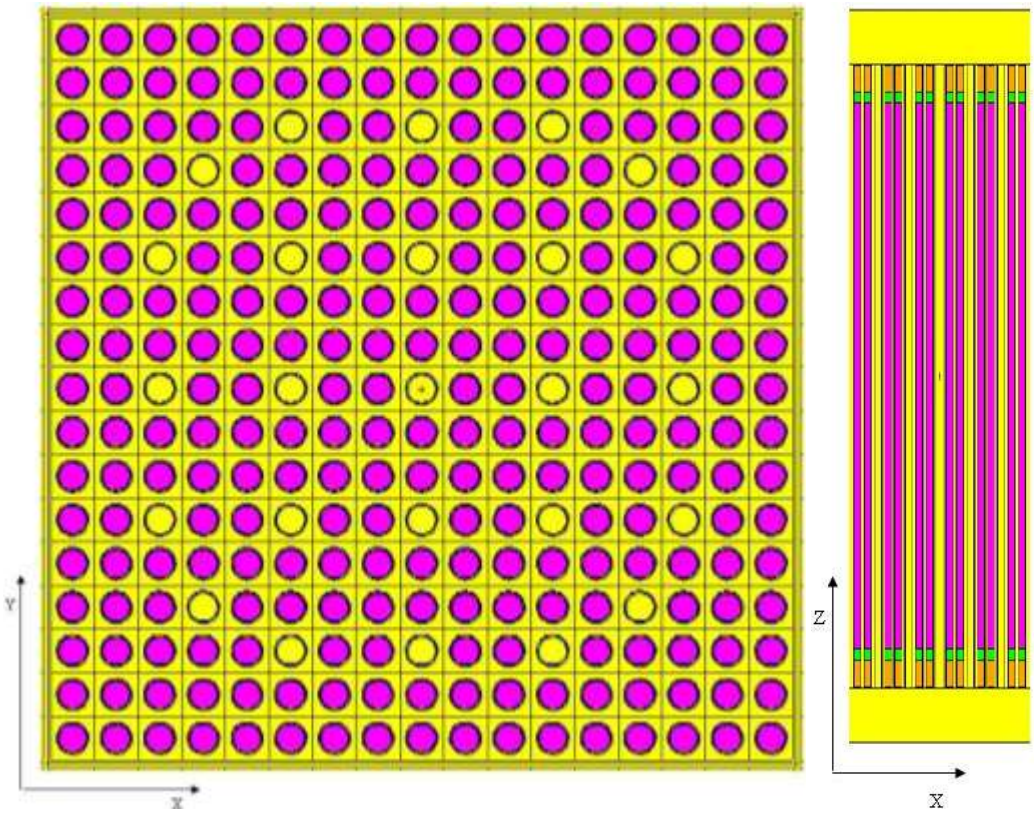

Figure 10: Radial and Axial Cross Sections of the SMR Fuel Assembly

5.2 High Fidelity Modeling Requirements for Final SMR Simulations

As mentioned in Section 2.4, the developed simulation methodology must possess sufficient fidelity with respect to the determination of the spatial shape of the neutron flux within the iPWR SMR core. Thus, the complexity of the SMR simulation model described in Section 5.1 was increased by employing spatial discretization within the active fuel region in the core geometry. In addition, the temporal discretization scheme, featuring two-hour depletion simulation time-steps employed in Section 4.2 while validating the methodology, was retained.

Taking advantage of the radial symmetry of the optimized core model, a one eighth core model was developed; significantly reducing computational time of the depletion simulations. This model featured thirteen unique assembly locations as shown in Figure 11.

Each assembly was subsequently divided axially into eight segments. Each axial segment was given its own material definition in MCNPX allowing for axially dependent flux and isotopic concentrations within the fuel to be tracked in the depletion simulations.

Similarly coolant channels within the assemblies were divided into axial segments; one per axial fuel segment. Separate coolant volumes were also defined for the downcomer, lower plenum, core shroud and upper plenum. The fidelity of the SCA tool was also updated to allow coolant temperatures and densities for each of these volumes to be calculated. Core average coolant temperatures were calculated and assigned to the coolant volumes between assemblies. Figure 12 shows an axial cross section of the core model clearly showing the eight axial fuel segments, downcomer, lower plenum, core shroud and upper plenum coolant volumes.

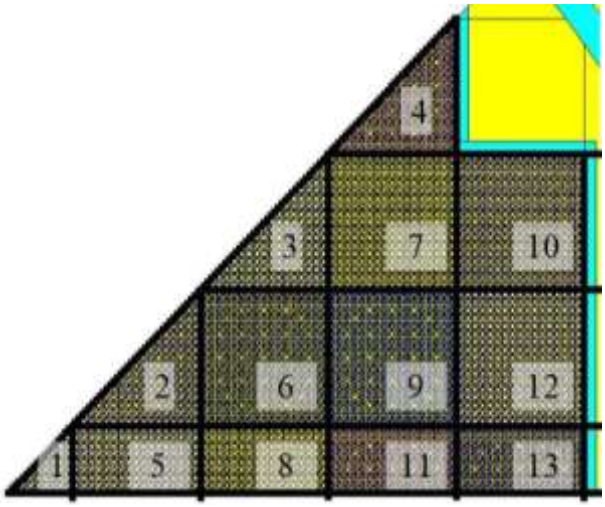

Figure 11: Radial Cross Section of SMR Model (Assemblies Numbered)

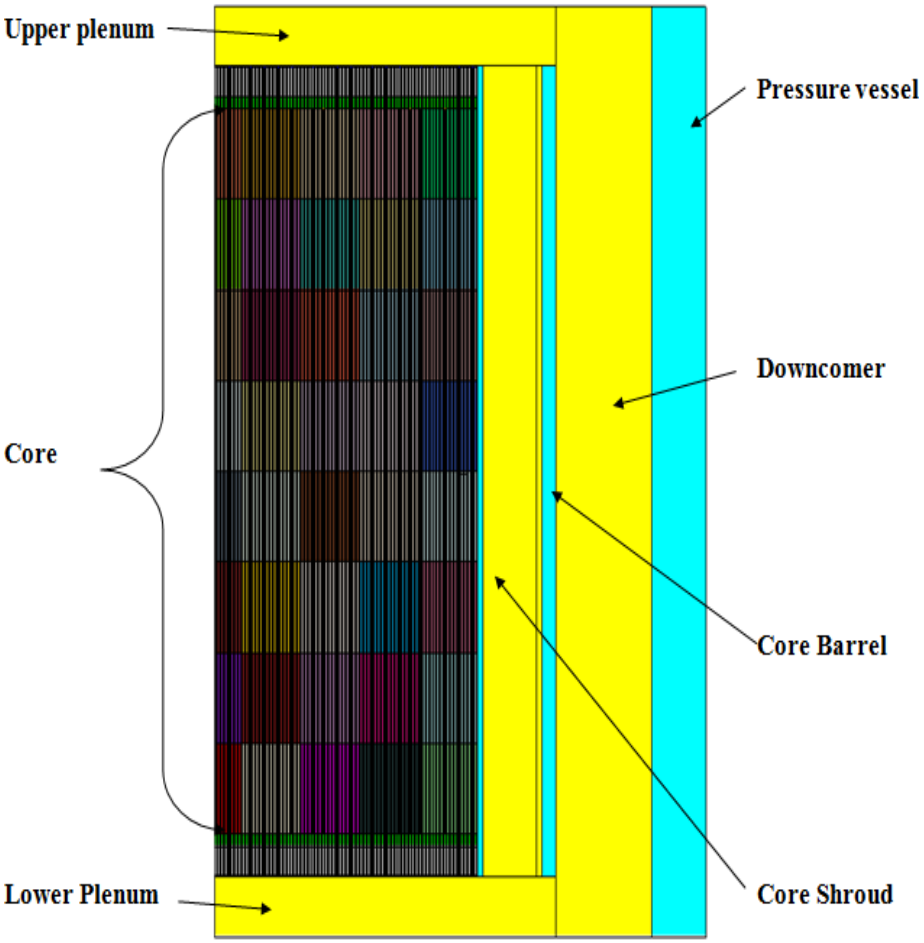

Figure 12: Axial Cross Section of SMR Model (Fuel Regions Visible)

6 RESULTS

Before assessing the threat posed to the reactor model by xenon-induced power oscillations, the developed methodology was applied to a typical depletion calculation to assess the effect of updating fuel material cross sections and coolant temperatures and densities at each depletion time step. The results of this preliminary assessment are presented in Section 6.1. The xenon stability results are presented for beginning of core life and end of core life in Section 0. Sections 6.3, 6.4 and 6.5 look at the sensitivity of the results to stochastic errors related to the Monte Carlo method, axial discretization and convergence of tallies in MCNPX, respectively. The results of a preliminary study of options for control within the SMR are presented in Section 6.6.

6.1 Effective Neutron Multiplication Factor and Fuel Burn-up

With respect to the effective neutron multiplication factor, a significant reduction is expected due to the net decrease in reactivity associated with the Doppler broadening of the uranium-238 radiative capture cross section. This effect is clearly visible in Figure 13 which shows the effective multiplication factor for the improved model (featuring eight axial regions, updated fuel temperatures and coolant densities) compared to that of the basic model for the first 350 days of the core life-time. Fuel burn-up as a function of time is also displayed in Figure 13 at the beginning of core life (BOL) for the SMR core. By implementing fuel material temperatures in the shape of updated material cross sections, all eight regions of the fuel were modeled with increased fuel temperatures compared to the basic model of the previous research. The increase in fission reaction rate in uranium-235 is negated by increased resonance absorption of neutrons in uranium-238.

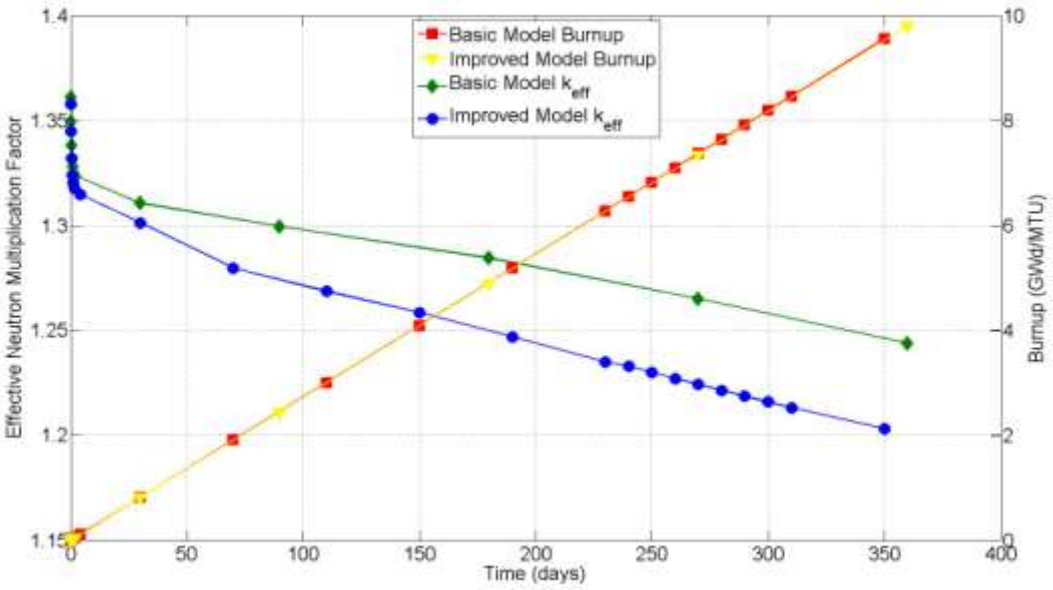

Figure 13: SMR Effective Neutron Multiplication Factor and Burn-up at BOL

The increase in resonance absorption leads to a net decrease in fission rate and a decrease in the effective multiplication factor. These effects are reinforced by increased coolant temperatures. The increased fuel temperatures are accompanied by increased coolant temperatures and decreased coolant region densities along the active fuel length. As the density decreases, the moderation offered by the coolant in the core also decreases resulting in a harder neutron spectrum and an accompanying decrease in effective neutron multiplication factor as expected in a reactor designed to operate in the thermal spectrum.

Burn-up increases linearly with time and remains the same as in the basic model. This result was expected since the amount of energy drawn from the core per unit time did not change. The first thirty days of the simulation are executed in time steps of 0.30, 0.30, 0.30, 0.30, 0.47, 2.33 and 26 days. This sequence was selected to allow xenon and other fission

products to build up to their equilibrium levels. Figure 14 shows the net xenon mass reaching saturation. After this point, forty-day time steps are used.

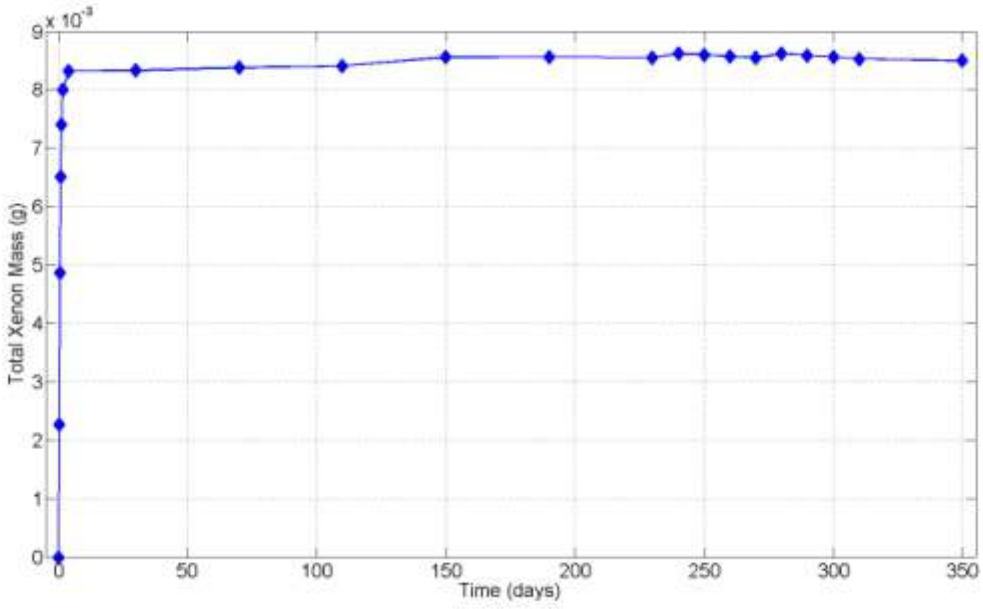

Figure 14: SMR Xenon Mass at BOL

As mentioned in Section 2.3.4, increased uniformity of the neutron flux distribution leads to decreased xenon stability. Thus, the evolution of the power and xenon distributions is of paramount importance. The evolution of the core-averaged axial power distribution is presented in Figure 15. After equilibrium xenon concentrations are established at thirty days, the axial power profile is "bottom-peaked" due to increased moderation (reactivity) as colder more dense coolant enters the core from the lower plenum. The "bottom-peaked" nature of the power profile is more pronounced in the central assembly and less so when the core

average distribution is calculated. With further depletion, the power profile become increasingly uniform as evident after 230 days.

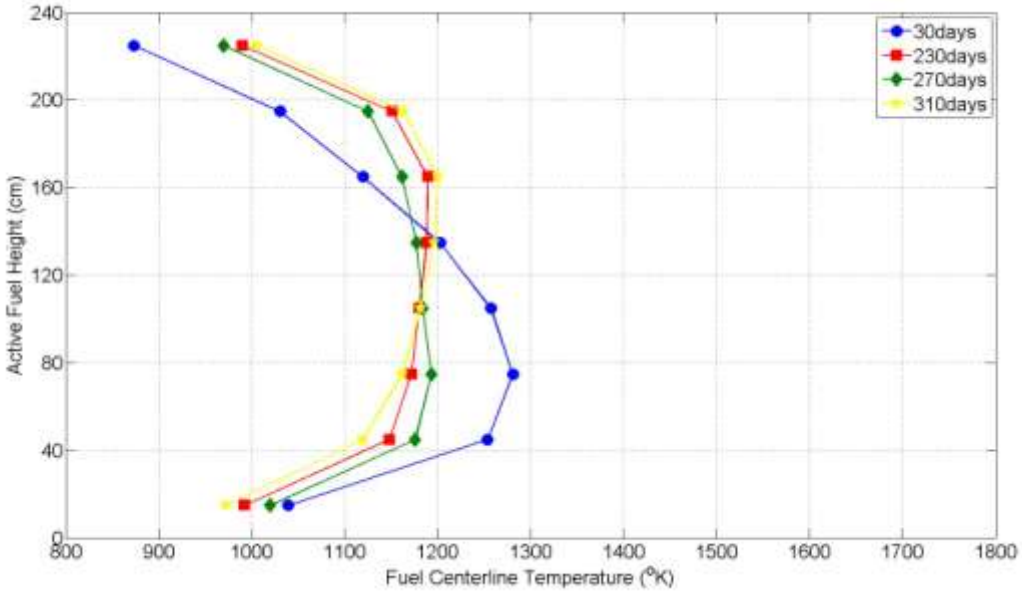

Figure 15: Evolution of Axial Power Distribution at BOL

The bottom region of the core experiences increased fission due to the increased moderation, however over time, this increased fission leads to increased depletion of the fissile isotope content in the fuel. As this occurs, the net reactivity of the bottom region of the core decreases and the power produced. Some stochastic variation is observed at subsequent time steps as the MCNP code attempts to enforce a constant power condition. This behavior is typical of Monte Carlo radiation transport simulations.

The evolution of the core averaged axial xenon distribution is shown in Figure 16. As expected, the same general trends are observed in the xenon distributions as in the power

distributions; namely the distribution is initially “bottom-peaked” and becomes increasingly uniform with fuel depletion. Naturally, the trends observed in the axial power distribution are also evident in the fuel centerline axial temperature distribution as the two are inextricably linked. Figure 17 shows the evolution of the core-averaged fuel-centerline axial temperature distribution. As the axial power distribution becomes increasingly uniform with time, so too does the fuel-centerline axial temperature distribution. From the figure, peak fuel centerline temperatures are well within safe operating limits for LEU fueled light water reactors as set forth in the Code of Federal Regulations (10CFR50.46).[65]

The core averaged bulk coolant axial temperature distribution is shown in Figure 18. As a result of the initial “bottom-peaked” nature of the axial power distribution, the rate of heat addition to the bulk coolant is at a maximum in the bottom coolant segments. As the axial power distribution becomes increasingly uniform, so too does the rate of heat addition to the bulk coolant resulting in a more linear increase in bulk coolant temperature with time. The core averaged outlet temperature is approximately 323 °C with an initial inlet temperature set at 297 °C. This is typical of existing PWRs. With the reactor vessel pressurized to 14.1 MPa, the bulk coolant is firmly within the subcooled boiling heat transfer regime[66] desired for safe operation.

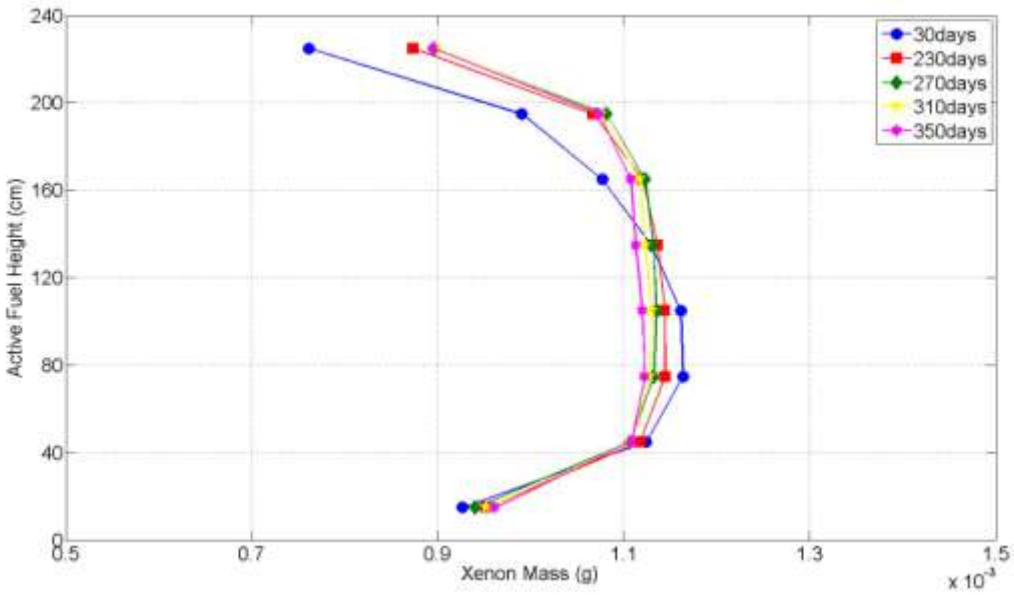

Figure 16: Evolution of Axial Xenon Distribution at BOL

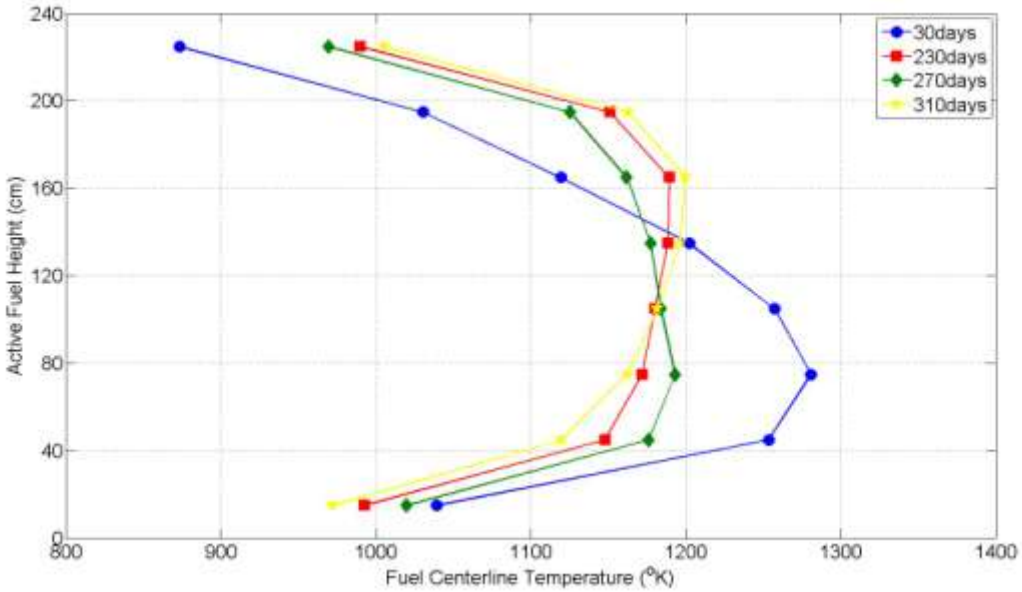

Figure 17: Evolution of Axial Fuel Temperature at BOL

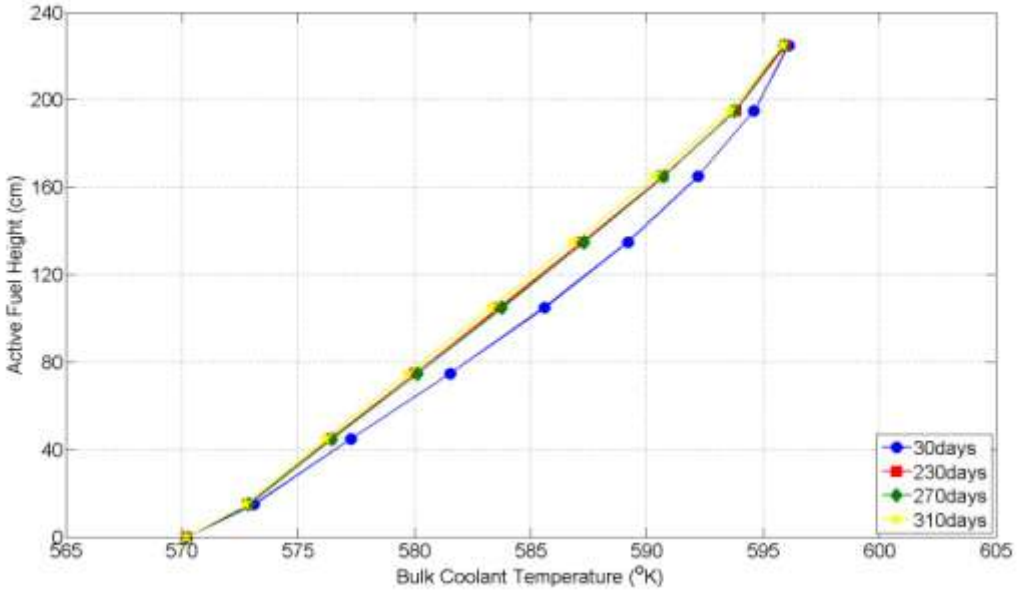

Figure 18: Evolution of Axial Bulk Coolant Temperature at BOL

6.2 Xenon Stability Results

Having validated the simulation methodology and confirmed anticipated behavior of various reactor physics phenomena, the developed methodology is applied to the simulation model to determine the threat posed by xenon-induced power oscillations present in the SMR core under study. Taking the seven factors affecting xenon stability as recognized in the literature into consideration, the physical core size and the core height to diameter ratio are fixed with the physical dimensions of the core and as such are time independent. The other five factors (thermal neutron flux level, neutron diffusion length, magnitude of the negative power coefficient, uniformity of the thermal flux distribution and fuel enrichment) are all material dependent, and hence time dependent due to depletion and transmutation of the fuel material. Of these five, only the neutron diffusion length acts to increase xenon stability over the life time of the core, while the others all tend to decrease xenon stability with the net

effect being a result in increased xenon instability. As such, it is expected that the core model will exhibit increased xenon stability at the Beginning of core Life (BOL) when the fuel is fresh compared to the End of core Life (EOL).

6.2.1 Beginning of Core Life Results

The test procedure used in the methodology validation section is repeated with the developed core model at BOL. The oscillation is initiated by a control rod bank insertion into the top region of the core for six hours before removal. Simulations are executed for the first eighty hours of the test in two-hour intervals and the Power Axial Offset is calculated. Two tests were performed with fresh fuel material definitions, one at full power (530 MW thermal) and the other at half power (265 MW thermal). The MCNPX simulations were executed using an MPI parallel installation version of MCNPX 2.7 on a 32 core, 2.7 GHz, 64 GB RAM desktop workstation. The coupling was done using Portable Python 2.7.6.1.

Figure 19 shows the effective neutron multiplication factor during the BOL tests at full and half power. The large difference at full power and half power is due to the equilibrium xenon concentrations reached in each case. At full power a higher thermal neutron flux level is attained and as such larger equilibrium xenon mass. The difference in the effective neutron multiplication factor is essentially the difference in xenon reactivity worth due to the different equilibrium fluxes.

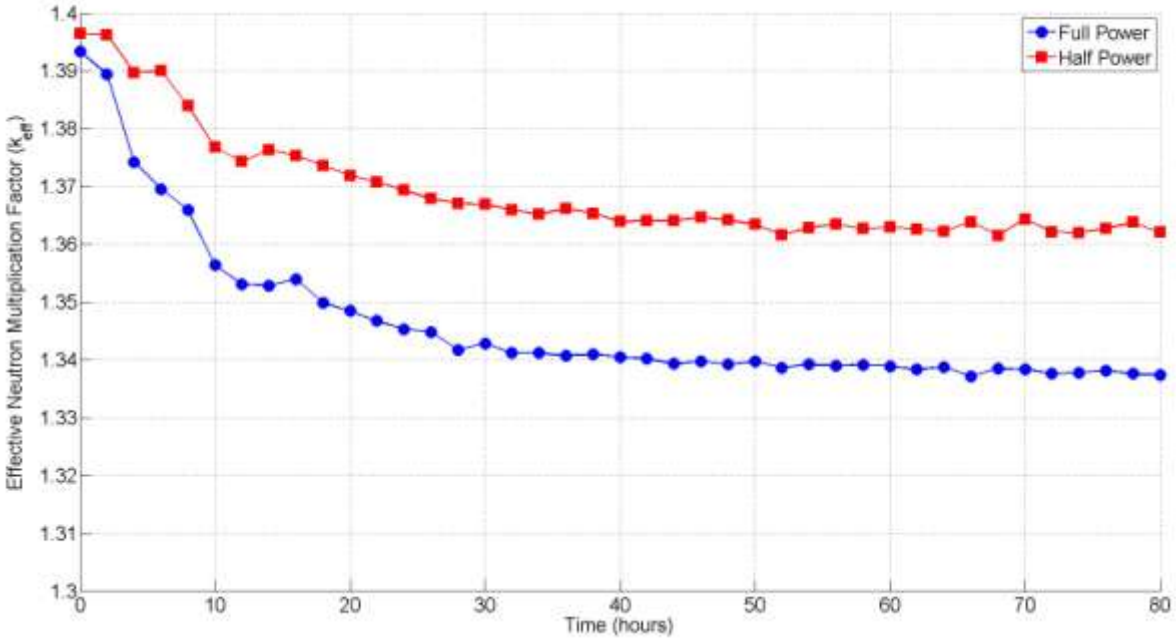

Figure 19: Effective Neutron Multiplication Factor during BOL Tests

The total xenon masses in the top and bottom regions of the core calculated at full and half power conditions are presented in Figure 20. As expected at BOL, the mass of xenon quickly builds up in the fresh fuel to reach an equilibrium level in keeping with the thermal flux level in each region of the core. The equilibrium xenon level in the full-power case is greater than that in the half-power case which is in keeping with expectations according to reactor theory. In order to increase power in a fixed geometry with fixed materials, the flux must increase. Additionally in both simulations, the xenon mass in the bottom region of the core is consistently greater than that in the top region of the core once again capturing the general bottom peak nature of the core power distribution due to the coolant density distribution.

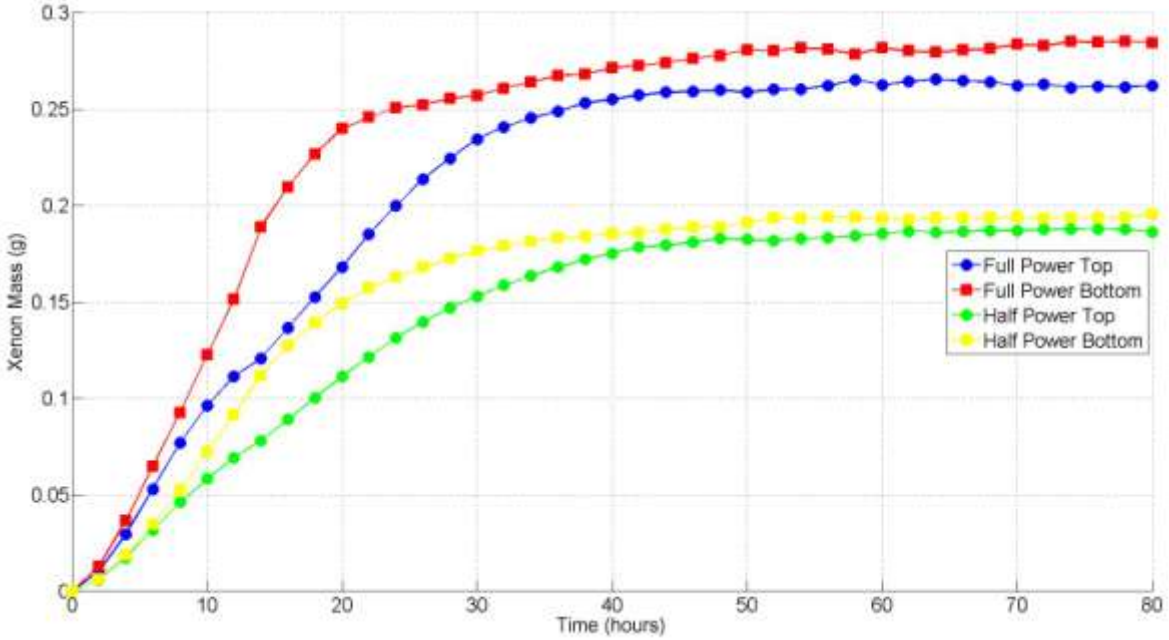

Figure 20: Xenon Mass during BOL Tests

During the test, the reactor is expected to go through four main phases. The first is the "pre-test" phase and is essentially the period of time before rod insertion. In this phase, the xenon concentration is rapidly building up the equilibrium levels for the flux levels associated with the full and half power conditions. The next phase or "rod insertion" phase is the period of time during which the control rod is inserted and maintained in the top region of the core. The control rod insertion results in an instantaneous change in the shape of the flux by depressing the flux in the top region of the core. Due to the constant power requirement, the power in the bottom region of the core increases to compensate for the decreased power production in the top region of the core. The third phase is the "oscillation" phase and is initiated by removal of the control rod from the top region of the core. It is in this phase that any inherent oscillatory behavior should be observed. The xenon stability is measured in a

“free oscillation mode” meaning that no control actions are taken to dampen the oscillation. The final phase is the “return to equilibrium” phase. Depending on the xenon stability of the core, a new equilibrium xenon distribution will be achieved after a few oscillation periods. If the core is inherently unstable, the return to equilibrium phase is not achieved in the free oscillation mode and control rod movement is required to regain control of core power.

The fraction of power produced in the top and bottom regions of the core during the tests at full and half power conditions are shown in Figure 21 and Figure 22, respectively. The rod insertion phase is clearly visible reducing the fraction of power produced in the top region of the core to approximately thirty percent. Removal of the control rod initiates the oscillation phase; characterized by the fluctuation of majority power production between the two regions of the core. This phase appears to persist for nearly thirty hours into the test at full power and twenty-four hours into the test at half power before returning to equilibrium. The corresponding average fuel centerline temperatures for tests are presented in Figure 23 and Figure 24. The general trends are consistent with those observed in the power fraction data. Maximum and minimum temperatures of approximately 1400 °K and 900 °K are experienced in the bottom and top regions of the core in the test at full power. At half power, the temperatures are reduced to approximately 1000 °K and 750 °K.

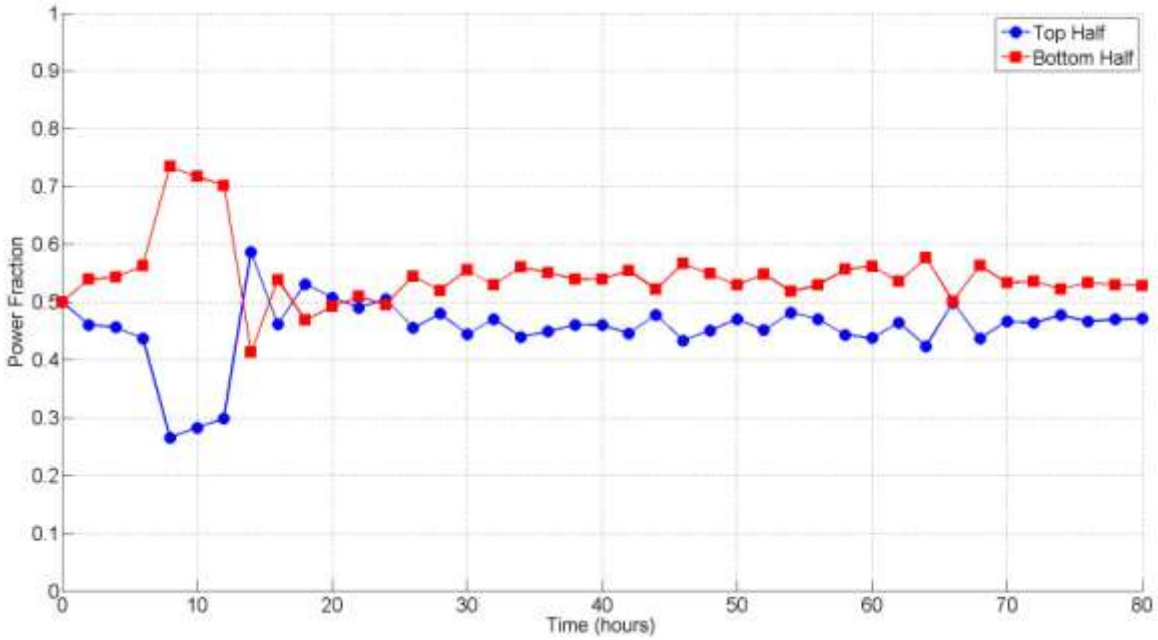

Figure 21: Power Fractions during BOL Tests at Full Power

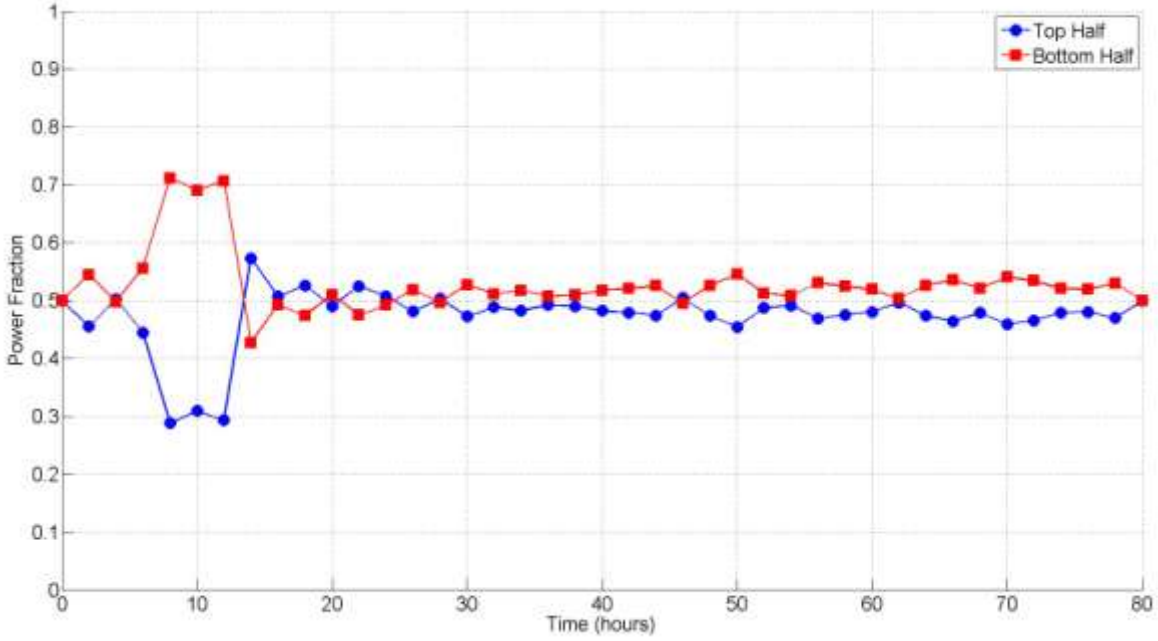

Figure 22: Power Fractions during BOL Tests at Half Power

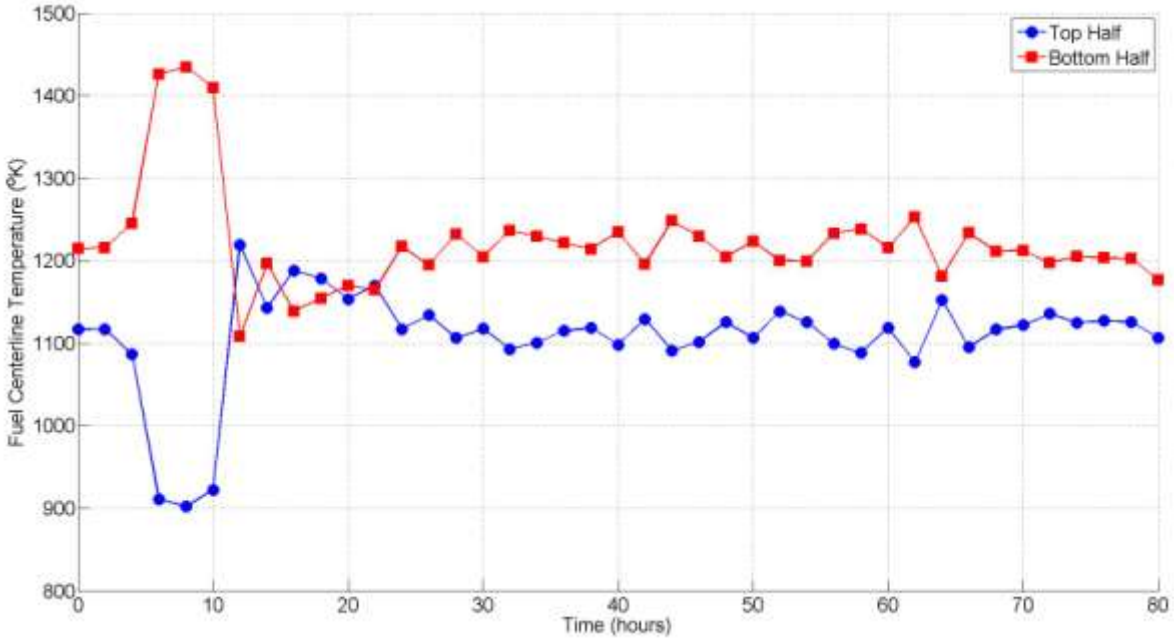

Figure 23: Average Fuel Centerline Temperatures during BOL Tests at Full Power

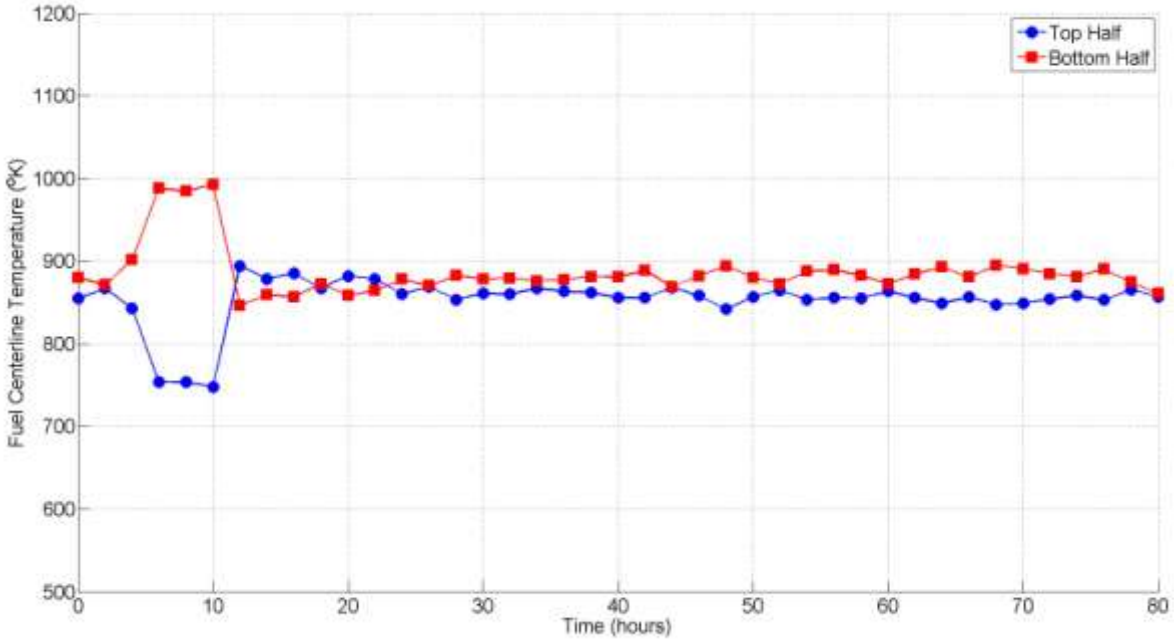

Figure 24: Average Fuel Centerline Temperatures during BOL Tests at Half Power

Using the power fraction data, power axial offset for the duration of the test was calculated. As predicted, the four main features of the test are evident in Figure 25.

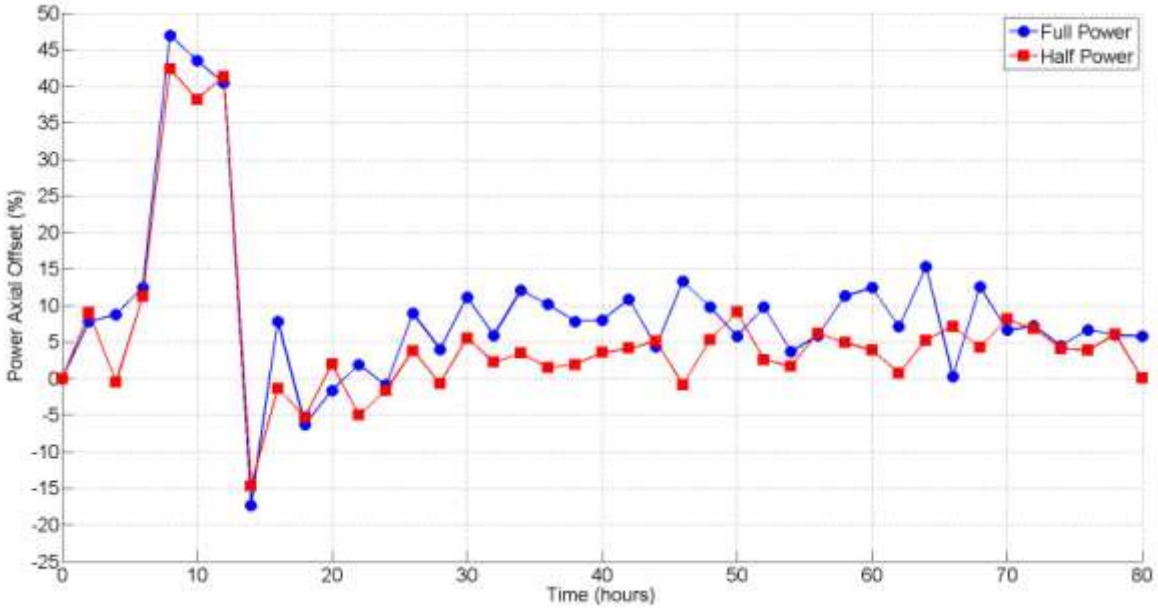

Figure 25: Power Axial Offset during BOL Tests

The first six hours of the test represents the pre-test phase where xenon concentration build up in both regions of the core are governed by the power requirement given via the MCNPX burn card. The next six hours of the test represents the rod insertion phase. As expected the depressed neutron flux in the top region of the core under the constant power requirement results in increased power production from the bottom region of the core. The resulting PAO is approximately forty-five percent in the full-power case and approximately forty percent in the half power case. The oscillation phase of the test lasts for approximately twenty hours. At the beginning of this phase, the PAO becomes instantaneously negative due

to the removal of the control rod with a maximum magnitude of approximately twenty and fifteen percent in the full-power and half-power cases, respectively. The PAO then increases to approximately ten percent for the full-power case and five percent for the half-power case. The last forty hours of the test was the return to equilibrium phase. The average PAO values over the last the forty hours of the test were approximately 8.0% ± 3.6% and 4.4% ± 2.5% for full-power and half-power cases, respectively.

The four phases of the test are further evident in the BOL xenon axial offset results as shown in Figure 26.

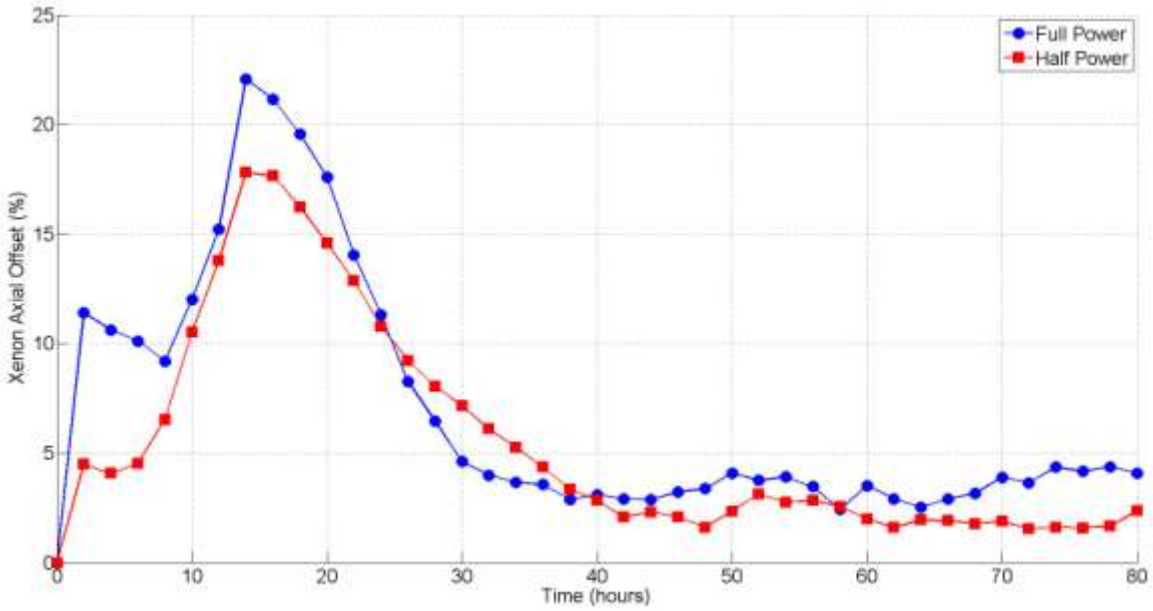

Figure 26: Xenon Axial Offset during BOL

The rod insertion phase results in a maximum XAO of approximately twenty-two percent in the full-power case and eighteen percent in the half-power case. The oscillation

phase is characterized by a decay trend as xenon concentrations quickly return to equilibrium concentrations based on the equilibrium power distribution between the top and bottom regions of the core. The average XAO values for the return to equilibrium phase of the test are 3.5% ± 0.6% and 2.1% ± 0.5% over the last forty hours of the test for the full-power and half-power cases, respectively.

It can be noted in Figure 26 that the full-power transient appears to enter the return to equilibrium phase ahead of the half-power transient. This result is due to increased negative temperature reactivity feedback at higher temperatures and also explains why xenon oscillation tests are typically conducted at reduced power levels.[67 68] This represents a more conservative case in addition to avoiding high heat load for fuel near the control rod used to initiate the transient as evident in the fuel centerline temperatures calculated in Figure 23 and Figure 24.

From these results, it is clear that the equilibrium PAO and XAO are not zero. This is due to the asymmetry in the temperature feedback introduced in the simulation of the fuel and coolant temperatures. As previously shown, the axial power and temperature distributions are "bottom-peaked" as a result of the increased moderation from the cooler coolant entering the core from the lower plenum. Thus, at equilibrium, the power and xenon distributions are bottom-peaked shown by a positive equilibrium PAO and XAO. The core model also shows increased stability at full power as evidenced by a speedy transition to the return to equilibrium phase shown by the steeper gradient of the XAO during the oscillation phase between twenty hours and 30 hours of the test. Nevertheless, the transient in the half-power test shows a smoother evolution due mainly to the lower thermal flux, reduced

equilibrium xenon concentration and worth. In both simulations, no oscillatory behavior is identified suggesting an inherently stable core design.

6.2.2 End of Core Life Results

The test procedure used in the methodology validation section was repeated with the developed core model at EOL. The oscillation was initiated by a control rod bank insertion into the top region of the core for six hours before removal. Simulations were executed for the first eighty hours of the test in two-hour intervals and the Power Axial Offset calculated. Two tests were performed with EOL fuel material definitions, one at full power (530 MW thermal) and the other at half power (265 MW thermal). The MCNPX simulations were executed using an MPI parallel installation of MCNPX 2.7 on a 32 core, 2.7 GHz, 64 GB RAM desktop workstation. The coupling was done using Portable Python 2.7.6.1.

However, due to limitations on computational resources (insufficient memory), the simulation terminated prematurely. This was due to the computational burden of MCNPX attempting to track 3400+ nuclides for 100+ individually defined materials. To remedy the situation, a reduced enrichment BOL fuel case was simulated as an analogue to the EOL fuel capturing the increased relative reactivity worth of xenon at EOL. All fission products were removed from the fuel material definition except Xe-135 and Sm-149; retaining the EOL concentrations for these two isotopes.

Figure 27 shows the effective neutron multiplication factor during the EOL tests at full and half power. At the beginning of the test, a sharp increase in effective neutron multiplication factor is seen. The xenon mass at the beginning of the test was calculated at a flux level commensurate with the reactivity worth of the fission products that have since been

removed. A number of these fission products are nuclides with substantial parasitic absorption of neutrons. Thus, a higher flux is required to maintain constant power with these nuclides included rather than removed and hence the initial xenon equilibrium mass is greater than the xenon equilibrium mass with the nuclides removed. This sharp decrease in xenon mass and the associated increase in neutron multiplication factor is an artificial effect introduced by having to remove nuclides to remedy the insufficient memory problem.

The effect of the removed nuclides is more obvious in the xenon mass results shown in Figure 28. Without the parasitic neutron absorption of the fission products that have been removed, the equilibrium level of xenon in the model is much lower than that prescribed in the material definitions at the beginning of the test. Thus, xenon is rapidly removed from the model but more so in the bottom region of the core (due to the "bottom-peaked" nature of the coolant density distribution) resulting in a "bottom-peaked" flux distribution. The net result is a temporary "top-peaked" xenon distribution and a corresponding negative XAO value.

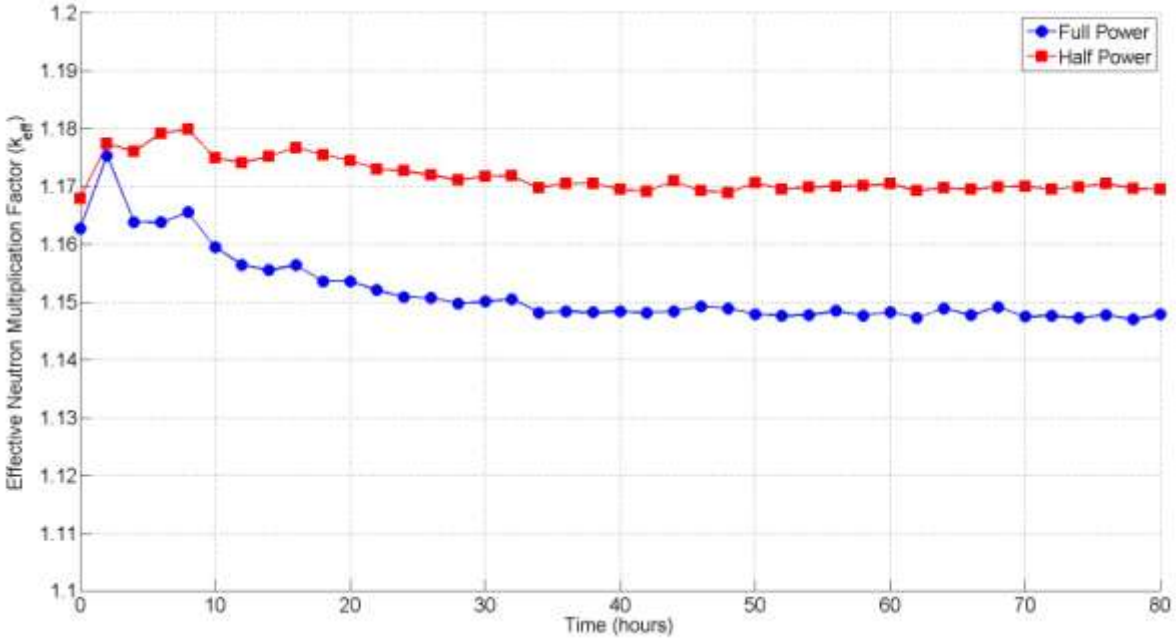

Figure 27: Effective Neutron Multiplication Factor during EOL Tests

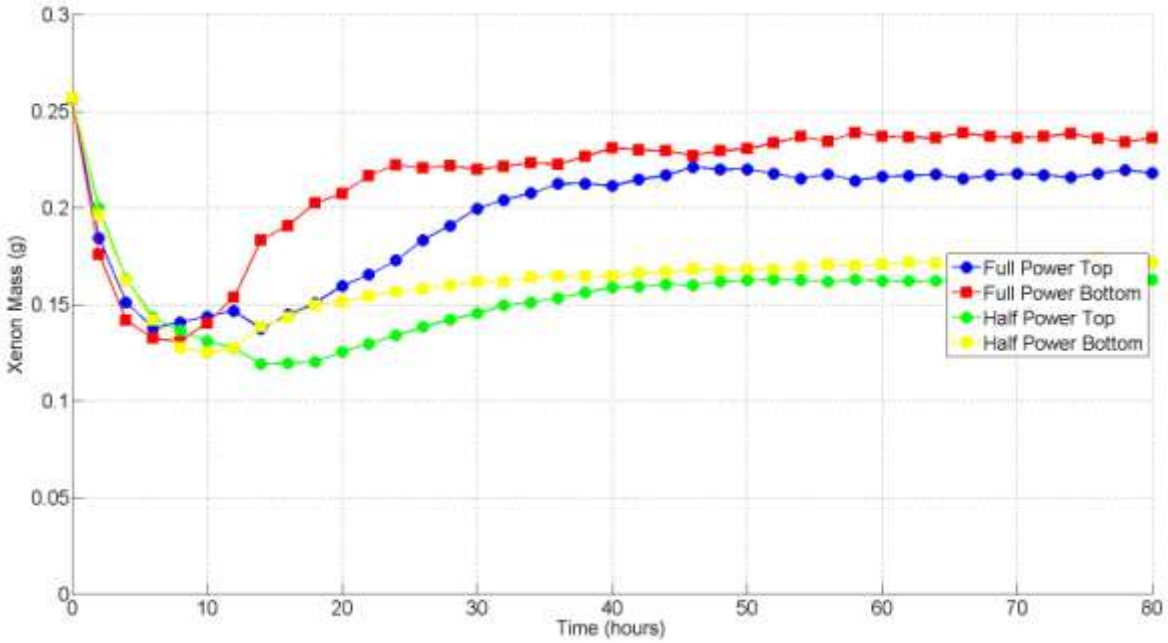

Figure 28: Xenon Mass during EOL Tests

The EOL PAO and XAO results from the simulations performed at full power and half power are presented in Figure 29 and Figure 30, respectively. Unlike the BOL case, the XAO parameter becomes immediately negative in the pre-test phase indicating a "top-peaked" equilibrium xenon distribution. The rod insertion phase results in a positive XAO value as again the xenon production in the bottom region of the core increases sharply as the xenon distribution becomes "bottom-peaked" in response to the rapidly changing flux. The ensuing oscillation phase is short-lived lasting no longer than approximately twenty-six and thirty hours into the test. The core model then enters the return to equilibrium phase until the end of the test at eighty hours. With EOL material definitions, the four main features of interest (pre-test, rod insertion, oscillation, and return to equilibrium) are identified in both the PAO and XAO parameters with similar behavior to the BOL results. Again it can be concluded that no oscillatory behavior is observed and the core model is stable with respect to xenon-induced power oscillations.

For completeness, the results for the power fractions are presented in Figure 31 and Figure 32, with corresponding average fuel centerline temperatures presented in Figure 33 and Figure 34 for EOL tests at full power and half power, respectively.

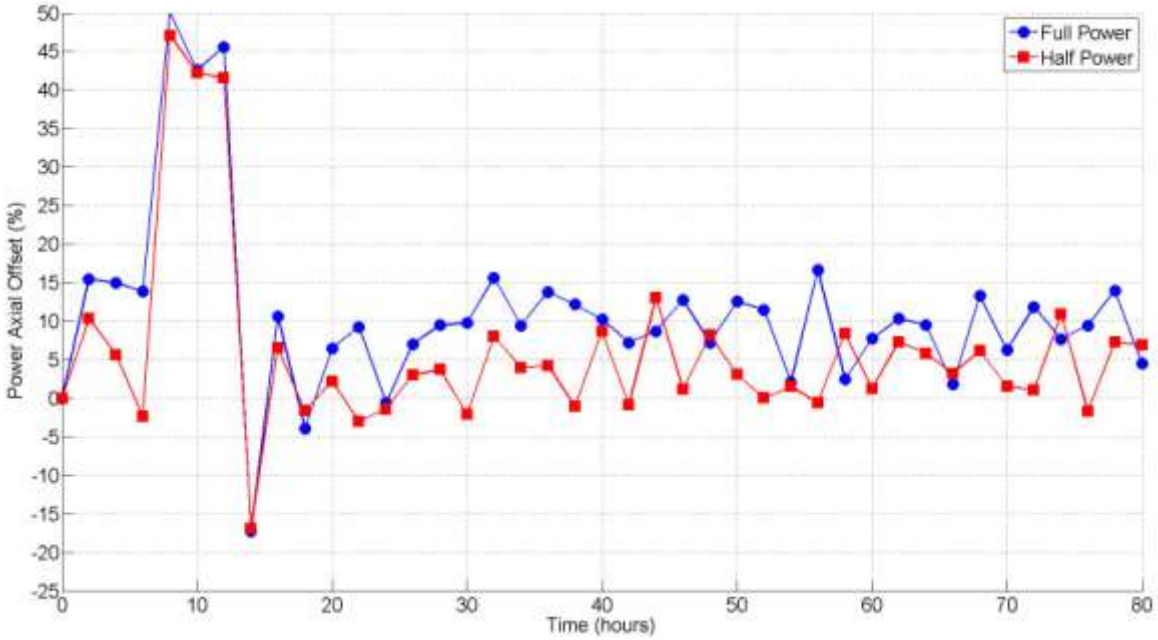

Figure 29: Power Axial Offset during EOL Tests

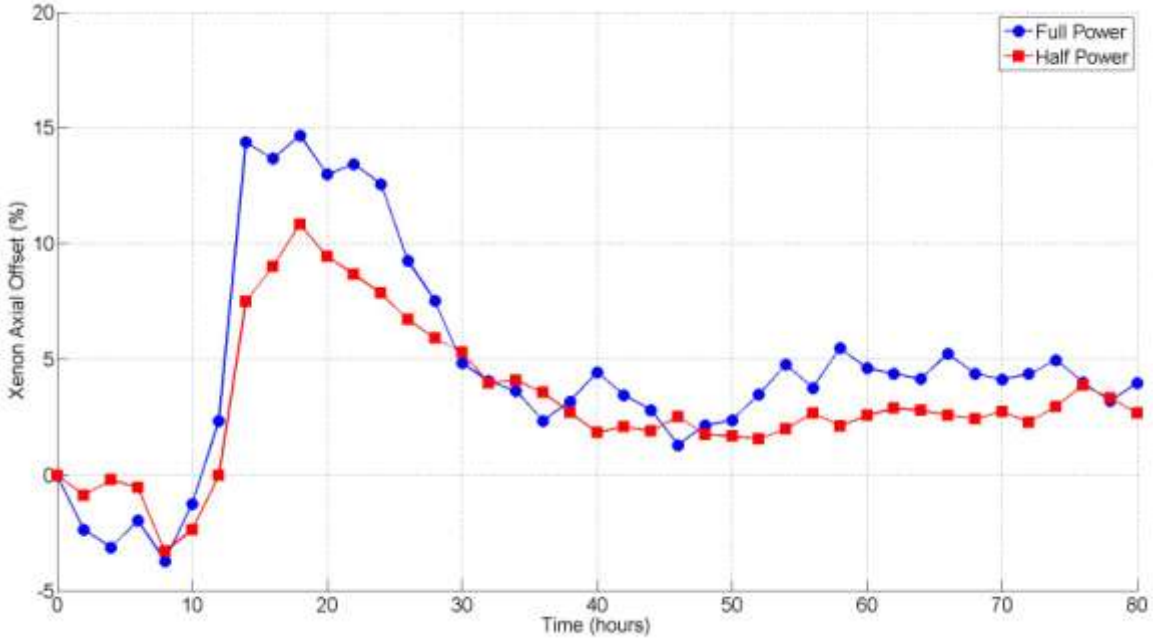

Figure 30: Xenon Axial Offset during EOL

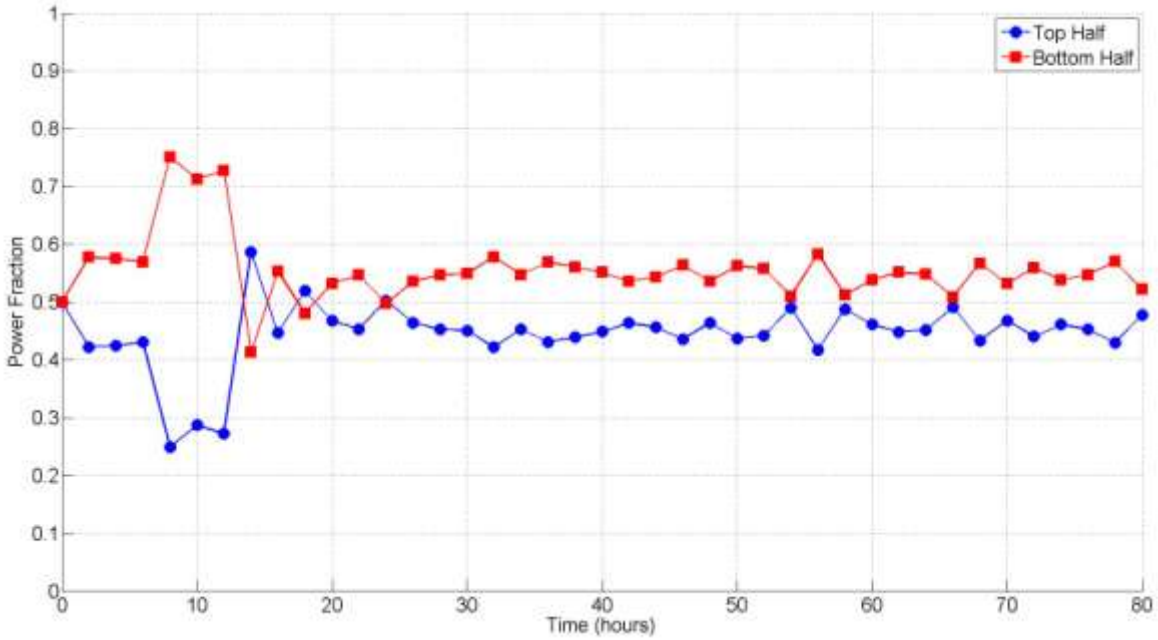

Figure 31: Power Fractions during EOL Tests at Full Power

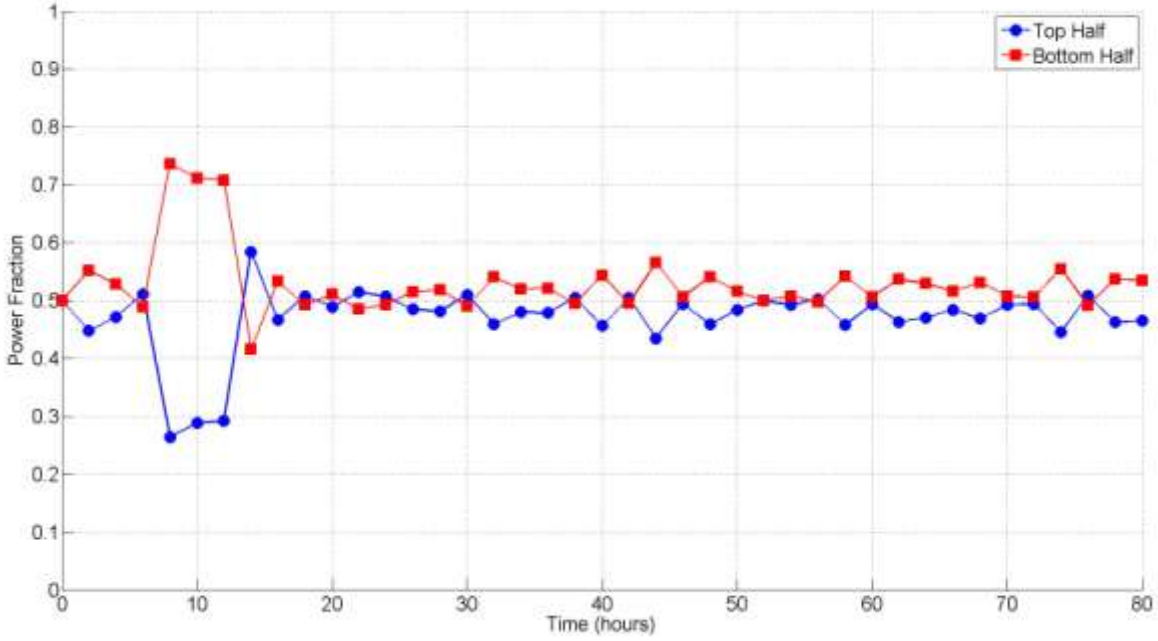

Figure 32: Power Fractions during EOL Tests at Half Power

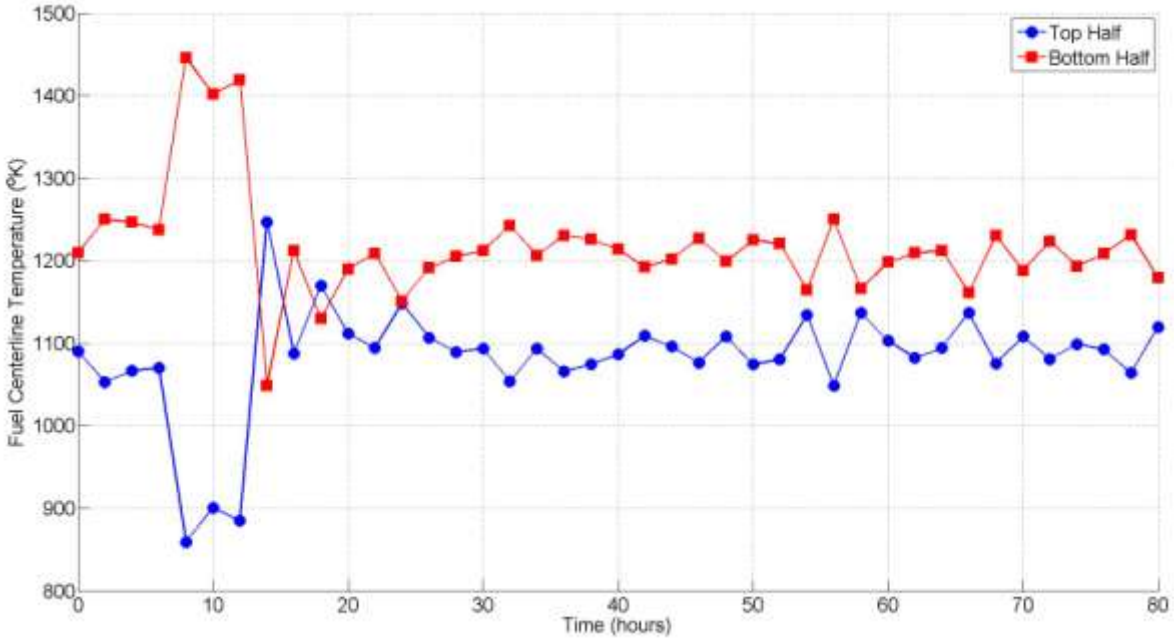

Figure 33: Average Fuel Centerline Temperatures during EOL Tests at Full Power

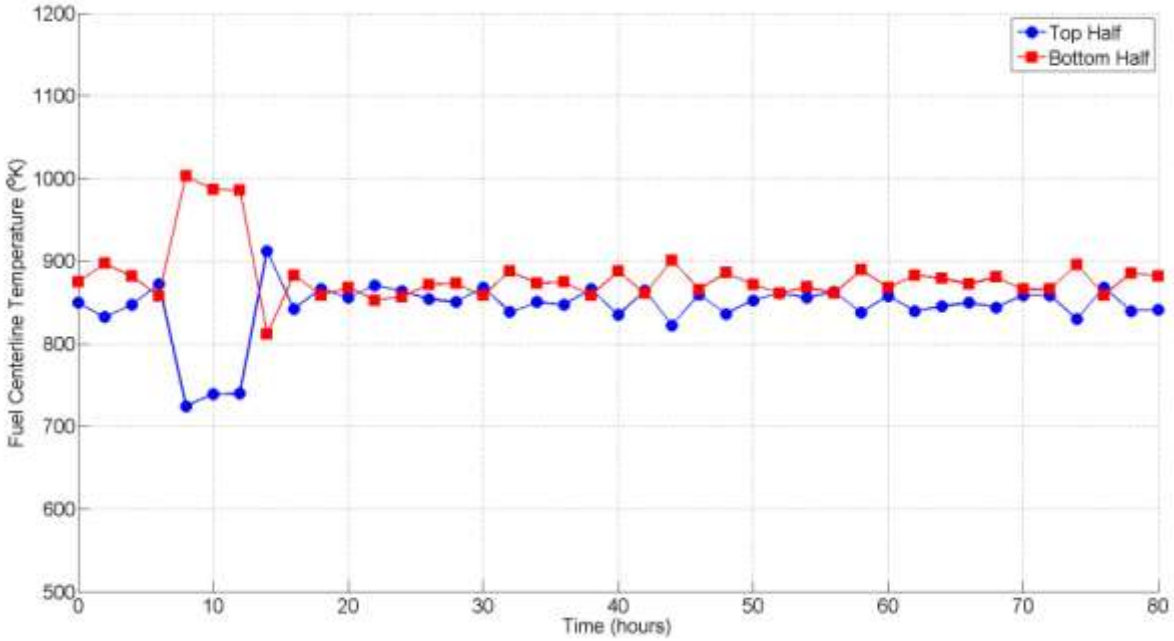

Figure 34: Average Fuel Centerline Temperatures during EOL Tests at Half power

6.3 Sensitivity Study - Axial Discretization

The temporal discretization scheme using two-hour time steps was chosen based on this time step size being significantly smaller than the oscillation period observed in literature. However, a suggested axial discretization was found in the literature reviewed. As mentioned in Section 2.4, the strong spatial dependence of the xenon-induced power oscillation phenomena requires high fidelity spatial information. In MCNPX simulations, this equates to adding cells to the problem geometry in which the neutron flux and reaction rates are tallied. Each cell requires its unique material definition to allow the tallies to be used to generate one-group cross sections to perform cell-dependent depletion. Thus, it is possible that the current level of spatial discretization (eight axial zones) may be insufficient to capture the xenon-induced power oscillation phenomena. Thus, a sensitivity study was performed using BOL material definitions to determine the requisite level of spatial discretization necessary to achieve statistically converged results. The same test was conducted, again at full power and half power using the developed methodology and core model with increased axial discretization; to twelve, sixteen and twenty-four regions.

The PAO results for BOL tests at full and half power are presented in Figure 35 and Figure 36, respectively. Likewise, the XAO results for BOL tests at full and half power are presented in Figure 37 and Figure 38, respectively. The standard deviation of the data from the different axially discretized models were calculated and are also shown on the figures. From the results, the model featuring twenty-four axial regions produced the same results for the PAO and XAO parameters as the eight-region case showing no benefit to the solution resolution by the additional axial discretization, substantiating the conclusion that the developed core model is inherently stable with respect to xenon-induced power oscillations.

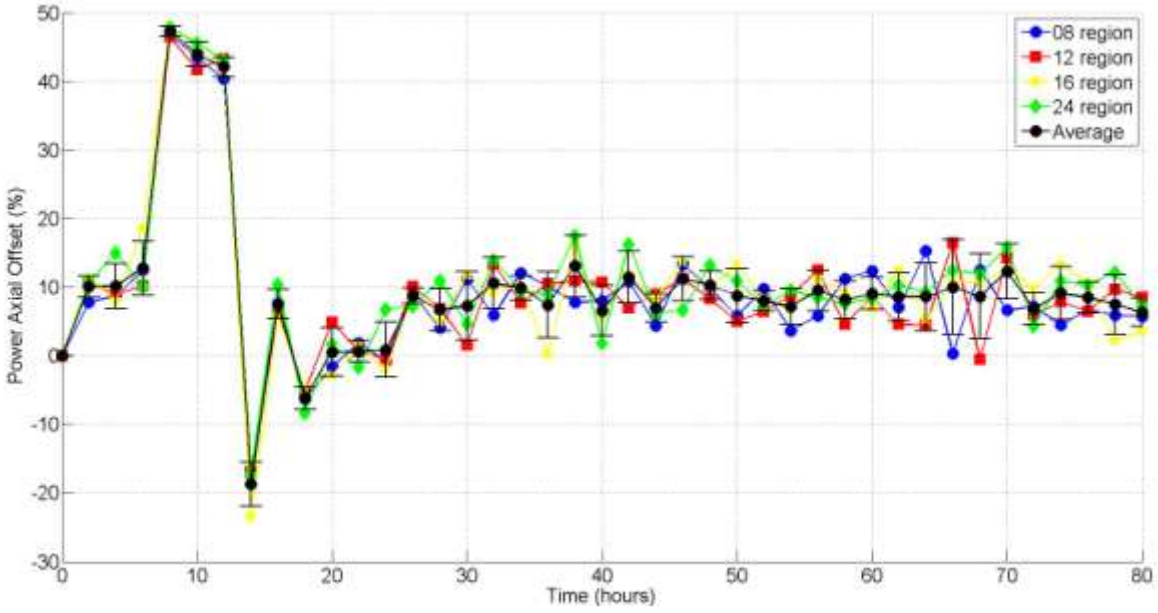

Figure 35: Discretization Sensitivity of the PAO during BOL Tests at Full Power

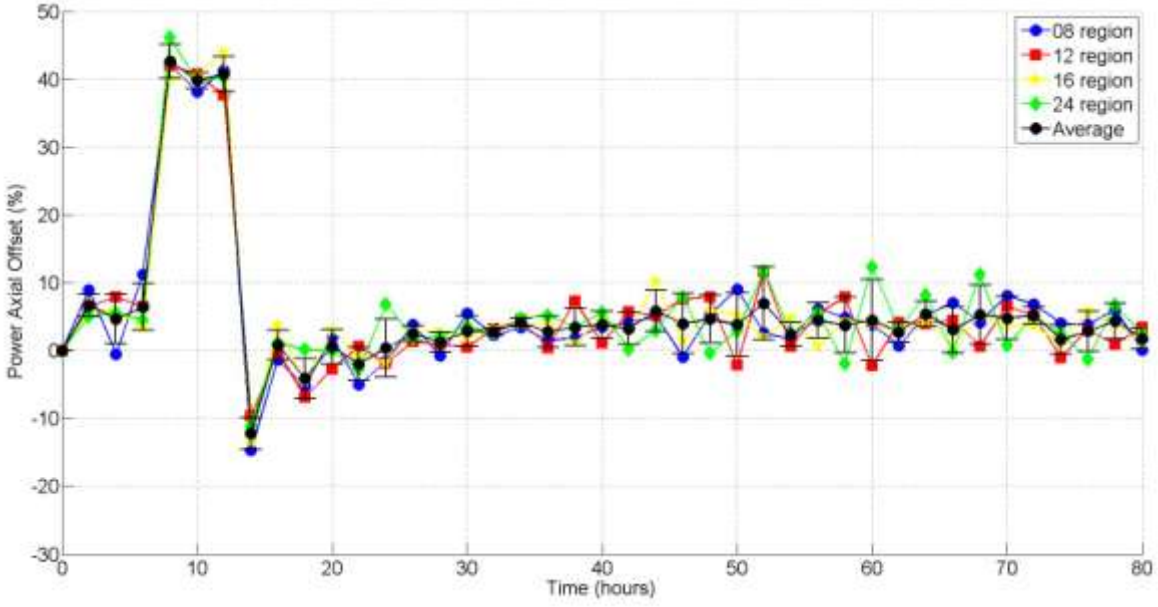

Figure 36: Discretization Sensitivity of the PAO during BOL Tests at Half Power

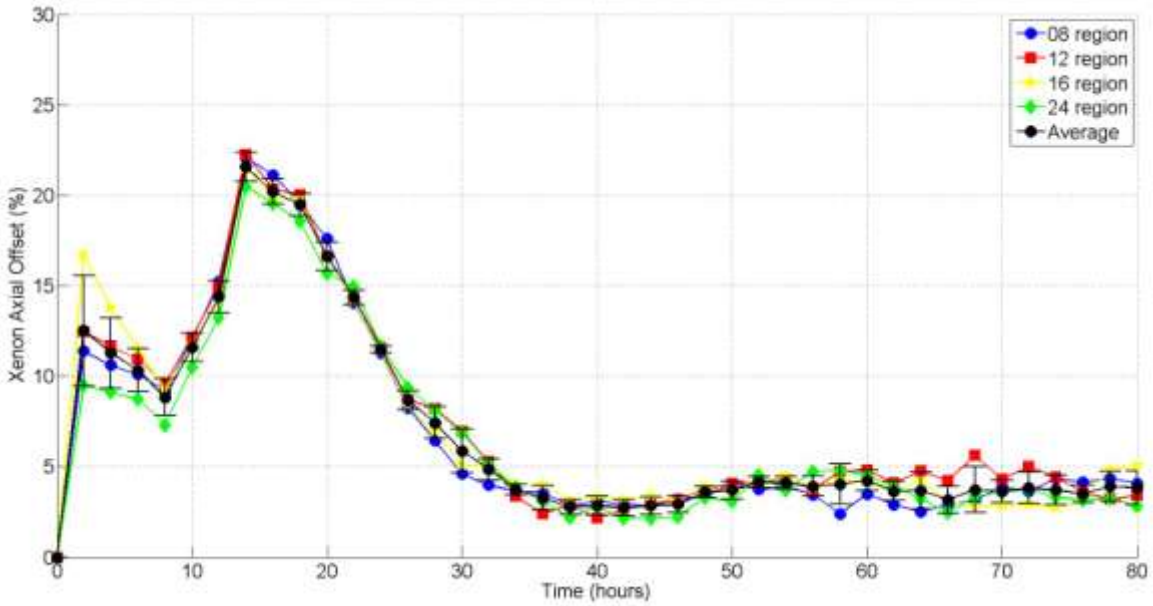

Figure 37: Discretization Sensitivity of the XAO during BOL Tests at Full Power

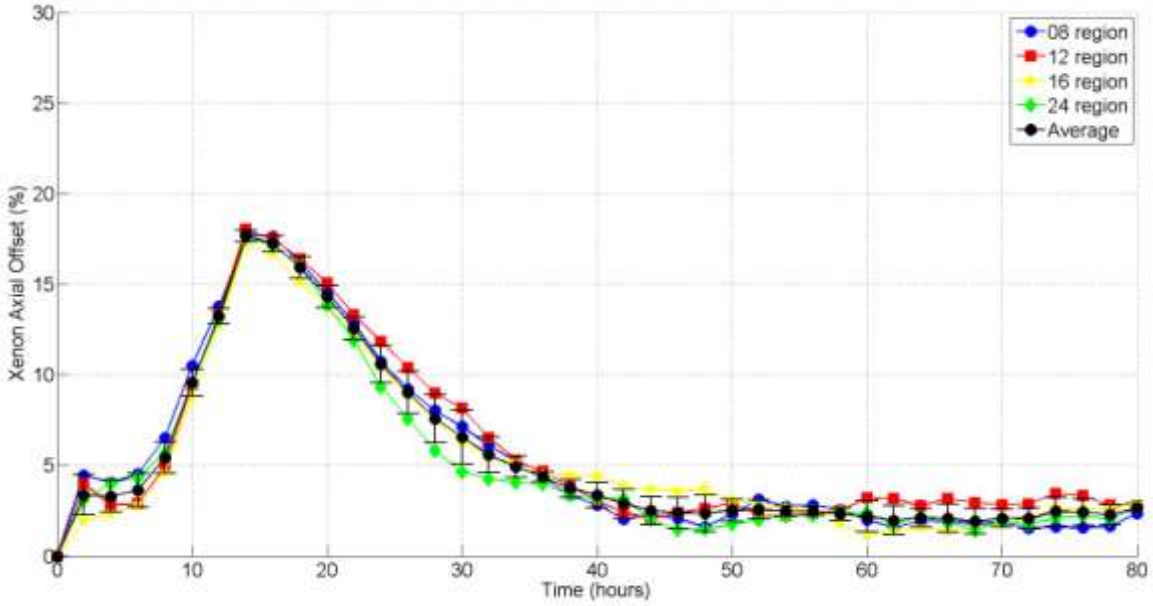

Figure 38: Discretization Sensitivity of the XAO during EOL Tests at Half Power

The PAO and XAO results for EOL tests at full and half power are presented in Figure 39. The standard deviation of the data from the different axially discretized models were calculated and also shown on the figures. Due to memory limitations, the simulations of the EOL model featuring twenty-four axial regions although initiated, could not be completed, even at reduced fidelity.

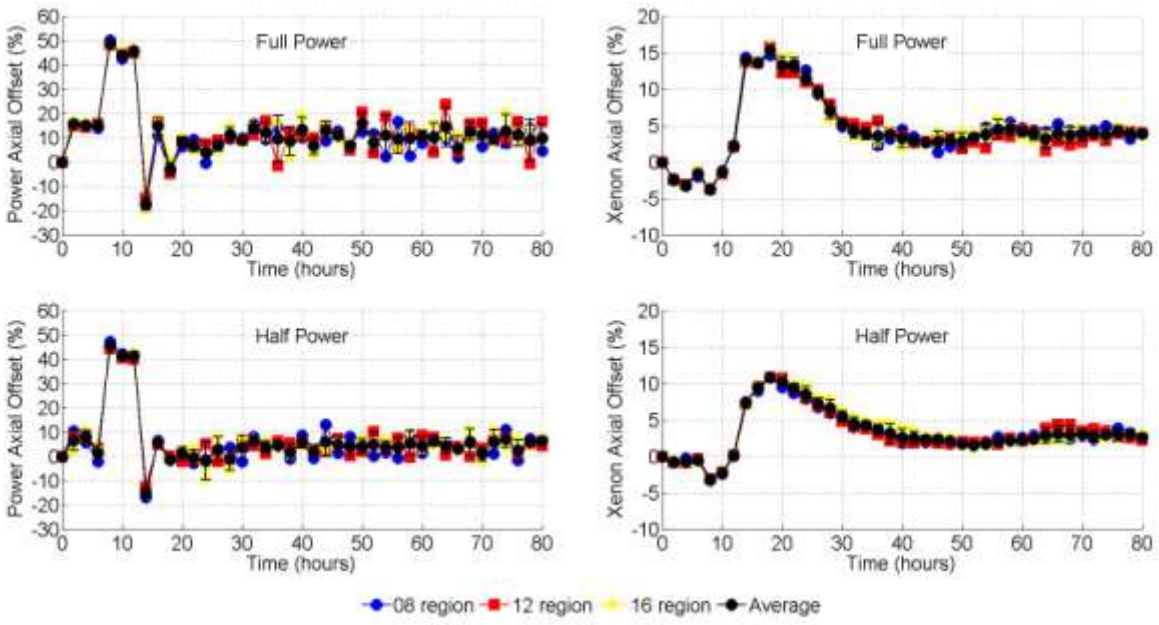

Figure 39: Discretization Sensitivity of the PAO and XAO during EOL Tests

As with the BOL results, the results for the models with twelve and sixteen axial regions fall within the error of the eight-region model as determined from the quantification of the stochastic uncertainty during EOL tests at full and half power. With no additional utility from the increased fidelity models, the conclusion that the developed SMR core model is inherently stable with respect to xenon-induced power oscillations at end of core life is confirmed and maintained.

6.4 Sensitivity Study - Quantification of Stochastic Noise

As identified in Section 4.1, the stochastic nature of the Monte Carlo method results in asymmetric solutions to known symmetric computations that are "symmetric within error". For the purposes of assessing xenon-induced power oscillations, it is possible that these asymmetries may be propagated from depletion step to depletion step resulting in an oscillatory behavior which is unreal. Though no oscillatory nature has been observed thus far, it is necessary to definitively eliminate the inherent stochastic nature of the Monte Carlo method as the cause of any oscillations observed in future models where the developed methodology may be applied.

To this end, the stochastic noise introduced into the results due to the Monte Carlo method was quantified by performing multiple simulations using the developed methodology with different random seed numbers for the MCNPX simulations. By averaging the results of several different random simulations, the stochastic noise in any single simulation was removed and a "noise-free" solution produced. Seven random seed simulations were executed using the core model and the developed methodology which, in addition to the results presented previously make a total of eight data points at each time step. The random seed number was changed using the DBCN card in MCNPX. The results for the power axial offset and xenon axial offset parameters are presented in Figure 40 and Figure 41, respectively. The average and standard deviation of the PAO and XAO at each step is calculated and presented on the same figures. The maximum and average standard deviations in the PAO and XAO parameters were 5.2% and 2.0%, respectively.

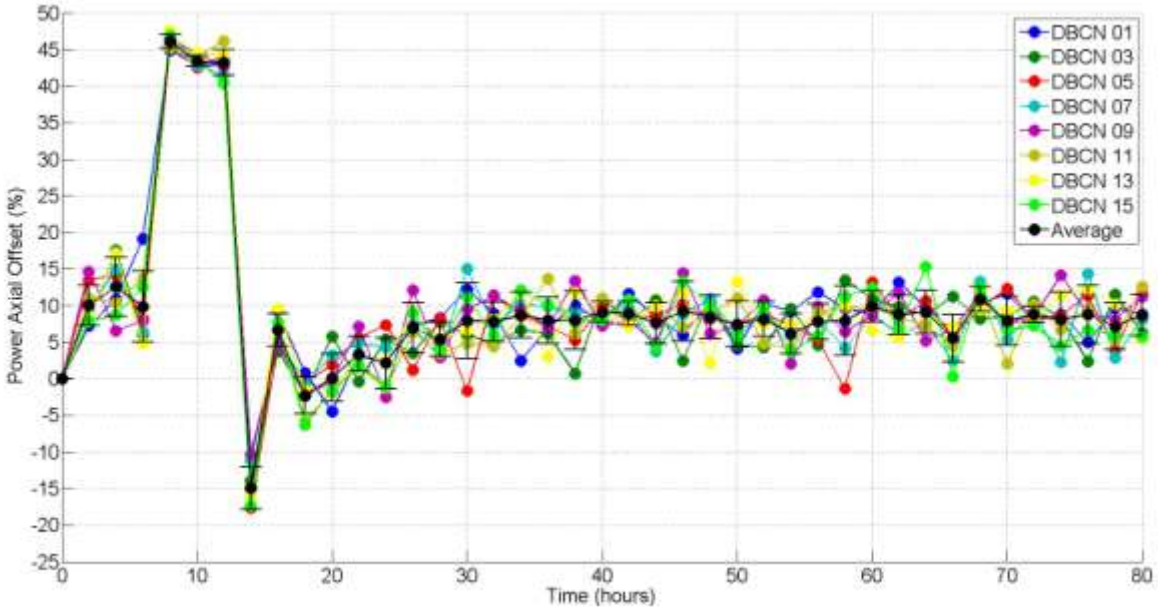

Figure 40: Stochastic Error in Power Axial Offset during BOL Tests at Full Power

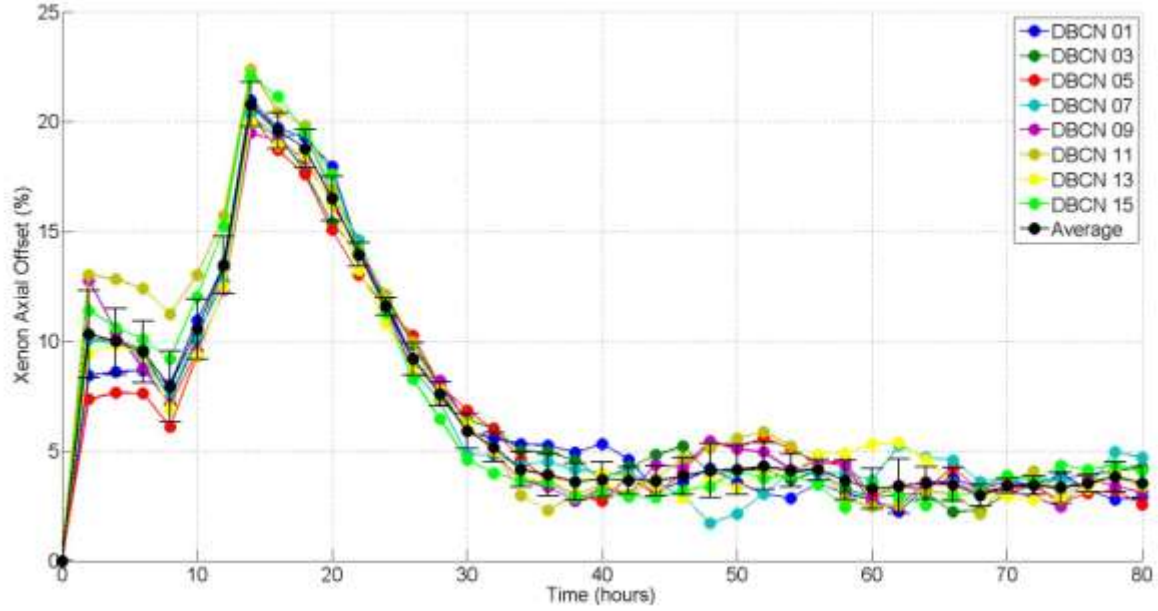

Figure 41: Stochastic Error in Xenon Axial Offset during BOL Tests at Full Power

For conservatism, this level of stochastic noise was assumed to be the level of stochastic uncertainty in for both parameters. Under this assumption, considering the introduced PAO and XAO values of approximately 45% and 22%, respectively. It can be concluded that the developed core model is inherently stable at BOL (and EOL from previous results) with respect to xenon-induced power oscillations showing no variation above the stochastic level. These results further strengthen the conclusion that the eight-region axial spatial discretization scheme employed was indeed sufficient.

6.5 Assessment of Error in Reaction Rate Convergence

As discussed in Section 3.2.1, the Monte Carlo method has very high computational costs when compared to deterministic methods for radiation transport problems due to the requisite simulation of a large number of particles to approximate a solution to the problem of interest. In order to arrive at a converged solution, cell neutron fluxes and reaction rates must be accurately computed. These fluxes and reaction rates are used to calculate cell power fractions and generate collapsed one-group cross sections for use in the fuel depletion calculations which determine the nuclide number densities for each time step. The uncertainties in the neutron cell fluxes and reaction rates are a function of the number of particles entering the cell in the Monte Carlo simulation. The more reactive cells (typically at the center of the problem geometry) have a larger number of particles sampled and hence a smaller error in flux and reaction rates. The less reactive cells (typically at the extremities of the problem geometry) have a lower sampling rate and hence a larger error.

As a result, the Monte Carlo method is excellent for calculating global parameters (such as effective multiplication factor, total xenon mass) since every simulated particle

contributes to the convergence of the quantity of interest. However, localized parameters (such as spatial xenon distribution) require significantly more particles to be simulated for convergence. With respect to this research, it was important to accurately predict the mass of xenon produced in each fuel cell in order to capture changes in the xenon distribution which may initiate power oscillations. The xenon mass is localized parameter and as such the error in the xenon mass calculations must be assessed in addition to the error from propagated stochastic asymmetries in the core model, by looking at the convergence of the flux and reaction rate tallies. Table 5 shows the average percent relative error in reaction rates of interest as determined by the xenon decay scheme shown in Figure 2 for the four different axially discretized models at two hours into the test. The relative error in the uranium-235 fission reaction was used as the error for the power and the xenon-135 capture reaction rate was used as the error for the xenon mass. These errors were used in to calculate the propagated error in the PAO and XAO, respectively. The results are presented Table 6.

$$P_{bot} = \sum_{i=1}^{\#bot} P_i \qquad P_{top} = \sum_{i=1}^{\#top} P_i$$

$$Xe_{bot} = \sum_{i=1}^{\#bot} Xe_i \qquad Xe_{top} = \sum_{i=1}^{\#top} Xe_i$$

$$\partial P_{bot} = \sqrt{\sum_{i=1}^{\#bot} (\delta P_i)^2} \qquad \partial P_{top} = \sqrt{\sum_{i=1}^{\#top} (\delta Xe_i)^2},$$

$$\partial Xe_{bot} = \sqrt{\sum_{i=1}^{\#bot} (\delta Xe_i)^2} \qquad \partial Xe_{top} = \sqrt{\sum_{i=1}^{\#top} (\delta Xe_i)^2}$$

$$\partial \mathrm{PAO} = |\mathrm{PAO}| \times \sqrt{\left(\frac{\delta\left(\mathrm{P_{bot}} - \mathrm{P_{top}}\right)}{\left(\mathrm{P_{bot}} - \mathrm{P_{top}}\right)}\right)^2 + \left(\frac{\delta\left(\mathrm{P_{bot}} + \mathrm{P_{top}}\right)}{\left(\mathrm{P_{bot}} + \mathrm{P_{top}}\right)}\right)^2}$$

$$\partial \mathrm{XAO} = |\mathrm{XAO}| \times \sqrt{\left(\frac{\delta\left(\mathrm{Xe_{bot}} - \mathrm{Xe_{top}}\right)}{\left(\mathrm{Xe_{bot}} - \mathrm{Xe_{top}}\right)}\right)^2 + \left(\frac{\delta\left(\mathrm{Xe_{bot}} + \mathrm{Xe_{top}}\right)}{\left(\mathrm{Xe_{bot}} + \mathrm{Xe_{top}}\right)}\right)^2}$$

Table 5: Relative Error in Important Reaction Rates as a function of Axial Discretization

Axial Regions	**8**	**12**	**16**	**24**
Fuel segments in the core	104	156	204	312
Average Relative Percent Error in U-235 fission reaction rate	1.13	1.38	1.58	1.87
Average Relative Percent Error in Xe-135 radiative capture reaction rate	1.37	1.67	1.92	2.29

Table 6: Relative Error in PAO and XAO as a function of Axial Discretization

Axial Regions	**8**	**12**	**16**	**24**
Fuel segments	104	156	208	312
Estimated Percent Error in PAO (%∂PAO)	1.63	1.32	1.19	1.18
Estimated Percent Error in XAO (%∂PAO)	1.35	1.33	0.98	1.60

The average relative error in the uranium-235 fission reaction rate increases with axial discretization. This result was expected and can be attributed to fact that increasing the axial discretization by adding cells to the problem geometry decreases the number of particles per cell resulting in less converged estimates for flux and reaction rates per cell. However, the relative error in the PAO parameter decreases with axial discretization. This result is due to the improved spatial resolution of the flux and reaction rates as axial discretization is improved. The cells near the center of the core produce a larger proportion of the total power having a larger population of neutrons and hence a smaller than average relative error. The number of cells near the extremities of the core is increased, each with larger than average relative errors which drive up the average relative error. However these additional cells produce significantly less power and as such their relatively large errors contribute significantly less to the calculation of the total relative error in the PAO parameter.

6.6 Burnable Absorber Analysis

The preceding analyses of the developed SMR core model reveal an SMR design with very similar characteristics to existing large commercial PWRs. Thus, with respect to compensating for excess reactivity, shaping the flux and power profile within the core, and active reactor control, an approach similar to that employed in existing large PWRs can be adopted. An assessment of the choices of burnable absorber material and configuration is performed to provide initial insight to the differences, if any, between PWR and SMR reactivity control in the absence of soluble boron in the coolant.

6.6.1 Methods for Excess Reactivity Control

Currently, there are three main methods employed in PWRs to achieve excess reactivity control. The first method involves the insertion of strong neutron absorbing material into the reactor core in the shape of control rods. The strong neutron absorbing material in the control rods, effectively reduced the number of neutrons available to propagate the fission reaction. The amount of control exerted by the control rods is a function of insertion distance into the core. The insertion distance is controlled by the reactor operator and gives an active mechanism for controlling core power.

The second method is to mix the strong neutron absorbing materials into the fuel material itself. In this configuration, the amount of absorber introduced to the core must be determined at the beginning of core life and is fixed once the core has been loaded. As the strong absorbing material captures neutrons, it will be depleted over time. As such these burnable absorbers are used primarily to suppress the initial excess reactivity in the core at beginning of core life.

The third method is to introduce the strong absorbing material in a soluble form dissolved into the coolant. PWRs are thermal reactors meaning that a majority of the fissions within the chain reaction are caused by neutrons with thermal energies. However, all neutrons produced in fission initially have fast energies and, as such, need to be slowed down (or thermalized) in order to continue the fission chain reaction. The fast neutrons produced in the fuel are thermalized in the coolant which also serves as a moderator. By adding strong absorbing material to the coolant, a fraction of the thermalized neutrons can be removed before returning to the fuel to cause fission thus controlling the fission chain reaction. This method allows for active control of core power since the concentration of strong absorbing

material in the coolant can be controlled by a Chemical Volume Control System which can add or remove the absorber material as needed.[69]

6.6.2 Implications of a Boron Free Coolant in SMR Operations

For PWRs, the soluble absorber material of choice is typically soluble boron in the form of boric acid. A major advantage of using soluble boron is that unlike control rods and burnable absorbers which provide localized reactivity control, soluble boron can provide a more global reactivity control as the absorber material is effectively distributed throughout the core by the coolant. Nevertheless, eliminating the use of the soluble absorber material offers several advantages to SMR operation. These include the removal of all systems associated with the manipulation of the boron concentration in the coolant (pipes, pumps, and purification systems) and the elimination of the corrosive effects of boric acid within the coolant. In doing so, a class of accident scenarios is eliminated which are initiated by the movement of a volume of coolant that is void of boron or rich in boron through the core. This coolant volume can result in very localized, strong, positive or negative reactivity insertions resulting in transients which could lead to reactor shutdown.

6.6.3 Burnable Absorber Comparison

Eliminating soluble boron as a means of excess reactivity control places an increased burden on control rod manipulation and initial burnable absorber loadings. To understand the appropriateness of PWR-style burnable absorbers in the developed SMR model, a study was performed in which various burnable absorber materials and configurations were tested in the SMR fuel assembly and the effect on the infinite multiplication factor (k_∞) observed. The

configurations and materials were selected based on Westinghouse burnable absorber rod design.[88] The combinations of different configurations and materials included in the investigation are presented in Table 7. The burnable absorber rod (BAR) and wetted annulus burnable absorber rod (WABA) configurations are selected for investigation. Figure 42 shows a radial cross section of a BAR cell.

Table 7: Materials and Configurations Considered in Burnable Absorber Analysis

Type	BAR	WABA	Gd_2O_3	Er_2O_3
Neutron Absorber	^{10}B AgInCd	^{10}B AgInCd	^{155}Gd , ^{157}Gd	^{167}Er
Absorber Material	B_4C AgInCd	B_4C AgInCd	Gd_2O_3/UO_2	Er_2O_3/UO_2
Assembly Location	Guide tube	Guide tube	Mixed with fuel pellet	Mixed with fuel pellet

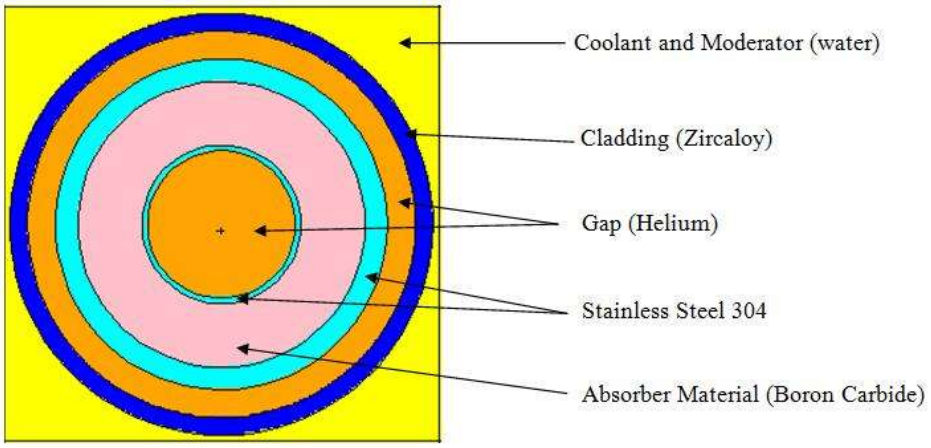

Figure 42: Radial Cross Section of a Burnable Absorber Rod

The WABA configuration is similar to the BAR configuration except that the central helium gap in the BAR configuration is vacated, allowing water to fill the annulus of the rod. The BAR and WABA configurations are limited to the twenty-four guide tube locations within the fuel assembly. Simulations were performed for four, eight, twelve and twenty-four rods in the assembly and compared to a no rods case. The typical absorber material for the BAR configuration was boron carbide (B_4C) or borosilicate glass. Silver-indium-cadmium (AgInCd) was typically used as a control rod material but was included in the analysis for comparison. For simplicity a uniform loading enrichment of burnable absorber was assumed in all the simulations. Axial grading of the burnable absorber (varying absorber enrichment along the length of the rod to account for the "bottom-peaked" nature of the flux) was not investigated. Figure 43 shows the effect on the infinite multiplication factor of the different discrete burnable materials in BAR and WABA configurations.

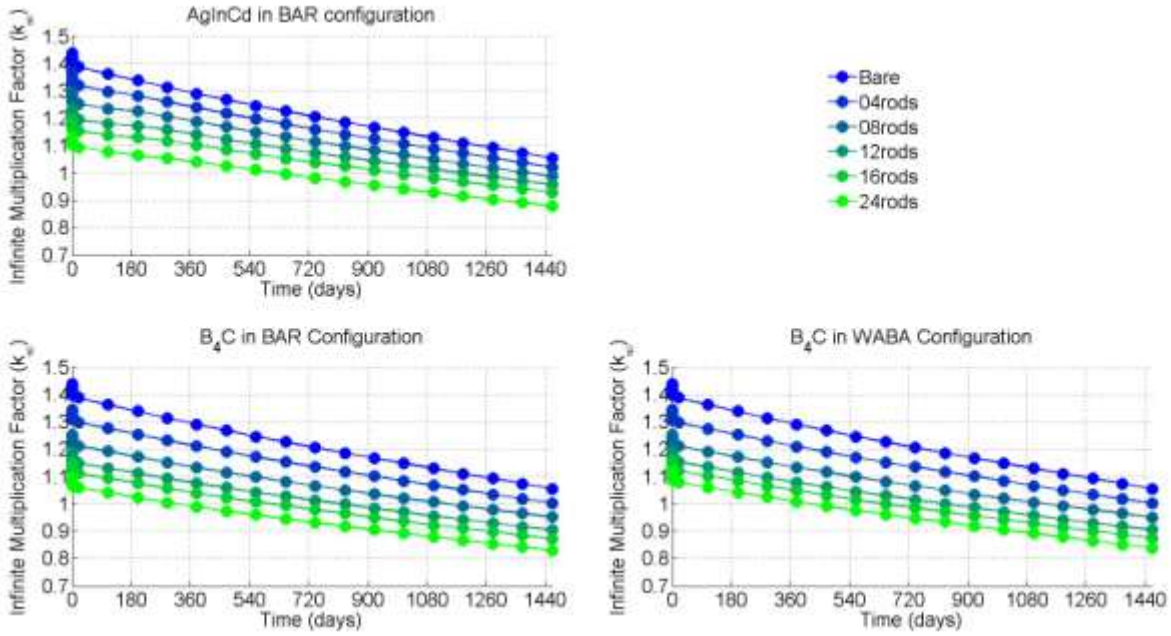

Figure 43: Infinite Neutron Multiplication Factor for Various Burnable Absorber Rods

Figure 44 shows the results for the twelve and twenty-four rod cases for both B4C and AgInCd in comparison to the no rods case. Two notable differences in the infinite neutron multiplication factor were immediately identified. The first was a reduction in the excess reactivity at the beginning of core life. This effect was due to parasitic absorption of neutrons by the introduced absorber material negatively affecting the fission chain reaction by reducing the number of readily available neutrons for fission. This reduced excess reactivity at beginning of core life is highly desirable and is the main reason why burnable absorbers are employed. The second, less desirable effect is evident at end of core life in a reduced infinite neutron multiplication factor. This reduced end of core life reactivity was due to the incomplete depletion of the introduced absorber material at end of core life. The absorber continued to suppress reactivity in the core. This effect is known as the residual absorption penalty.

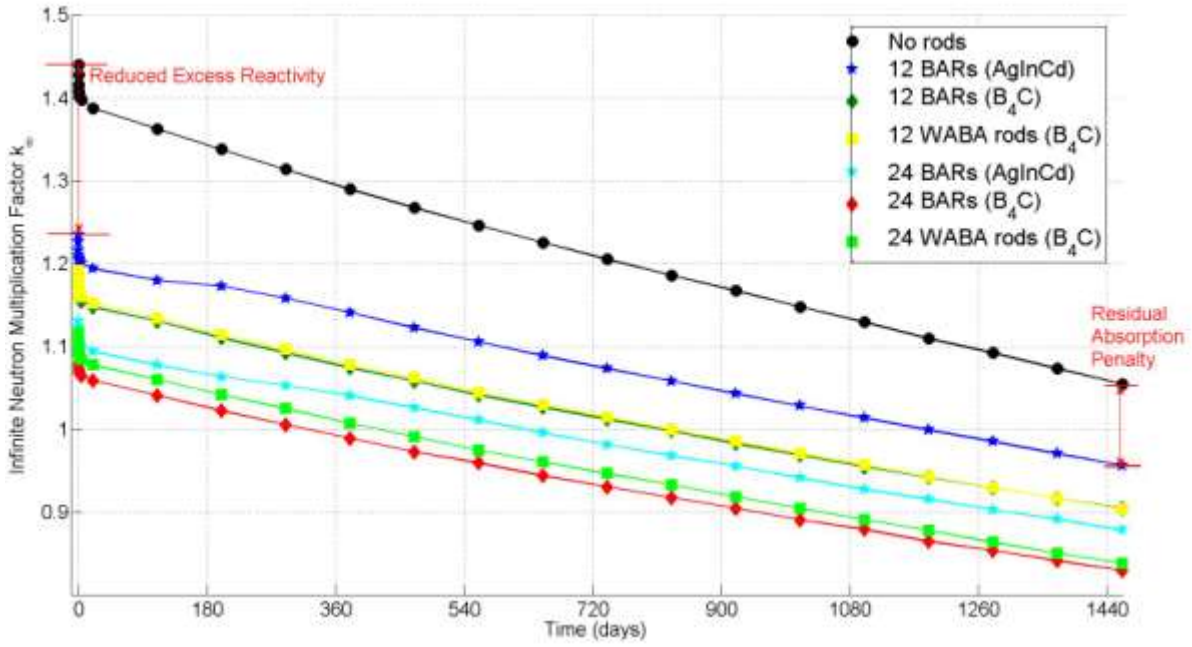

Figure 44: Discrete Burnable Absorber Rod Comparison

The reduced excess reactivity at beginning of life and the residual absorption penalty at end of life are both proportional to the number of burnable absorber rods introduced at the beginning of core life. For equal volumes, the B_4C (at natural enrichment; 19.9% ^{10}B) produces the largest reduced excess reactivity at BOL but also the greatest residual absorption penalty at EOL. The AgInCd burnable absorber rod has the smallest reduced excess reactivity at BOL and similarly smallest residual absorption penalty at EOL. The additional moderation of neutrons offered by the water annulus in the WABA rod results in slightly improved depletion of the loaded ^{10}B content accompanied by a marginally improved residual absorption penalty at EOL.

Gadolinium oxide (Gd_2O_3) and erbium oxide (and Er_2O_3) were considered for direct mixing with the fuel material. The material was homogeneously mixed with the uranium dioxide at fuel fabrication. Figure 45 shows a radial cross section of a mixed burnable absorber – fuel rod.

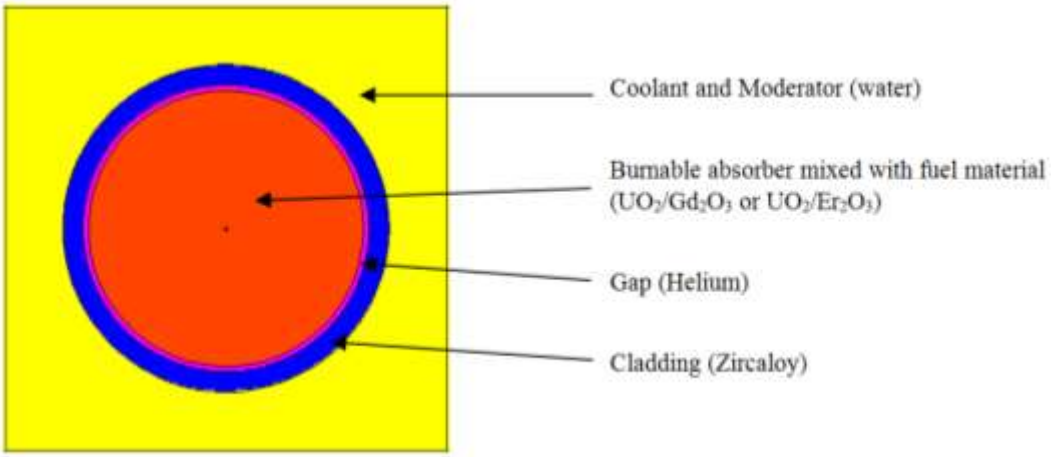

Figure 45: Radial Cross Section of a Mixed Burnable Absorber Rod

Unlike the BAR and WABA rods, these rods are not limited to the guide tube locations and may occupy any of the 264 fuel rod locations within the assembly. The number of directly mixed burnable absorber rods is varied between four and eighty rods with the only restriction a requirement to maintain assembly symmetry. Adding the burnable material directly to the fuel mixture has the result of decreasing the thermal conductivity of the fuel rod. To compensate for this reduced thermal conductivity, the fuel enrichment is reduced by ten percent of the original enrichment. This is done to ensure that the hottest fuel pin does not occur in a fuel pin of reduced thermal conductivity. In addition, the enrichment of the burnable absorber material was varied between two and eight weight percent. The simulation results for gadolinium oxide at two, four, six and eight weight percent are compared to the no rods case and presented in Figure 46. Similarly, the results for erbium oxide at two, four, six and eight weight percent are compared to the no rods case and presented in Figure 47.

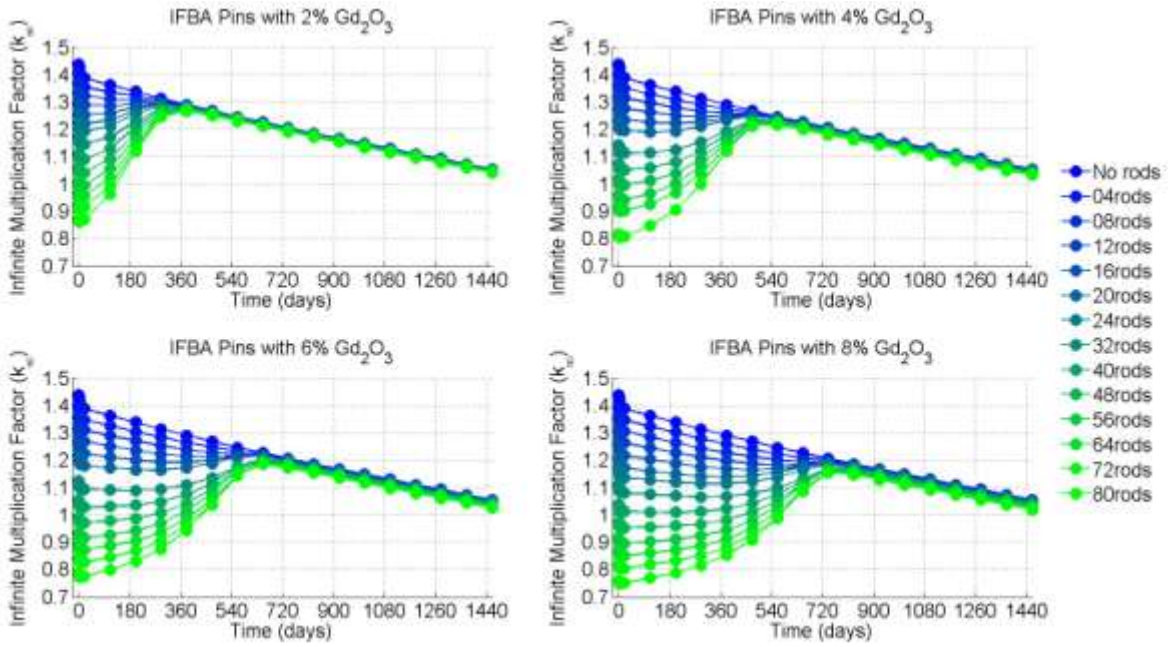

Figure 46: Infinite Multiplication Factor with Various Gd_2O_3 Enrichments

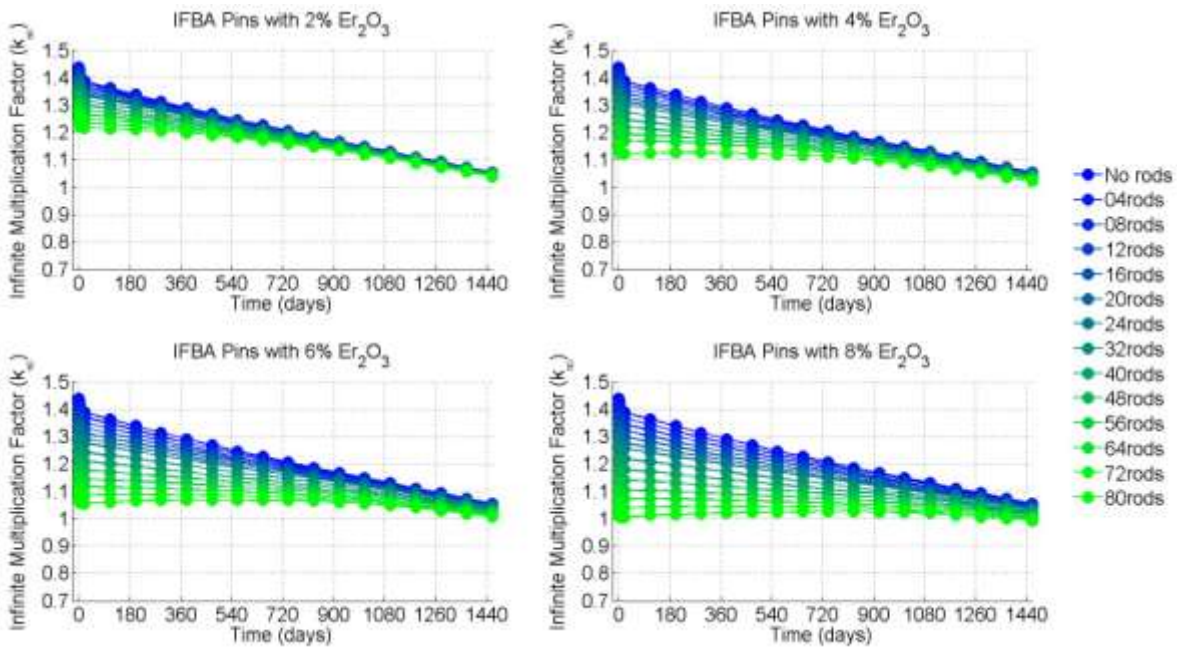

Figure 47: Infinite Multiplication Factor with Various Er_2O_3 Enrichments

Figure 46 and Figure 47 show clearly that gadolinium oxide offers the greatest reactivity suppression potential at BOL. This is evidenced by the lower infinite neutron multiplication factors while maintaining a negligible residual absorption penalty at EOL when compared to the no rods case. As more rods are added to the assembly, the excess reactivity at BOL is further suppressed with no additional residual absorption penalty at EOL.

Rod self-shielding effects are more evident in the cases with higher absorber material enrichment. Self-shielding occurs when the absorber material in the surface layers of the rod absorb a significant fraction of the neutron flux effectively shielding the inner layers. This leads to a slower release of excess reactivity seen in the cases with higher enrichment and increased number of rods. In each enrichment case the total absorber loading is essentially

depleted at the same point. The results reveal the fact that gadolinium has the same effect of a strong local absorber.

Although erbium oxide has a lower reactivity suppression potential at BOL and a slightly larger residual absorption penalty when compared to gadolinium oxide, as additional rods are employed and absorber enrichment increased the reactivity suppression potential of erbium oxide increases significantly with minimal increase in the residual absorption penalty. No self-shielding effects are visible in the erbium oxide results revealing that erbium has the same effect as a dispersed absorber in that all regions of the absorber material are depleted at the same rate.

In terms of application of gadolinium oxide and erbium oxide in SMRs as potential burnable absorbers, the key difference between the two is found in the respective reactivity swings over the core lifetime. The reactivity swing is defined as the difference in excess reactivity at BOL and EOL; the gadolinium oxide cases are quite large when compared to the erbium oxide cases.

With erbium oxide displaying dispersed absorber characteristics, it is a viable option to “replace” soluble boron in the coolant to provide global excess reactivity control while reducing the control burden on the control rods. Gadolinium oxide deployment would follow existing PWR strategies aimed at minimizing peaking taking advantage of its strong local absorption characteristic.

6.6.4 Control Rod Positioning, Power Profiles and Optimized Core Loading

Control rod position for the iPWR SMR was determined by placing control rods in areas of localized power peaking. The locations of power peaking were determined by

computing the assembly-wise power at BOL is shown in Figure 48. The assembly-wise power calculations were repeated for core life-times of 360 days, 720 days, 1080 days and EOL to determine the localized power peaking. Using these power maps, control rod locations are chosen to maximize the effect of each rod while minimizing the number of rods required to shut down the reactor.

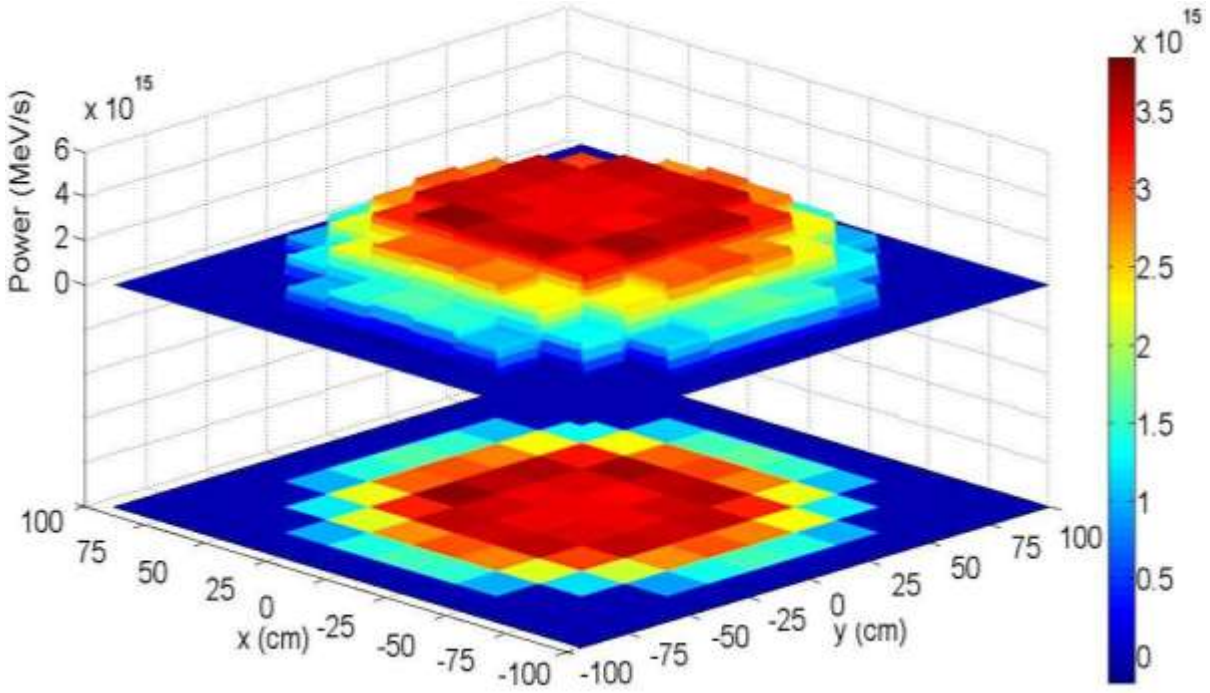

Figure 48: Assembly Power Distribution at BOL

Using a combination of boron carbide burnable absorber rods and gadolinium oxide mixed fuel rods, a core loading pattern that meets the specified performance requirements, such as the burn-up, core life-time, core power uniformity, is obtained and shown in Figure 49. The number in the upper left corner of the cell is the number of burnable absorber rods in that location while the number in the lower right corner represents the number of control rods

in that location. This core loading was chosen to achieve the most uniform power distribution possible over the core lifetime as this maximizes the fuel utilization while minimizing power peaking. Figure 50 shows the power distribution for the SMR core without optimization of burnable absorber loading. Figure 51 shows the power distribution for the SMR core with the optimized burnable absorber loading pattern.

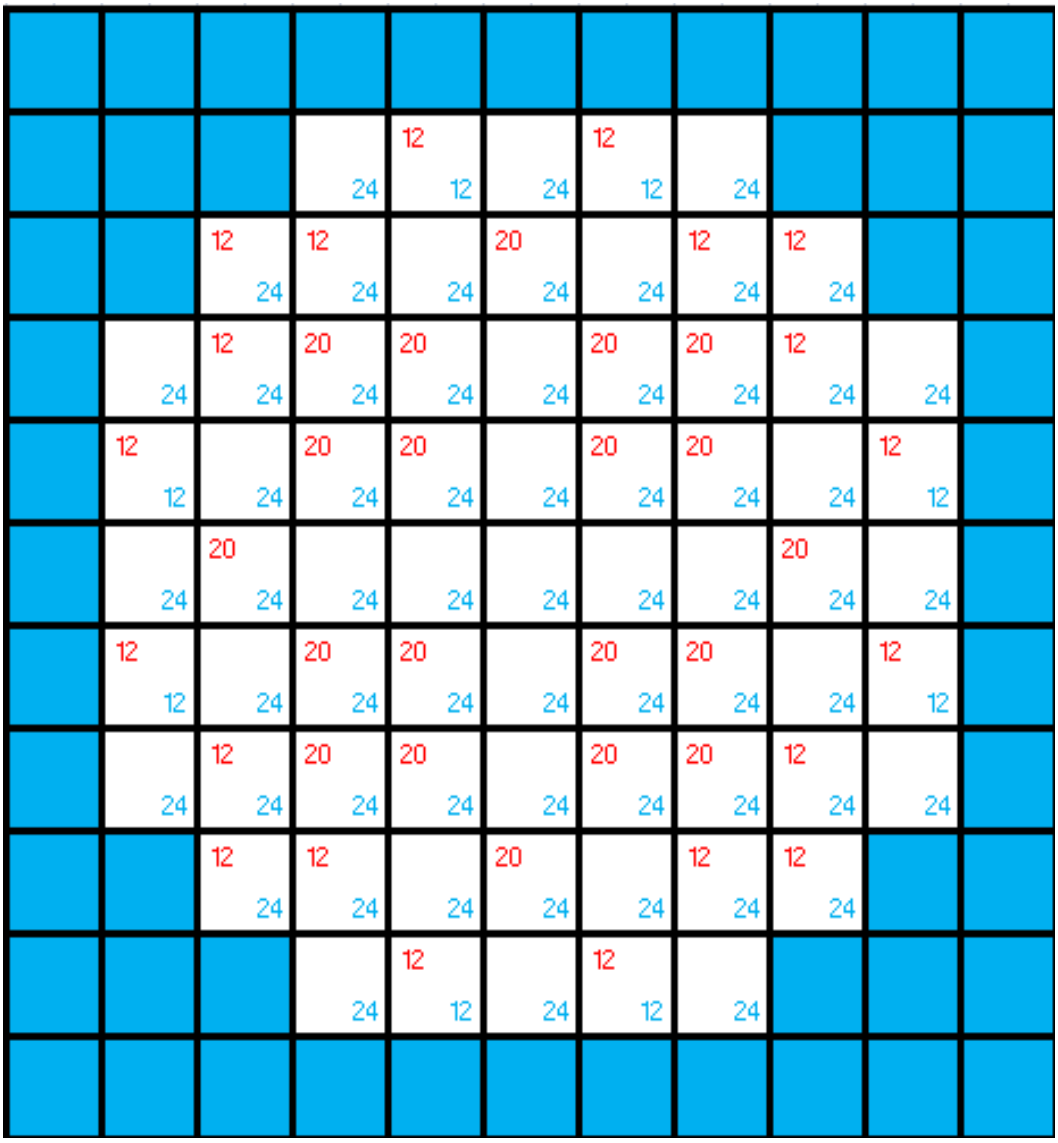

Figure 49: Optimized Burnable Absorber Rod Loading Pattern

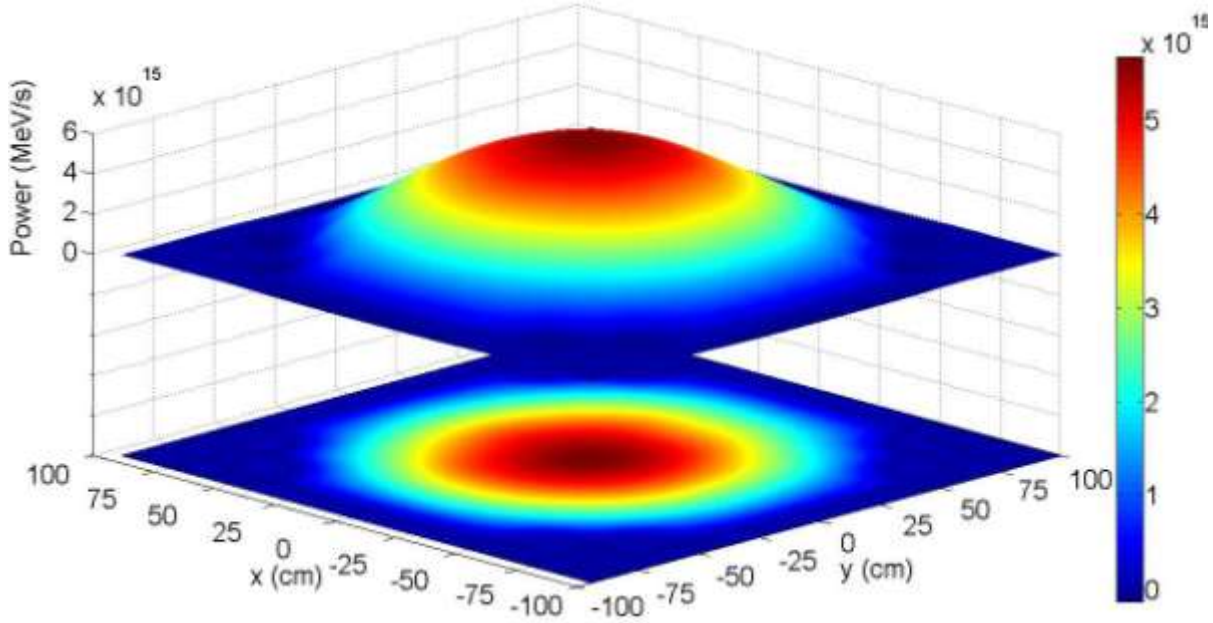

Figure 50: Core Power Distribution at BOL without Burnable Absorbers

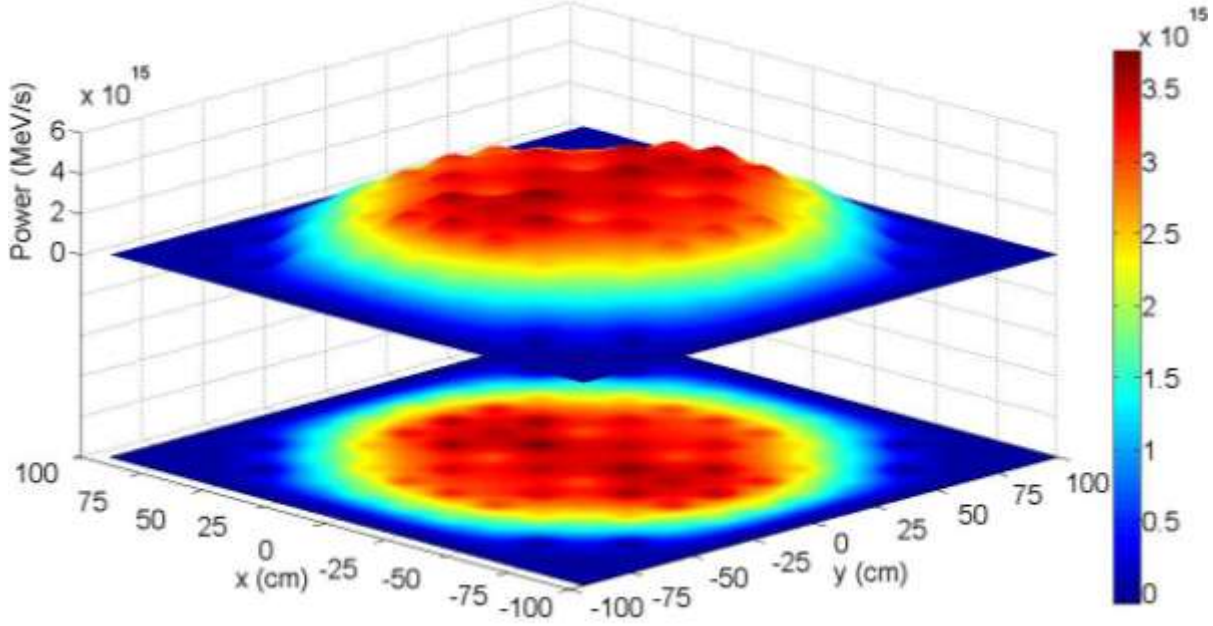

Figure 51: Core Power Distribution at BOL with Burnable Absorbers

7 CONCLUSIONS

The essential goals of this research were to develop a multi-physics methodology whereby high fidelity reactor physics simulations could be performed to observe the xenon oscillatory behavior, if any, in a reactor due to transients. The methodology using MCNP as the neutronics solver was applied to a generic SMR core performing general safety and performance assessments as well as quantifying the threat posed to the SMR from xenon-induced power oscillations. Sensitivity analysis into various sources of error within the methodology, stochastic error and model fidelity were performed building confidence in the capability of the developed methodology to accurately capture the phenomena underpinning the dynamics of xenon-induced power oscillations. As such, options for the control of excess reactivity in the SMR core were briefly explored. This section provides a detailed summary of the research along with conclusions regarding the inherent stability of the SMR core model and discusses possible avenues for future research.

7.1 Research Summary

The multi-physics coupling computational methodology developed was initialized with the MCNP model of the SMR at “cold zero power” conditions and an eight-hour fuel depletion simulation was performed. The power fractions were passed to the SCA tool developed in Python. Fuel and coolant temperature distributions were calculated and along with the output material compositions of the initial simulation used to develop the first step simulation for the xenon-induced power oscillation test featuring the appropriate Doppler-broadened cross sections developed using the SIGACE code.

For the purposes of benchmarking, the developed methodology was used to replicate the results of a startup test performed at the Yonggwang Unit 3 PWR on which other benchmarks have been performed. The benchmark model was a simple one-dimensional model with two separate regions representing the top and bottom regions of the Yonggwang reactor core. Pertinent Yonggwang core characteristics were matched within ten percent of the literature values. The test was initialized by insertion of control rods and removal after six hours. The Power Axial Offset (PAO) and Xenon Axial Offset (XAO) parameters were chosen to quantify any oscillatory behavior observed. The initial magnitude (twenty-two percent PAO) and period (twenty-nine hours) of the observed oscillation in the benchmark model was within ten percent of the literature values. However as the test progressed, the benchmark model demonstrated inherently unstable behavior whereas the Yonggwang reactor shows inherently stable behavior. This discrepancy was attributed to failing to accurately replicate the initial conditions of the Yonggwang reactor in the benchmark model. Additional benchmark models with reduced heights were simulated. The results demonstrated that the developed methodology captured the desired phenomena accurately.

The SMR core model was developed in MCNP/MCNPX with the proposed performance characteristics of the B&W mPower reactor in mind. The resulting SMR featured sixty-nine fuel assemblies with an active fuel length of 240 centimeters producing 530 MW of thermal power for a core life-time of four years. The fuel enrichment was limited at five percent uranium-235. Burnable absorber rods (BARs) with boron carbide as the absorber material were used to shape the core power profile. The fidelity of the model and methodology was increased by adding axial regions within the fuel geometry and accompanying coolant segments within the coolant. To reduce the computational time

associated with the simulations only one-eighth of the core was modelled taking advantage of core symmetries utilizing reflecting boundary conditions to ensure reactor physics behavior was preserved. The final simulation model featured thirteen assemblies each with eight axial fuel regions for a total of 104 fuel regions, 104 coolant regions and additional coolant regions for down-comer, lower plenum, core shroud and upper plenum. The fidelity of the SCA tool was also updated accordingly. Implementation of temperature feedback through fuel temperatures and coolant densities resulted in reduced excess reactivity in the final model when compared to the simple model. The burn-up remained the same since the same amount of energy was drawn from the same mass of fuel. Axial neutron flux, power, fuel temperature and coolant temperature and xenon mass distributions are shown to evolve as expected in LEU light-water systems becoming increasingly uniform with burn-up.

The same test procedure from the benchmarking study was applied to the final SMR core model at beginning of core life (BOL) under full-power and half-power conditions. At BOL the effective neutron multiplication factor decreased rapidly in the first six hours of the test as fission products build up in the fresh fuel. This decline was accelerated by the insertion of control rods into the top region of the core for a further six hours before control rod removal. Excess reactivity in the core was greater at half power where equilibrium fission product concentrations were lower as were fuel and coolant temperatures. The PAO and XAO parameters were calculated in both the full-power and half-power cases and the behavior found to be consistent with an inherently stable SMR core design with less than a single period of oscillations observed and completely dampened below measurable levels in the first thirty hours of the test in all cases. At EOL under full-power and half-power conditions, the PAO and XAO results were again found to be consistent with an inherently

stable core design with oscillatory behavior persisting marginally longer but again completely dissipated within the first forty hours of the test in all cases.

Sensitivity studies were performed investigating the effects of axial discretization, stochastic noise and convergence of the Monte Carlo tallies in the calculations of the PAO and XAO parameters. With respect to axial discretization, simulations were executed featuring eight, twelve, sixteen and twenty-four axial fuel regions, again at BOL and EOL both at full power and half power. The maximum standard deviation was calculated to be 5.2% for the PAO parameter and 2.0% for the XAO parameter, respectively. Considering the initial introduced non-uniformity in both parameters by the control rod insertion and subsequent rapid return to equilibrium, it was concluded that the increased discretization models agreed with the eight-region model in suggesting an inherently stable SMR core design. Due to limitations with computational resources, EOL simulations with twenty-four axial regions were prematurely terminated and no results were obtained.

To quantify stochastic error within the simulation results due to the Monte Carlo method employed by MCNP/MCNPX, seven additional simulations were performed on the eight-region model using different random seeds for each simulation. The results were aggregated and again found not to exceed the maximums of 5.2% for the PAO parameter and 2.0% for the XAO parameter. Thus, the core model was inherently stable even with the stochastic error in each simulation.

Convergence of neutron flux and reaction rate tallies was a requirement for the reliability of the results produced by the Monte Carlo method employed in MCNP/MCNPX. Relevant reaction rates were assessed for convergence and found to be essentially converged

within 2% relative error. This error is propagated through the calculation of the PAO and XAO parameters and these were also found to be converged within 2%.

The preliminary investigation into excess reactivity control options for the SMR design focused on two discrete burnable absorber configurations and two burnable absorber materials. Burnable Absorber Rods (BAR) and Wetted Annulus Burnable Absorber (WABA) rods were used with boron carbide (B_4C) and silver-indium-cadmium (AgInCd) as the absorber materials. The B_4C BAR configuration yielded the largest potential for excess reactivity control by a discrete burnable but exhibited a nontrivial residual absorption penalty.

For fuel integral burnable absorbers, the absorber materials considered were gadolinium oxide (Gd_2O_3) and erbium oxide (Er_2O_3) at two, four, six and eight weight percent within the rod. Fuel enrichment was reduced within the fuel integral burnable rods to avert fuel failure in these reduced thermal conductivity rods. Gadolinium oxide was found to have the greater excess reactivity suppression potential with almost no residual absorption penalty. Erbium oxide demonstrated significantly reduced potential for excess reactivity suppression. However, its behavior was consistent with a dispersed absorber; therefore did not suffer the rod self-shielding effects of a localized absorber such as gadolinium oxide. Considering the design decision to operate the SMR under boron-free coolant regime, erbium oxide offered a viable pathway to retain the excess reactivity control options offered by a dispersed absorber such as soluble boron in the coolant.

Full optimization of the SMR core design with respect to excess reactivity control lies beyond the scope of the research. However, a simple control and burnable absorber

loading was developed by assessing the evolution of the core power profile over the core lifetime.

In conclusion, a multi-physics analysis methodology was developed and utilized to assess a generic small modular reactor core design. The design is found to be inherently stable with respect to xenon-induced power oscillations within the errors associated with the modelling and execution of MCNP/MCNPX.

7.2 Future Research

The developed multi-physics methodology allows for the simulation of complex, time-dependent reactor design problems with temperature feedback mechanisms by coupling existing state-of-the-art codes using an external coupling script. This methodology was applied to the safety and performance assessment of a generic SMR. Several avenues for future research are briefly discussed below including future improvements to the methodology, components of the multi-physics routines and the SMR design itself.

First, with respect to the methodology, the thermal hydraulic assessment needs to be improved to be comparable to the neutronics assessments performed by the MCNP/MCNPX code. In this regard, possible coupling to existing state-of-the-art thermal hydraulics tools such as RELAP-3D or the use of computational fluid dynamics (CFD) can be explored. This will allow for more complex phenomena to be included in the analysis beyond those accommodated by semi-analytic models. The SIGACE code was used to produce Doppler broadened cross sections for the nuclides deemed important to the current research. In future research all cross sections should be appropriately treated to fully implement the effect of temperature on the fuel material.

With respect to improving the design of the SMR, this research provides a base for other transient analyses to be performed, extending perhaps to the analysis of postulated accident scenarios. Further optimization of the fuel and burnable absorber loadings should be explored including axial enrichment of the fuel and combinations of BARs and mixed fuel burnable absorbers to achieve optimal power profile shaping and fuel utilization. Lastly components of the balance of plant must be designed and optimized providing further feedback mechanisms that would have to be implemented.

The developed methodology benefits immensely from the general geometry modelling of the SMR core and the continuous cross section data available in the MCNP/MCNPX codes. However, the Monte Carlo method comes with a significant computational cost with a single time step simulation taking more than six hours to complete resulting in complete simulation with 40 time steps running taking more than 10 days to complete on a 32 core, 2.7 GHz desktop workstation. In the case of some of the EOL simulations, the available 64 GB RAM memory was exhausted resulting in premature termination and no results obtained. In the future, a preliminary assessment should be done to determine the requisite level of fidelity required for an assessment and the computational methodology adjusted accordingly.

Finally, the developed SMR model displayed transient behavior consistent with existing PWRs during restart after shutdown. Thus, it is unlikely that iPWR SMRs of a similar design will experience disruptions in operations due to xenon-induced power oscillations.

REFERENCES

1 Brown, F. B., Goorley, J. T., & Sweezey, J. E. (2003). MCNP5 Parallel Processing Workshop. Proceedings of ANS Mathematics & Computation Topical Meeting. Gatlinburg: American Nuclear Society.

2 International Atomic Energy Agency. (1999). Evolutionary water-cooled reactors: Strategic issues, Technologies and Economic Viability. Vienna: IAEA.

3 Ingersoll, D. T., & Poore, W. P. (2007). Reactor Technology Options Study for Near-Term Deployment of GNEP Grid-Appropriate Reactors. Oak Ridge: ORNL.

4 Ingersoll, D. T. (2009). Deliberately Small Reactors and the Second Nuclear Era. Progress in Nuclear Energy, 51(4), 589-603.

5 Carelli, M. D., Petrovic, B., Mycoff, C. W., Trucco, P., Ricotti, M. E., & Locatelli, G. (2007). Economic comparison of different size nuclear reactors. ANS Symposium (pp. 1-5). Cancun: ANS.

6 Carelli, M. D., Garrone, P., Locatelli, G., Mancini, M., Mycoff, C., Trucco, P., & Ricotti, M. E. (2010). Economic features of integral, modular, small-to-medium size reactors. Progress in Nuclear Energy, 52(4), 403-414.

7 Shropshire, D. (2011). Economic viability of small to medium-sized reactors deployed in future European energy markets. Progress in Nuclear Energy, 53(4), 299-307.

8 Vujić, J., Bergmann, R. M., Škoda, R., & & Miletić, M. (2012). Small modular reactors: Simpler, safer, cheaper? Energy, 45(1), 288-295.

9 Bickel, J. H. (2001). Grid Stability and Safety Issues Associated with Nuclear Power Plants. Evergreen Safety and Reliability Technologies.

10 International Atomic Energy Agency. (2014). Advances in Small Modular Reactor Technology Developments. Vienna: IAEA.

11 United States Nuclear Regulatory Commission. (2015, September 14). Advanced Reactors and Small Modular Reactors. Retrieved from USNRC Website: http://www.nrc.gov/reactors/advanced.html

12 Ingersoll, D. T., Houghton, Z. J., Bromm, R., & Desportes, C. (2014). Integration of NuScale SMR with Desalination Technologies. ASME 2014 Small Modular Reactors Symposium. Washington D.C.: ASME.

13 Ingersoll, D. T., Colbert, C., Houghton, Z., Snuggerud, R., Gaston, J. W., & Empey, M. (2014). Can Nuclear Energy and Renewables be Friends? 2015 International Congress on Advances in Nuclear Power Plants (pp. 1-9). Nice: ICAPP.

14 Reyes, J. N. (2012). Plant Safety in Response to Extreme Events. Nuclear Technology, 128, 153-163.

15 NuScale Power LLC. (2013). NuScale Plant Design Overview. NP-ER-0000-1198: USNRC.

16 United States Nuclear Regulatory Commission. (2015, September 14). Advanced Reactors and Small Modular Reactors - NuScale. Retrieved from USNRC Website: http://www.nrc.gov/reactors/advanced/nuscale.html

17 United States Nuclear Regulatory Commission. (2015, September 14). Advanced Reactors and Small Modular Reactors - Holtec. Retrieved from USNRC Website: http://www.nrc.gov/reactors/advanced/holtec.html

18 United States Nuclear Regulatory Commission. (2015, September 14). Advanced Reactors and Small Modular Reactors - MPower. Retrieved from USNRC Website: http://www.nrc.gov/reactors/advanced/mpower.html

19 United States Nuclear Regulatory Commission. (2015, September 14). Advanced Reactors and Small Modular Reactors. Retrieved from USNRC Website: http://www.nrc.gov/reactors/advanced.html

20 Halfinger, J. A., & Haggerty, M. D. (2012). The B&W mPower™ scalable, practical nuclear reactor design. Nuclear technology, 178(2), 164-169.

21 American Society of Mechanical Engineers. (1976). National Historic Mechanical Engineering Landmark Hanford B Reactor. Richland: ASME.

22 Roggenkamp, P. L. (2000). The Influence of Xenon-135 on Reactor Operation. Aiken: WSRC.

23 Stacey, W. M. (2007). Nuclear Reactor Physics. John Wiley & Sons.

24 Lamarsh, J. R. (1972). Introduction to nuclear reactor theory. Addison.

25 Stacey, W. M. (1970). Xenon-induced Spatial Power Oscillations. Reactor Technology, 13 (3), 252-279.

26 Onega, R. J., & Kisner, R. A. (1977). An axial xenon oscillation model. Annals of Nuclear Energy, 5(1), 13-19.

27 Strydom, G. (2007). Xenon Induced Axial Power Oscillations in the 400MW Pebble Bed Modular Reactor. A Dissertation: North-West University.

28 Waata, C. L. (2006). Coupled neutronics Thermal Hydraulics analysis of a high performance light water reactor fuel assembly. Ph.D. Dissertation: Karlsruhe Institute of Technology.

29 Seker, V., T., J. W., & Downar, T. J. (2007). Reactor physics simulations with coupled Monte Carlo calculation and computational fluid dynamics. International Conference on Emerging Nuclear Energy Systems (pp. 1-5). Istanbul: ICENES.

30 Sanchez, V., & Al-Hamry, A. (2009). Development of a coupling scheme between MCNP and COBRA-TF for the prediction of the pin power of a PWR fuel assembly. International Conference on Mathematics, Computational Methods & Reactor Physics. New York: M&C.

31 Shan, J., Chen, W., Rhee, B. W., & Leung, L. K. (2010). Coupled neutronics/thermal–hydraulics analysis of CANDU–SCWR fuel channel. Annals of Nuclear Energy,, 37(1), 58-65.

32 Hoogenboom, J. E., Ivanov, A., Sanchez, V., & Diop, C. (2011). A flexible coupling scheme for Monte Carlo and thermal-hydraulics codes. International Conference on Mathematics and Computational Methods Applied to Nuclear Science and Engineering (M&C 2011) (Vol. 2, p. 22). 2. M&C.

33 Ivanov, A., Sanchez, V. & Imke, U. (2011). Development of a coupling scheme between MCNP5 and SUBCHANFLOW for the pin-and fuel assembly-wise simulation of LWR and innovative reactors. International Conference on Mathematics and Computational Methods Applied to Nuclear Science and Engineering. Rio De Janeiro: M&C.

34 Ivanov, A., Sanchez, V., Imke, U., & Ivanov, K. (2012). Optimization of a coupling scheme between MCNP5 and SUBCHANFLOW for high fidelity modeling of LWR reactors. La Grange Park: ANS.

35 Ivanov, A., Sanchez, V., & Hoogenboom, J. E. (2012). Single pin BWR benchmark problem for coupled Monte Carlo-Thermal Hydraulics analysis. La Grange Park: ANS.

36 Kotlyar, D., Shaposhnik, Y., Fridman, E., & Shwageraus, E. (2011). Coupled neutronic thermo-hydraulic analysis of full PWR core with Monte-Carlo based BGCore system. Nuclear Engineering and Design, 241(9), 3777-3786.

37 Cardoni, J. N. (2011). Nuclear reactor multi-physics simulations with coupled MCNP5 and STAR-CCM+. Masters' Thesis. : University of Illinois at Urbana-Champaign.

38 Xi, X., Xiao, Z., Yan, X., Li, Y., & Huang, Y. (2013). The axial-power distribution validation of the SCWR fuel assembly with coupled neutronics-Thermal Hydraulics method. Nuclear Engineering and Design, 258, 157-163.

39 Guo, Z., Zhou, J., Zhang, D., Chaudri, K. S., Tian, W., Su, G., & Qiu, S. (2013). Coupled neutronics/thermal-hydraulics for analysis of molten salt reactor. Nuclear Engineering and Design, 258, 144-156.

40 Sjenitzer, B. L., Hoogenboom, J. E., Escalante, J. J., & Espinoza, V. S. (2015). Coupling of dynamic Monte Carlo with thermal-hydraulic feedback. Annals of Nuclear Energy, 76, 27-39.

41 X5 Monte Carlo Team. (2008). MCNP: A General Monte Carlo N-Particle Transport Code, Version 5 Volume I&II: Overview and Theory. Los Alamos: Los Alamos National Laboratory.

42 Pelowitz, D. B. (2008). MCNPX User's Manual Version 2.6.0. . Los Alamos: Los Alamos National Laboratory.

43 Kitcher, E. D. (2012). Performance and Safety Analysis of a Generic Small Modular Reactor. Master's thesis: Texas A&M University.

44 International Association for the Properties of Water and Steam. (2007). Revised Release on the IAPWS Industrial Formulation 1997 for the Thermodynamic Properties of Water and Steam. Lucerne: IAPWS.

45 Sharma, A. R., S., G., & A, T. (2005). The SIGACE package for generating high temperature ACE files – User Manual. Vienna: IAEA.

46 Whalen, D. J., Cardon, D., Uhle, J. L., & Hendricks, J. S. (1991). MCNP: Neutron Benchmark Problems. Los Alamos: Los Alamos National Laboratory.

47 Whalen, D. J., Hollowell, D. E., & Hendricks, J. S. (1991). MCNP: Photon Benchmark Problems. Los Alamos: Los Alamos National Laboratory.

48 Wagner, J., Sisolak, E., & McKinney, G. (1992). MCNP: criticality safety benchmark problems. Los Alamos: Los Alamos National Laboratory.

49 Sitaraman, S. (1992). MCNP: Light Water Reactor Critical Benchmarks. General Electric Nuclear Energy.

50 Wilson, W., Cowell, S., England, T. R., Hayes, A., & Moller, P. (2007). A manual for CINDER'90 version 07.4 codes and data. Los Alamos: Los Alamos National laboratory.

51 England, T. R. (1962). CINDER - A One Point Depletion and Fission Product Program . Pittsburgh: Westinghouse Electric Corp. Bettis Atomic Power Lab.

52 Wilson, W. B., England, T. R., Arthur, E. D., Beard, C. A., & Bowman, C. D. (1993). Accelerator Transmutation Studies at Los Alamos with LAHET, MCNP, and CINDER90. Los Alamos: Los Alamos National Laboratory.

53 Sharma, A. R. (2005). SIGACE code for generating high-temperature ACE files; Validation and benchmarking. International Conference on Nuclear Data for Science and Technology. 769. Institute of Physics Publishing LTD.

54 Organisation for Economic Co-operation and Development - Nuclear Energy Agency. (2013). JANIS 4.0 User's manual. OECD-NEA.

55 Dufek, J., & Waclaw, G. (2005). Managing xenon oscillations in Monte-Carlo burn-up simulations of thermal reactors. XII Meeting on Reactor Physics Calculations in the Nordic Countries. Halden.

56 Leppänen, J. (2007). Development of a new Monte Carlo reactor physics code. Ph.D. Dissertation: VTT Technical Research Centre of Finland.

57 Dufek, J., & Hoogenboom, J. E. (2009). Numerical stability of existing Monte Carlo burn-up codes in cycle calculations of critical reactors. Nuclear Science & Engineering, 162(3), 307-311.

58 Dufek, J., Kotlyar, D., Shwageraus, E., & Leppänen, J. (2013). Numerical stability of the predictor–corrector method in Monte Carlo burn-up calculations of critical reactors. Annals of Nuclear Energy, 56, 34-38.

59 Isotalo, A. E. (2013). Computational Methods for Burn-up Calculations with Monte Carlo Neutronics. Ph.D. Dissertation: Aalto University, Finland.

60 Isotalo, A. E., Leppänen, J., & Dufek, J. (2013). Preventing xenon oscillations in Monte Carlo burn-up calculations by enforcing equilibrium xenon distribution. Annals of Nuclear Energy, 60, 78-85.

61 Song, J. S., & Cho, N. Z. (1997). Two-Group, Flux-Coupled Xenon Oscillation Model with an Equation System of Axial Difference Parameters. Nuclear Technology, 119, 105-111.

62 Song, J. S., & Cho, N. Z. (1999). Analytic Modeling of the Xenon Oscillation Due to Control Rod Movement. Journal of the Korean Nuclear Society, 31(1), 80-87.

63 Generation mPower. (2012). Generation mPower Snapshot. Charlotte: B&W. Retrieved from: http://www.uxc.com/smr/Library%5CDesign%20Specific/mPower/Other%20Documents/mPower%20Snapshot.pdf

64 Nuclear Energy Institute. (2016, June 21). US Capacity by Fuel Type. Retrieved from NEI Website: 2013 http://www.nei.org/Knowledge-Center/Nuclear-Statistics/US-Nuclear-Power-Plants/US-Capacity-Factors-by-Fuel-Type

65 Code of Federal Regulations. 10CFR50.46. Acceptance criteria for emergency core cooling systems for light water nuclear power reactors. As amended at 72 FR 49508, August 2007

66 Collier, J. G., & Thome, J. R. (1972). Convective Boiling and Condensation. Second Edition. Oxford: Clarendon Press.

67 Aoki, N., Osaka, K., Shimada, S., Tochihara, H., & Machii, S. (1980). Xenon Oscillations Tests in Four-Loop PWR Cores. Journal of the Japan Atomic Energy Agency, 22(10), 718-724.

68 Corcoran W. R., Humphries, J. R., & Litke, H. J. (1974). Damping of Xenon Oscillations in the Maine Yankee Reactor. Nuclear Technology, 22, 252-262.

69 Secker, J. R., & Brown, J. A. (2010). Westinghouse PWR Burnable Absorber Evolution and Usage Winter. Transactions of the American Nuclear Society. 103, pp. 733-734. ANS.